Development of the Module Back End Electronics for the Large Observatory For X-ray Timing

Diplomarbeit

vorgelegt von
Pascal Uter

am
Institut für Astronomie und Astrophysik Tübingen
Universität Tübingen

Februar 2013

Meinen Eltern,
in großer Dankbarkeit

Contents

Contents

Acronyms

A/D   Analog/Digital

ACK   Acknowledged

AGN   Active Galactic Nucleus

ASCII   American Standard Code for Information Interchange

ASIC   Application-Specific Integrated Circuit

BH   Black Hole

DFFT   Discrete Fast Fourier Transform

DHU   Data Handling Unit

EOS   Equation Of State

ESA   European Space Agency

FEE   Front End Electronics

FIFO   First In First Out

FOV   Field of View

FPGA   Field-Programmable Gate Array

FSM   Finite State Machine

FWHM   Full Width at Half Maximum

FWZI   Full Width at Zero Intensity

GPS   Global Positioning System

GRB   Gamma Ray Burst

HEXTE   High Energy X-ray Timing Experiment (RXTE)

HMXB   High Mass X-ray Binary

I/O   Input/Output

IAAT   Institut für Astronomie und Astrophysik Tübingen

IDE   Integrated Development Environment

JAXA   Japan Aerospace Exploration Agency

LAD   Large Area Detector

LBAS   LOFT Burst Alert System

LEO   Low Earth Orbit

Contents

LMXB Low Mass X-ray Binary

LOFT The Large Observatory For X-ray Timing

LVDS Low-Voltage Differential Signaling

MBEE Module Back End Electronics

MCP Multi Channel Plate

MIPS Minimum Ionizing Particles

MIXS Mercury Imaging X-ray Spectrometer

NACK Not-Acknowledged

NASA National Aeronautics and Space Administration

NS Neutron Star

OBDHU On-Board Data Handling system

OETS Odd-Even-Transportation-Sort

PBEE Panel Back End Electronics

PCA Proportional Counter Array (RXTE)

PCB Printed Circuit Board

QPO Quasi Periodic Oscillation

RXTE Rossi X-ray Timing Explorer

SAA South Atlantic Anomaly

SDD Silicon Drift Detector

SMOS Soil Moisture and Ocean Salinity

UV Ultra Violet

VHDL VHSIC Hardware Description Language

VHF Very High Frequency

VHSIC Very-High-Speed Integrated Circuits

WFM Wide Field Monitor

XMM X-ray Multi Mirror Mission

Deutsche Zusammenfassung

Das *Large Observatory For X-ray Timing* (LOFT) ist einer der fünf Kandidaten im M3 Auswahlprozess des ESA Cosmic Vision Programms. Der wissenschaftliche Fokus von LOFT liegt auf der Erforschung extrem dichter Materie, wie sie in Neutronensternen vorkommt, und starker Gravitationsfelder, wie sie in der direkten Umgebung von Neutronensternen und Schwarzen Löchern anzutreffen sind. Das Hauptinstrument von LOFT ist der *Large Area Detector* (LAD), welcher aus 2016 einzelnen Detektoren besteht, die in 126 gleichartige Module aufgeteilt sind. Als Detektoren kommen sogenannte *Silizium-Driftdetektoren* zum Einsatz. Dabei wird eine effektive Gesamtfläche von $12\,\mathrm{m}^2$ bei $8\,\mathrm{keV}$ angestrebt. Aufgrund des stark modularisierten Designs des LADs wird für jedes Detektormodul eine dedizierte Datenauswertungselektronik benötigt. Diese sogenannte *Module Back End Electronics* (MBEE) liest die von der Detektorelektronik digitalisierten Anodenwerte ein und führt die Ereignisrekonstruktion durch. Ziel dieser Diplomarbeit war die Entwicklung eines Hardwareprototyps der MBEE.

Die vorliegende Arbeit beschreibt die Mission LOFT und ihren Bezug zu aktuellen Forschungsthemen der Röntgenastronomie. Darüber hinaus werden die beiden wissenschaftlichen Instrumente von LOFT, der *Large Area Detector* und der *Wide Field Monitor* vorgestellt, wobei ein Schwerpunkt auf das hierarchische Elektronikdesign des LADs gelegt wird, da dieses für die MBEE von zentraler Bedeutung ist. Im Rahmen dieser Arbeit wurde die für die MBEE erforderliche Datenverarbeitungspipeline in VHDL[1] beschrieben und in Simulationen erfolgreich getestet. Das VHDL-Design enthält neben der eigentlichen Pipeline die notwendige Struktur, um mehrere Pipelines parallel betreiben zu können, so wie Schnittstellen zu den unter- und übergeordneten Ebenen der Elektronik. Eine nachhaltige Entwicklungsplattform für RTAX2000 FPGAs[2] wurde, unter Berücksichtigung der Anforderungen von LOFT, am Institut für Astronomie und Astrophysik Tübingen (IAAT) eingerichtet. Dabei wurden verschiedene kommerziell erhältliche Lösungen in Betracht gezogen und auf Basis der am besten geeigneten Variante eine individuelle Lösung in Kooperation mit einem Industriepartner entwickelt. Damit war es möglich, einen funktionsfähigen Hardwareprototypen der MBEE zu entwickeln. Der Hardwareprototyp kann entweder alleine oder im Verbund mit den unter- und übergeordneten Ebenen der Elektronik betrieben werden und erlaubt es, das VHDL-Design in Hardware zu verifizieren. Besonders hervorzuheben ist, dass mit diesem Prototypen die Machbarkeit der MBEE auf Basis eines RTAX2000 FPGAs demonstriert wurde.

---

[1] Eine Hardwarebeschreibungssprache, häufig eingesetzt um FPGA-Designs zu beschreiben.
[2] Field-Programmable Gate Array, ein konfigurierbarer integrierter (Logik-)Schaltkreis

1 Introduction

The Large Observatory for X-ray Timing (LOFT; Feroci et al., 2012) is a candidate for the ESA M3 call for medium space missions, focused on dense matter and strong-field gravity. Its main instrument is the Large Area Detector (LAD), consisting of 2016 detectors arranged in 126 identical detector modules, with a total effective area of $12\,\mathrm{m}^2$ at $8\,\mathrm{keV}$ based on monolithic silicon drift detectors. The highly modular design approach requires a dedicated data processing electronics for each module. The Module Back End Electronics (MBEE) reads out the digitized anode values from the detector electronics and performs the event reconstruction. *This thesis describes the development of a hardware prototype of the MBEE.*

Chapter 1, as a brief introduction to X-ray astronomy, explains the mechanisms of radiation and photon–matter interaction relevant to the LOFT science case. It also gives a basic description of commonly used detection principles, introduces recent X-ray missions, and the most important sources, which are primary targets for LOFT. Chapter 2 and 3 introduce LOFT in more detail. The science goals of LOFT, which are divided into three main fields, are presented. LOFT will address key questions to understand: First, the *dense matter* regime and especially the equation of state of neutron stars, second, *strong-field gravity* including matter orbiting close to the event horizon of black holes, and third, *observatory science* including X-ray bursts and jet formation. Chapter 2 introduces the two scientific instruments of LOFT: the Large Area Detector (LAD), a collimated instrument for highly time- resolved spectra, and the Wide Field Monitor (WFM), a coded-mask instrument for all-sky monitoring. Chapter 3 describes the hierarchical electronics design of the Large Area Detector with its main components: the Front End Electronics (FEE) reading out the detector, the Module Back End Electronics performing the event reconstruction, the Panel Back End Electronics, which orders the event data and creates spectra, and the Data Handling Unit, which prepares the event data for transmission to ground. The VHDL[1] Design of the event processing pipeline inside the Module Back End Electronics is presented in Chapter 4, and Chapter 5 describes the development of the hardware prototype including the establishment of a Microsemi RTAX2000 FPGA[2] development platform at IAAT[3]. A summary of the results of this thesis is given in Chapter 6 together with an outlook about the future development of the Module Back End Electronics.

---

[1] A hardware description language, commonly used to describe FPGA designs.
[2] Field-Programmable Gate Array
[3] Institut für Astronomie und Astrophysik Tübingen

The following sections are an introduction to the field of X-ray astronomy and mainly based on Seward, 2010 with additional information from Longair, 2004 and Trümper and Hasinger, 2007.

1.1 X-ray Radiation

X-rays are within the high energy part of the electromagnetic spectrum between γ-rays at higher energies and UVs at lower energies. There are no strict boundaries between the different regions in the electromagnetic spectrum, however electromagnetic radiation in the energy range between 0.1 keV and 100 keV is generally considered to be X-rays.

1.1.1 Physical Processes Shaping Emission in X-ray Astronomy

This section introduces the most important physical processes, which create or shape X-ray radiation in astronomy: blackbody radiation from hot objects, synchrotron radiation from high-energy electrons, thermal bremsstrahlung from hot gas, fluorescence lines and comptonization. It is the result of a combination of these radiation mechanisms, that is usually observed from astronomical sources emitting (not only) in X-rays (see Section 1.4).

Blackbody Radiation from Hot Objects

As described by the Planck law, a black body, and in an approximation all hot matter in thermal equilibrium, emits electromagnetic radiation with a spectrum of the following form (cf. Figure 1.1):

$$I(\nu, T) = \frac{2h\nu^3}{c^2} \frac{1}{\exp\left(\frac{h\nu}{kT}\right) - 1}$$

where $I(\nu, T)$ is the intensity, ν is the photon frequency, T the blackbody temperature, h is the Planck constant, k is the Boltzmann constant and c is the speed of light. The higher the temperature, the higher is the peak energy of the spectrum, which is described by Wien's displacement law:

$$\lambda_{\mathrm{max}} = \frac{2.8977 \times 10^6 \, \mathrm{nm\,K}}{T}$$

For temperatures between 10^6 K and 10^8 K, the maximum of the blackbody spectrum will be in the X-ray range (cf. Figure 1.1 b). Temperatures so high are expected to be found in a variety of X-ray sources, such as on the surface of young neutron stars (Gnedin, Yakovlev, and Potekhin, 2001) and in the inner region of accretion disks around neutron stars and black holes (Shakura and Sunyaev, 1973).
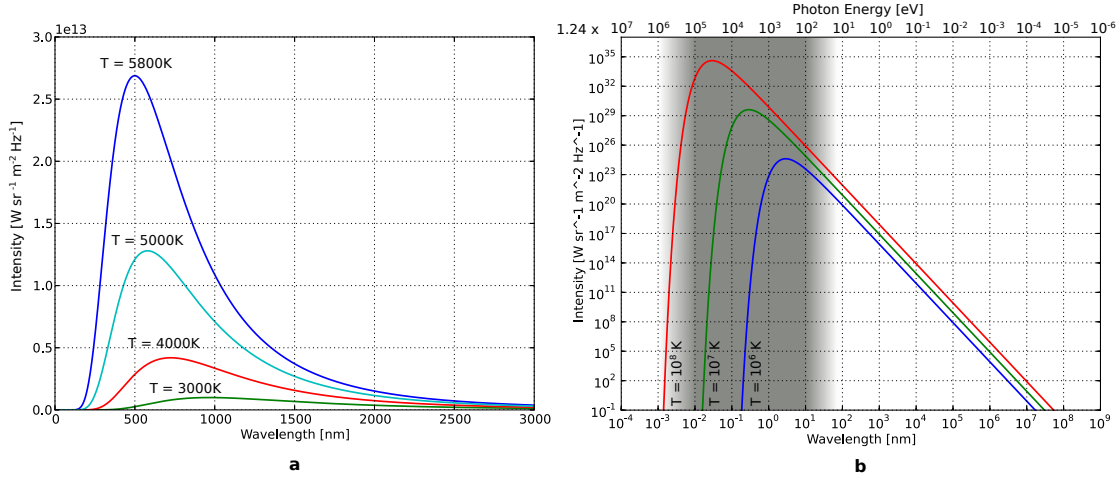
Figure 1.1: Blackbody spectra at different temperatures. The higher the temperature is, the shorter is $\lambda_{\max}$. a) For $T = 5800\,\mathrm{K}$ (about the temperature of the photosphere of the sun) the maximum of the spectrum is in the optical range. b) For temperatures between $10^6\,\mathrm{K}$ and $10^8\,\mathrm{K}$ the maximum of the spectrum is in the X-ray range (highlighted in grey).

Synchrotron Radiation from High-energy Electrons

When an electron moves through a magnetic field with a velocity component perpendicular to the magnetic lines of force, it is subject to the Lorentz force $\vec{F} = q(\vec{E} + (\vec{v} \times \vec{B}))$, which causes a helical motion of the electron (see Figure 1.3a). The accelerated charge emits electromagnetic radiation. In the non-relativistic limit ($E_{\mathrm{kin}} \ll m_{\mathrm{e}}c^2$) this radiation is called cyclotron radiation and is emitted at a single frequency:

$$\nu = \frac{eB}{2\pi m_{\mathrm{e}}}$$

For high-energy electrons with velocities close to the speed of light, this radiation is called synchrotron radiation. Due to relativistic effects, the radiation is no longer emitted at a single frequency but as a spectrum (see Figure 1.3b). The maximum of the spectrum (Blumenthal and Gould, 1970) is at:

$$\nu_{\max} = 0.29\,\nu_{\mathrm{c}} = 0.29 \frac{3\,eB}{4\pi m_{\mathrm{e}}c} \left(\frac{E}{m_{\mathrm{e}}c^2}\right)^2$$

where e is the electron charge, m_{e} is the electron mass, B is the magnetic field, E is the electron energy, and c is the speed of light. Considering an ensemble of electrons and assuming an isotropic velocity distribution, the synchrotron spectrum only depends on the magnetic field B and the energy distribution of the electrons. If the energy spectrum of the electrons is described by a power law $I(E) = AE^{-\gamma}$, where A is a normalization constant and γ the spectral index, the emission spectrum will follow a power law (see Figure 1.2, middle) with spectral
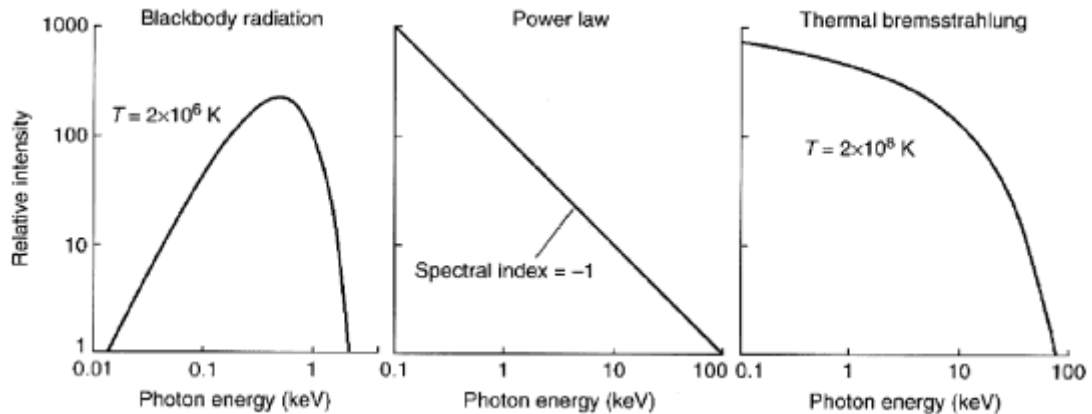
Figure 1.2: Spectra of different astrophysical radiation mechanisms. Black-
body radiation is in the range of X-rays for very high temperatures (10^6 K
and above) as they are expected, for example, on the surface of young neu-
tron stars or in the inner part of accretion disks. A power law spectrum is
the typical spectrum for synchrotron radiation from high-energy electrons.
Thermal bremsstrahlung is emitted from collision of electrons and ions in
hot gas. Source: Seward, 2010

index $\gamma' = (\gamma - 1)/2$ (Blumenthal and Gould, 1970). In fact, a power law as the
high-energy tail of an X-ray spectrum, is usually interpreted as an indication for
synchrotron radiation. Together with polarization, caused by an aligned magnetic
field, the indication is even stronger.
Isolated pulsars in supernova remnants (SNR) are known to have a so called X-ray
synchrotron nebula (Seward and Wang, 1988). The pulsar accelerates electrons to
relativistic energies, which emit synchrotron radiation in the magnetic field of the
pulsar. This radiation in the vicinity of the pulsar can be observed as a diffuse
X-ray source. For example, in the central region of the Crab Nebula[4], a pure power
law spectrum caused by synchrotron radiation can be observed in the energy range
of 2 keV to about 50 keV with a spectral index of $\gamma = 1.10 \pm 0.03$ (Toor and Seward,
1974). Synchrotron radiation is also discussed as a source of X-ray radiation in
the jets of active galactic nuclei (AGN) and X-ray binaries (XB) (Markoff et al.,
2003).

Thermal Bremsstrahlung from Hot Gas

When astronomers talk about hot gas, they usually mean ionized gas of cosmic
composition: For every 10 000 H atoms, there are about 850 He atoms and about
16 atoms of C, O, or heavier elements. The electrons and the positive ions share the
thermal energy and exchange it in frequent collisions. During a collision between

---

[4]The Crab Nebula is the supernova remnant (SNR) of the historical supernova in 1054. A
    pulsar is located in the center of the nebula. It is one of the brightest and most studied
    objects in the X-ray sky.
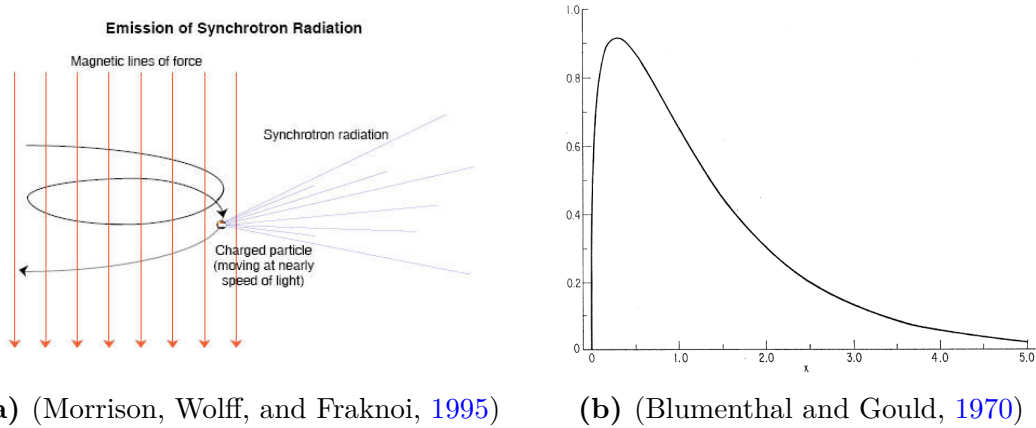
(a) (Morrison, Wolff, and Fraknoi, 1995)   **(b)** (Blumenthal and Gould, 1970)

Figure 1.3: Synchrotron emission from a relativistic electron. a) Shows the helical motion of an electron through a homogeneous magnetic field. b) Shows the synchrotron emission spectrum caused by a single relativistic electron in a homogeneous magnetic field as a function of $x = \nu/\nu_c$, where ν_c is the critical frequency.

an electron and an ion, the electron gets accelerated and emits electromagnetic radiation, which is called thermal bremsstrahlung. Due to the spread in the kinetic energies and different collision parameters, thermal bremsstrahlung leads to a continuum in the emission spectrum as shown in Figure 1.2 (right). The intensity I at a certain energy E and temperature T is described as:

$$I(E,T) \propto Z^2 n_e n_i (kT)^{1/2} e^{-E/kT}$$

where Z is the charge of the ions, n_e the electron density, n_i the ion density, and k the Boltzmann constant.

During the collisions, the free electrons can also excite certain electronic modes of the ions. When the ion makes the transition from the excited state back to the ground state, a photon with the same energy as the energy difference between those two states is emitted. Therefore emission lines can be seen in the spectrum. The radiation from this process is called *characteristic radiation*.

At temperatures of about 10^7 K almost all photons are emitted in the X-ray band, with thermal bremsstrahlung and line radiation equally contributing (Seward, 2010). When observing an X-ray spectrum, the form of the continuum and the presence of emission lines are strong indications for the source to be thermal emission from hot gas.

Fluorescence Lines

Fluorescence is the most important process for line creation in X-ray astronomy. An electron of the lower shells (K, L, ...) of an atom can be freed by a high-energy photon due to the photoelectric effect (bound-free transition). When this happens, there are three possibilities how the vacancy in the lower shell can be

filled: The first possibility is a transition of an electron from a higher shell into the vacant state. In this bound-bound transition, a photon with the same energy as the energy difference between the two involved states is emitted (*fluorescence*). Since the photon caused by this transition has always the same energy, an emission line (fluorescence line) can be observed in the spectrum. It is possible, as a second possibility, that the fluorescence photon will be absorbed by the atom immediately instead of being emitted. The absorbed energy is then used to free another electron of the outer shells. This effect, called *Auger effect*, often happens as a cascade. The third possibility to fill the vacancy in the lower shell is that the atom captures a free electron (free-bound transition). When this happens the excess energy of the electron is emitted as a photon. Since these three effects are competing, the so called fluorescence yield ω_{K} (Bambynek et al., 1972) is of interest:

$$\omega_{\mathrm{K}} = I_{\mathrm{K}}/n_{\mathrm{K}}$$

where I_{K} is the number of fluorescence photons emitted from the K-shells of a sample of atoms, and n_{K} is the number of K-shell vacancies in this sample.

The fluorescence lines are named after the transition, which caused the fluorescence photon. An uppercase Latin letter (K, L, ...) is used to describe the shell in which the vacancy occurred, and a Greek lowercase letter (α, β, ...) denotes the shell, which the electron filling the vacancy came from, with α being the first shell above and β being the second shell above. For example, the Kα line, is the line caused by a transition from the L to the K shell. The most important fluorescence line in X-ray astronomy is the Fe Kα line at 6.4 keV due to its high abundance. Fluorescence lines are used to determine chemical abundances in astronomical objects. See Section 1.4.3 for how the Fe Kα line can be used to probe strong-field gravity and Section 2.2.2 for how LOFT will contribute to that.

Compton Scattering and Comptonization

Compton scattering is the scattering of a photon by an electron (see Figure 1.4 a). In the rest frame of the electron, the photon energy after the scattering E_{ph}' can be described as (Blumenthal and Gould, 1970):

$$E_{\mathrm{ph}}' = \frac{E_{\mathrm{ph}}}{1 + \frac{E_{\mathrm{ph}}}{m_e c^2}(1 - \cos\theta)}$$

where E_{ph} is the photon energy before the scattering, m_{e} is the electron mass, c the speed of light, an θ the scattering angle of the photon (see Figure 1.4 a). For a non-relativistic electron gas with temperature T_{e}, the average energy exchange per scattering $<E_{\mathrm{ph}}>$ is described by (Titarchuk, 1994):

$$\frac{<E_{\mathrm{ph}}>}{E_{\mathrm{ph}}} = \frac{4kT_{\mathrm{e}} - E_{\mathrm{ph}}}{m_e c^2}$$

where k is the Boltzmann constant. If the temperature is so high that $4kT_{\mathrm{e}} > E_{\mathrm{ph}}$, the photon gains energy by the scattering. This effect is called *inverse Compton*

scattering (see Figure 1.4 b). *Comptonization* (Illarionov and Siuniaev, 1975) occurs if the spectrum of an X-ray source is significantly shaped by the repetitive occurrence of inverse Compton scattering before a photon can escape the gas. For example, Comptonization plays an important role in the X-ray emission of the inner part of accretion disks around black holes in close X-ray binaries (Shakura and Sunyaev, 1973).
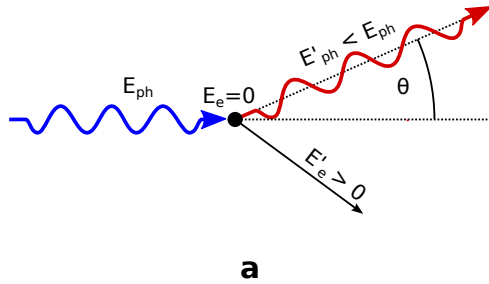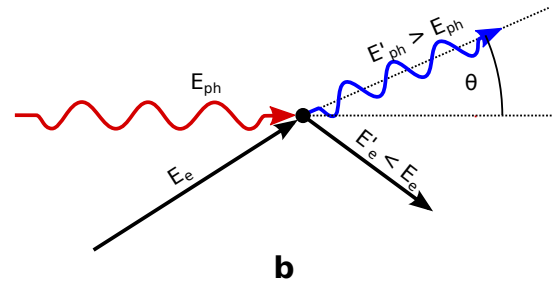

Figure 1.4: Compton- and Inverse Compton Scattering. a) In the rest frame of the electron before the scattering. b) In the laboratory frame.

The processes described in this section are useful for a better understanding of the LOFT science goals described in Section 2.2.

1.2 X-ray Detectors

This section explains how the photoelectric effect and Compton scattering are used to detect X-ray photons. It also introduces two detectors, which are very suitable for X-ray timing with large detection areas: The proportional counter and silicon drift detectors.

1.2.1 Detection Principles

The working principle of almost all X-ray detectors is based on the photoelectric effect at lower energies and on Compton scattering at higher energies. In Silicon, for example, the photoelectric effect is dominating in the energy range between $0.1\,\mathrm{keV}$ and $50\,\mathrm{keV}$. When a bound electron with binding energy E_b absorbs a photon with energy $E_\mathrm{ph} \geq E_\mathrm{b}$, the electron is released and has the kinetic energy $E_\mathrm{kin} = E_\mathrm{ph} - E_\mathrm{b}$. The cross section of the photoelectric effect is proportional to $Z^3 E_\mathrm{ph}^{-3}$, where Z is the proton number. However, the cross section suddenly increases when the photon energy reaches the binding energy of electrons closer to the core. This can be seen in X-ray spectra as edges, caused by electrons from the K and L shell of lighter elements.

The Compton effect, already introduced in the previous Section, is important to detect X-rays at higher energies. In Silicon, for example, the Compton effect is
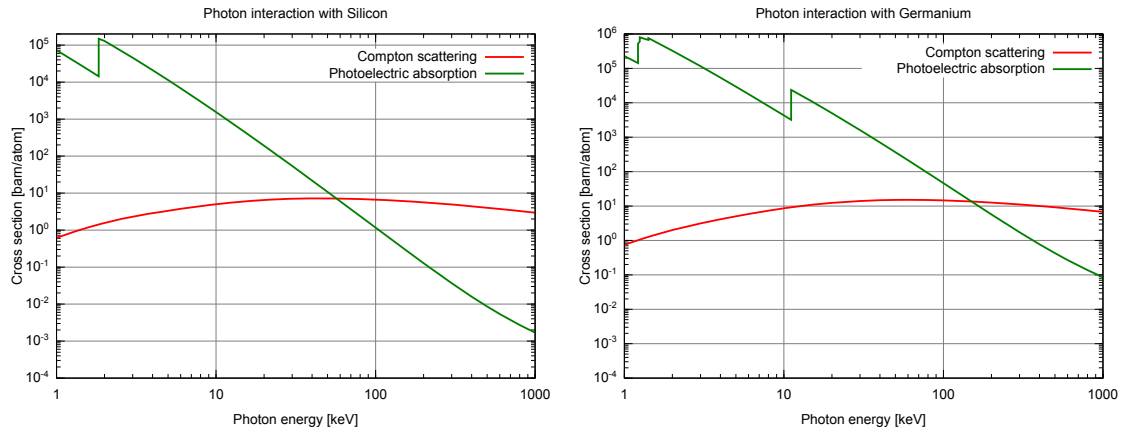
Figure 1.5: Cross sections of the photoelectric effect and Compton scattering for Silicon ($Z = 14$) and Germanium ($Z = 32$), two elements used for semiconductor detectors. The higher the proton number Z, the higher is the energy, at which the Compton effect starts to dominate. Source: Plot by D. Maier/IAAT, Data from Berger et al., 2011

dominating above energies of 50 keV. Since the binding energies of the electrons[5] are very small compared to the photon energy, it is possible to treat the electrons as quasi-free particles, which can receive energy through Compton scattering. The cross sections of photoelectric absorption and Compton scattering for Silicon and Germanium, two commonly used elements for semiconductor detectors, are compared in Figure 1.5.

All of the detectors introduced in the following part of this section utilize photo-electric absorption or Compton scattering to detect X-ray photons.

Proportional Counters

Proportional Counters have been the workhorse detectors in X-ray astronomy since the 1960s. The active region of proportional counters is a compartment filled with gas, which allows for relatively large active volumes. Common gas mixtures are argon/methane or xenon/methane. The compartment has a window, which is transparent to X-ray photons. In a basic setting (see Figure 1.6) a single wire through the compartment is used as a high-voltage anode. When a photon enters the detector, one of the gas atoms will be ionized due
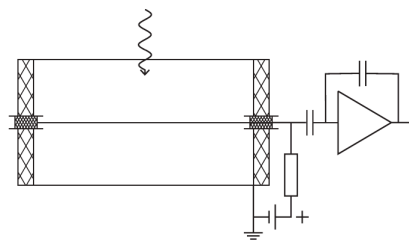

Figure 1.6: A single wire proportional counter. Source: Trümper and Hasinger, 2007

---

[5]The binding energy of the electrons in the p-orbitals in Silicon is < 100 eV (Neddermeyer, 1979 as quoted on Winter, 2013)

to the photoelectric effect. The photoelectron creates a small ionization trail within the gas. The amount of secondary electrons and ions created this way is proportional to the energy of the incident photon:

$$N = \frac{E_{\mathrm{ph}}}{W}; \qquad W \approx 25\,\mathrm{eV} \text{ to } 30\,\mathrm{eV}$$

where N is the number of electron–ion pairs created, E_{ph} is the energy of the incident photon, and W is "the average energy for the creation of one electron–ion pair" (Trümper and Hasinger, 2007) depending on the used gas. The electrons start to drift towards the anode and are accelerated so much that they start to ionize more and more atoms in a cascading process resulting in an amplification of the signal. For proportional counters, the high-voltage of the anode (about 2000 V for the Proportional Counter Array (PCA) of RXTE[6]; Jahoda et al., 2006) is chosen to make the amplification linear. Therefore proportional counters are able to determine the energy of every single incident photon. Proportional counters are suitable to detect X-ray photons of energies up to[7] 60 keV, depending on the density and the proton number of the gas used. Higher energies can not be detected efficiently with conventional proportional counters as the cross section of the photoelectric effect decreases with ν^{-3}. See Figure 1.7 for the efficiency of photoelectric absorption in argon and xenon. Higher energies can be reached with so called *gas scintillation proportional counters* (Policarpo et al., 1972) as they have been used, for example, for the High Pressure Gas Scintillation Proportional Counter (HPGSPC; Manzo et al., 1997) aboard BeppoSAX[8] (Boella et al., 1997), which covered an energy rage of 4 keV to 120 keV.
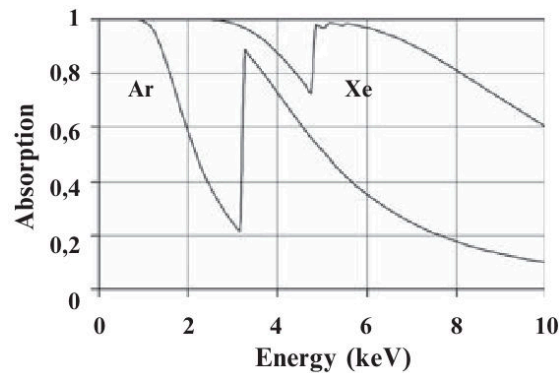
Figure 1.7: Absorption Efficiency of Ar and Xe. The figure shows the photoelectric absorption of 1 cm argon and xenon at a pressure of 1 bar. Source: Trümper and Hasinger, 2007

---

[6]Rossi X-ray Timing Explorer (Bradt, Rothschild, and Swank, 1993).

[7]The proportional counter array (PCA) of RXTE has had an energy range of 2 keV to 60 keV

[8]The "Satellite Astronomia X" (SAX), renamed BeppoSAX in honor of the Italian physicist Giuseppe Occhialini, was an Italian–Dutch X-ray mission launched in 1996 with an especially wide energy range of 0.1 keV to 300 keV.

The energy resolution of proportional counters is limited due to variations in the size of the initial charge cloud created by the incident photon and the following statistical processes. The HPGSPC had an energy resolution of 2.4 keV FWHM at 60 keV whereas the PCA of RXTE reached only 1.1 keV at 6 keV. The time resolution of proportional counters, however, is superb due to the "high drift velocity of electrons in gases (10^6 cm/s to 10^7 cm/s at moderate electrical fields, see for instance (Sauli, 1977))" (Trümper and Hasinger, 2007). The PCA, optimized for high timing and a large effective area, reached a time resolution of 1 µs.

Silicon Drift Detector

Silicon Drift Detectors (SDDs) have been proposed for the first time by Gatti and Rehak (1984). First intended to measure positions, their potential for spectroscopy has been recognized soon (Rehak et al., 1985). The fundamentally new idea of SDDs is to use two separate voltages for the depletion of the semiconductor and the generation of the drift field. This allows for an anode geometry, which makes the size of the anode almost independent of the size of the active area. In this way a small capacitance anode (typically about 50 fF; Rashevsky et al., 2002; Lechner et al., 2001) can be used to read out charges created by an incident photon in a large active area. The low anode capacitance allows to achieve a small readout noise which is important in order to accomplish a high energy resolution for spectroscopy. The voltage at two opposing p^+ contacts (see Figure 1.8a) is always the same whereas the voltage of adjacent p^+ contacts decreases from contact to contact towards the anode. This generates a potential (see Figure 1.8b) with a minimum (for electrons) at the anode.

When a photon (or a particle as in the figure) creates a cloud of electron–hole pairs in the active region of the detector with the number of pairs being proportional to the energy of the incident photon, the holes will be absorbed by a p^+ contact, while the electrons drift in a buried channel parallel to the surface towards the anode. The drift velocity of the electrons is (Spieler, 2005):

$$\vec{v}(x) = \mu \vec{E}(x)$$

where $\vec{E}$ is the electrical field, $\vec{v}$ is the velocity of the electron, and μ is the so called mobility. For electrons in silicon, the mobility is $\mu = 1350 \frac{\text{cm/s}}{\text{V/cm}}$. With an electric field of $E = 370$ V/cm as it is used for LOFT, this leads to a drift velocity of $v = 5$ mm/µs. Knowing the drift velocity of the electrons and the drift time of a certain electron cloud, it is possible to reconstruct the incident position in the drift direction. In astronomical settings, however, the drift time is usually unknown due to the unknown arrival time of the photon. If a spatial resolution in drift direction is desired, it is possible to use the spread of the charge cloud to estimate its drift distance. A spatial resolution perpendicular to the drift direction is achieved by an appropriate segmentation of the anode. Spatial resolutions of about 5 µm have been demonstrated to be possible (Rehak et al., 1985). With
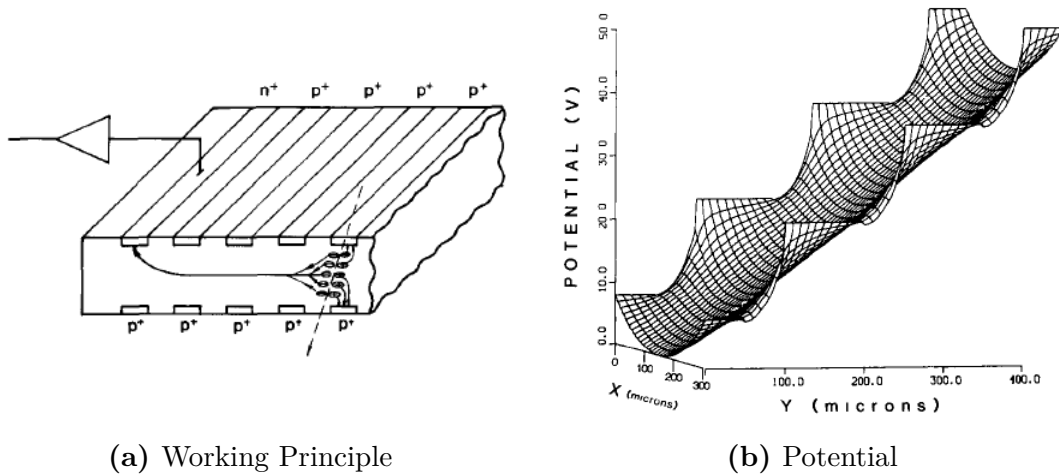
(a) Working Principle   **(b)** Potential

Figure 1.8: Silicon Drift Detector. a) shows the working principle of a silicon drift detector (SDD). b) shows the electric potential in the drift region with a voltage of 15 V between two neighboring p^+ contacts. Source: Rehak et al., 1985

silicon drift detectors optimized for spectroscopy an energy resolution of 145 eV FHWM at 5.9 keV at a temperature of $-50\,°C$ has been reached (Lechner et al., 1996). With a digital filter it was even possible to reach a resolution of 137 eV.

When interested in X-ray timing, not only the energy resolution and the readout time is important but also the active area. A large active area, and therefore a high sensitivity, allows to create spectra with short integration times. However, conventional silicon drift detectors optimized for spectroscopy have small active areas between about $1\,mm^2$ and $1\,cm^2$. A huge step forward to larger areas has been made with the large area silicon drift detector developed for the inner tracking system (ITS) of ALICE[9] at the LHC. These detectors, optimized for position sensing, have a large active area of $52\,cm^2$. It has been shown by Zampa, Rashevsky, and Vacchi (2009) that these detectors are also suitable for spectroscopy. An energy resolution of 386 eV FWHM at 5.9 keV has been reached at a temperature of $0\,°C$ with external readout electronics and without electronic filters, demonstrating the great potential of this technology. With integrated readout electrics, lower temperatures, and electronic filters much better energy resolutions are to be expected.

The silicon drift detector which will be used for LOFT is based on the ALICE detector with design optimizations for spectroscopy. The design goal for the LOFT detector is 200 eV FWHM at 6 keV. The timing resolution of silicon drift detectors is limited by the maximum drift time. With a maximum drift distance of 35 mm and a drift velocity of 5 mm/µs for the LOFT detector, the maximum drift time is 7 µs. Therefore, this is the goal of the time resolution. A big advantage of silicon drift detectors over proportional counters is their very small mass of about

---

[9]ALICE is A Large Ion Collider Experiment at the Large Hadron Collider (LHC) at the European Organization for Nuclear Research (CERN) near Geneva, Switzerland.

$1 \, \text{kg/m}^2$ allowing for large area detectors aboard spacecrafts. The silicon drift detector used for LOFT is described in Section 2.3.1.

1.2.2 Detector Optics

Classical optical instruments like lenses or mirrors do not work for X-rays at all (refraction) or only limited (reflection): Therefore, new methods have been developed to achieve X-ray imaging capabilities. Collimators and coded masks work a non-focusing instruments. While collimators solely limit the field of view, coded masks provide a non-focusing imaging technology. The only known focusing optics for X-rays is the Wolter optics.

Collimator

The idea of a collimator is to decrease the field of view (FOV) in order to avoid source confusion and to reduce background. The working principle of a collimator is shown in Figure 1.9a. The angle α describes the field of view at half intensity:

$$\alpha = 2 \arctan \left(\frac{d}{2L} \right)$$

To reach a field of view of $\alpha = 1°$ for a detector with $d = 7 \, \text{cm}$ the length of the collimator must be about $L = 4 \, \text{m}$. This is obviously not viable on a spacecraft. Multiple slits can be used to reduce the necessary collimator length, as shown in Figure 1.9b. Using n slits reduces the necessary collimator length to L/n. However, the more slits are used, the smaller becomes the aperture due to the finite thickness of the collimator walls. If desired, imaging capability can be achieved by "scanning" the sky with a continuous change of the pointing. This is sometimes referred to as temporal aperture modulation (Matteson et al., 1985). The collimator used for the LOFT Large Area Detector (LAD) is described in Section 2.3.1.

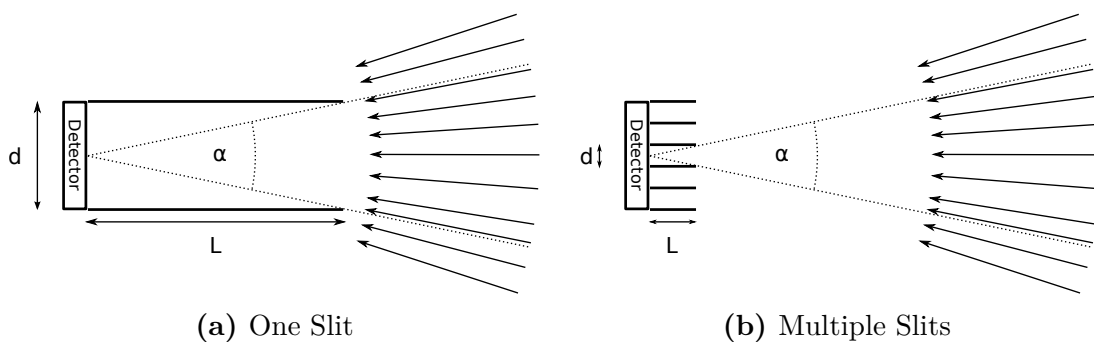**(a)** One Slit   **(b)** Multiple Slits

Figure 1.9: Working Principle of a Collimator. The same field of view as in a) can be reached in b) with multiple slits and a shorter collimator length. With n slits the collimator length can be reduced to L/n.

Coded Mask

Coded masks, so called spatial aperture modulation instruments, have been independently proposed by Ables (1968) and Dicke (1968). They are used with position-sensitive detectors. The mask is made of an X-ray absorbing material and has a certain hole pattern (see Figure 1.10). When the mask is illuminated by one source, the shadow of the mask is visible on the detector and can be used to reconstruct the position of the source. This also works for a superposition of many sources. Mathematically this is described as a folding:

$$D(x) = M(x) \times S(x)$$

where x is the two-dimensional coordinate, $S(x)$ the sky distribution, $M(x)$ the mask-dependent modulation function, and $D(x)$ the detected distribution. In general the modulation matrix M is not invertible and therefore the image reconstruction is a non-trivial task. Different methods involving cross-correlation or inverse Fourier transformations have been developed (Skinner, 1995). The angular resolution, which can be reached with coded masks is d/D, where d is size of the holes and D the distance from the mask to the detector. The better the angular resolution is for a certain distance D, the smaller is the opening fraction of the mask. This means there is a trade off between angular resolution and aperture. LOFT uses coded masks for its Wide Field Monitor (WFM), see Section 2.3.2.
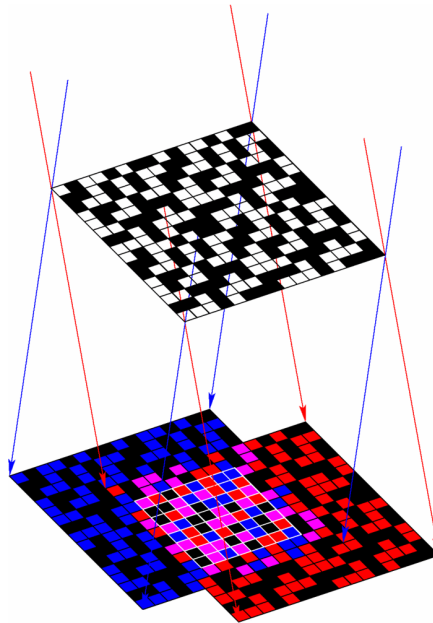

Figure 1.10: Working principle of a coded mask detector. Light from two sources (red and blue) projects two overlapping shadows of the coded mask onto the detector. With mathematical cross-correlation, it is possible to reconstruct the image from the shadow pattern on the detector. Source: ISDC/M. Türler

Wolter Optics

In general, X-rays are not reflected from mirror surfaces. However, on very smooth surfaces gracing incident ($< 1°$) reflections are possible. The higher the photon energy is, the smaller must the incident angle be to allow for reflection. Wolter (1952) proposed the first design for a focusing X-ray optics. First intended for X-ray microscopy, the value of his design for astronomy has been realized soon. The Wolter Type-I setup has a first reflection on a paraboloid surface and a second reflection on a hyperboloid surface to form an image in the detector plane (see Figure 1.11). When only accepting grazing incident angles, the effective aperture is rather small. It is the big advantage of the Wolter Type-I design that it allows to nest mirrors in order to increase the effective aperture. The highest energy, which a Wolter telescope has been successfully used for is 80 keV (NuSTAR; Harrison et al., 2010). The best angular resolution so far has been reached with Chandra: $< 1''$ (Weisskopf et al., 2002).
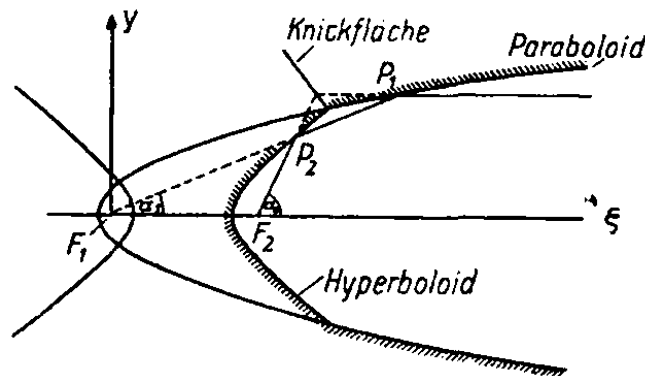

Figure 1.11: Wolter Type-I Setup. Parallel on-axis X-rays are first reflected on the paraboloid mirror then on the hyperboloid mirror which forms an image in the detector plane. Usually several mirrors are nested to increase the effective aperture. Source: Wolter, 1952

1.3 Recent X-ray Missions

Since the first X-ray satellite Uhuru (Giacconi et al., 1971) launched in 1970, there have been many significant X-ray missions. Especially important for LOFT is the Rossi X-ray Timing Explorer (RXTE), which, as a mission dedicated to X-ray timing, can be seen as a precursor of LOFT. The current X-ray missions, Chandra, XMM-Newton, Suzaku, and NuSTAR are compared to RXTE and LOFT in Table 1.1 with regard to their timing capabilities. From each mission the instruments with the best timing capabilities have been chosen. For high timing measurements, the effective detector area is as important as the time resolution. In the following part of this section RXTE is described in more detail. Then,

the current X-ray missions are briefly introduced with respect to their timing capabilities.

Table 1.1: Comparisson of recent X-ray missions with regard to their timing capabilities.

Instrument	Energy range [keV]	Eff. Area [cm^2]	@ [keV]	Time Res. [µs]	Ref.
RXTE PCA	2 − 60	6000	10	1	1
RXTE HEXTE	20 − 250	1200	50	8	2
Chanrda HRC-S	0,07 − 10	800	2	16	3
XMM-Newton PN	0,15 − 12	1550	1.5	30 / 7	4, 5
Suzaku HXD	10 − 600	260	100	6	6
NuSTAR	5 − 80	900	9	2	7
LOFT LAD	2 − 80	120000	8	7	8

1) Glasser, Odell, and Seufert, 1994; 2) Gruber et al., 1996; 3) Weisskopf et al., 2002;
4) Jansen et al., 2001; 5) Strüder et al., 2001; 6) Terada et al., 2008;
7) Harrison et al., 2010; 8) LOFT Consortium, 2012b

1.3.1 Rossi X-ray Timing Explorer (RXTE)

The Rossi X-ray Timing Explorer (RXTE, see Figure 1.12), launched in December 1995 by NASA, was successfully operated for 16 years before it was decommissioned at the beginning of 2012. RXTE carried three instruments: The proportional counter array (PCA; Glasser, Odell, and Seufert, 1994), a large area timing instrument; the High-Energy X-ray Timing Experiment (HEXTE, Gruber et al., 1996); and the all-sky monitor (ASM, Levine et al., 1996).
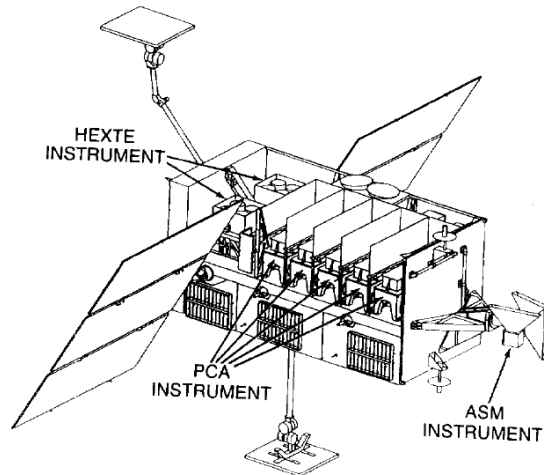

Figure 1.12: The instruments of RXTE. Source: Glasser, Odell, and Seufert, 1994

RXTE - **Proportional Counter Array**

The proportional counter array (PCA) consisted of xenon-based proportional counters (see Section 1.2.1 for the working principle of proportional counters) with a total collecting area of $0.6\,\mathrm{m}^2$ at $10\,\mathrm{keV}$ covering the $2\,\mathrm{keV}$ to $60\,\mathrm{keV}$ energy range. The time resolution of the PCA was $1\,\mathrm{\mu s}$ and the spectral resolution was about $18\,\%$ at $6\,\mathrm{keV}$. A $1\,\mathrm{Crab}$ observation caused about $10\,000\,\mathrm{counts/s}$ in the energy range of $2\,\mathrm{keV}$ to $30\,\mathrm{keV}$.

The PCA consisted of five co-aligned proportional counter units (PCU, see Figure 1.13) which had a collimated field of view of $1°$ FWHM. A set of anodes operated at about $2000\,\mathrm{V}$ was used to detect events and a shielding around the detector prevented X-rays from entering the detector from outside the field of view. High-energy particles, however, cannot be stopped by the shielding, which is why anti-coincidence chambers were placed around the main detector volume. An americium source inside the detector volume was used for gain calibration. The calibration photon was identified by the simultaneously detected alpha particle from the nuclear decay.

The relatively large area of the PCA allowed to detect an AGN source with $1.3\,\mathrm{mCrab}$ in the $2\,\mathrm{keV}$ to $10\,\mathrm{keV}$ band with a significance of 2σ within $1\,\mathrm{s}$.
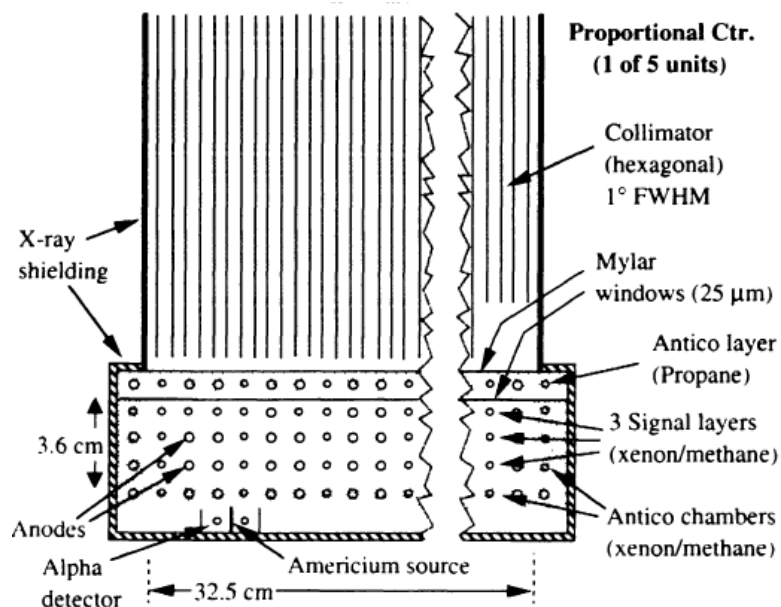

Figure 1.13: Proportional Counter Unit. Source: Bradt, Rothschild, and Swank, 1993
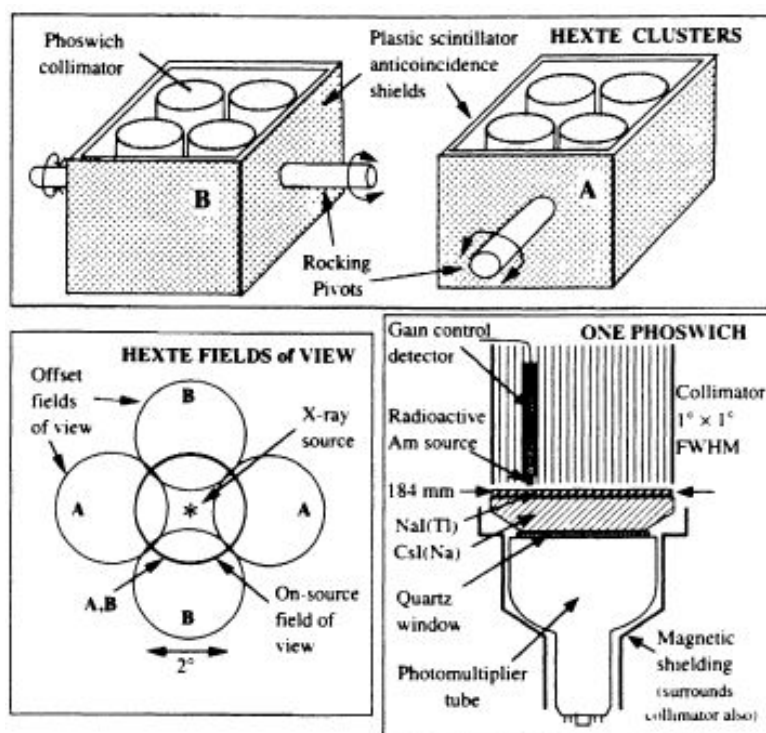
Figure 1.14: The High Energy X-ray Timing Experiment (HEXTE) consisted of two clusters (top) with four phoswich detectors (bottom right) each. The clusters were rocked on and off the source to observe the background resulting in five different pointing positions (bottom left). Source: Bradt, Rothschild, and Swank, 1993

RXTE - High Energy X-ray Timing Experiment

The High Energy X-ray Timing Experiment (HEXTE) was co-aligned with the PCA and had also a collimated field of view of 1° FWHM. HEXTE covered the higher energy range from 20 keV up to 250 keV with two clusters of four phoswich detectors each (see Figure 1.14) with a time resolution of 8 µs. HEXTE had an effective area of $0.12\,\mathrm{m}^2$ at 50 keV with an energy resolution of 18 % at 60 keV. The phoswich detector consisted of a 3 mm thick NaI scintillation crystal coupled to a 38 mm thick CsI crystal used as an anti-coincidence detector. The scintillation light from both crystals was observed with a photomultiplier tube (PMT). Four of these detectors formed a HEXTE cluster, which was shielded on 5 sides by a plastic scintillator, also watched by photomultiplier tubes, for background reduction. The two clusters were rotated ("rocked") in orthogonal directions to alternate on- and off-source observations, which allowed to perform a background reduction. Each cluster monitored the background on two opposite sites, which made a total of four background pointings around the the source (see Figure 1.14). The rocking of the clusters was timed in a way that always at least one cluster was pointed at the source.

RXTE - **All-Sky Monitor**

The all-sky monitor (ASM) was a 1D-coded mask instrument with position-sensitive proportional counters. It had a field of view of 6° x 90° FWHM or 12° x 110° FWZI. The ASM was sensitive in the range of 2 keV to 10 keV and scanned about 80 % of the sky during one orbit, i.e. in 90 min. Its sensitivity allowed to detect a 30 mCrab source in 90 min and a 10 mCrab source in a day. The angular resolution in the imaging direction was 0.2°. This allowed to determine a source position within 0.2° x 1° for a weak source and 3′ x 15′ for a 5σ detection.

RXTE - **Highlights**

RXTE was mainly focused on systems involving black holes or neutron stars to study strong gravity, high densities and high magnetic fields. It discovered over a dozen stellar mass black holes. Monitoring quasi-periodic oscillations and observing spectra from black hole binaries allowed to probe the angular momentum of black holes. RXTE also found evidence that jet ejections are linked with accretion disks and for the similarity of stellar mass and supermassive black holes (Mirabel, 2007).
Employing a variety of techniques (Poutanen and Gierliński, 2003; Bhattacharyya et al., 2005), RXTE was able to put constrains on the masses and radii of neutron stars and therefore to begin to constrain possible equations of state for dense matter. Further remarkable results of RXTE include monitoring outbursts from Soft Gamma-ray Repeaters, Anomalous X-ray Pulsars, and transient sources as well as the discovery of sub-millisecond quasi-periodic oscillations (van der Klis et al., 1996), which are described in Section 1.4.3 and will be further investigated by LOFT (see Section 2.2.2). More information on the scientific achievements of RXTE can be found in Swank, 2006.

1.3.2 Chandra X-ray Observatory

The Chandra X-ray Observatory (Weisskopf et al., 2002) was launched by NASA in July 1999 from the space shuttle Columbia and is still operational after more than 13 years (see Figure 1.15a). The main component of Chandra is its telescope system with a focal length of 10 m. The High Resolution Mirror Assembly (HRMA) consists of four nested paraboloid and 4 nested hyperboloid mirrors. The mirrors have an effective area of about 0.075 m^2 at 1 keV and an impressive angular resolution of 0.5″ is reached.
Chandra carries four science instruments: The Advanced CCD Imaging Spectrometer (ACIS) consists of ten CCDs in two arrays, one for imaging and one for spectroscopy. The High Resolution Camera (HRC) uses micro-channel plates (MCPs) with a high angular resolution ($< 0.5″$ FWHM) over a relative wide field of view ($31′ \times 31′$). Two transmission gratings can be inserted into the focused X-ray beam. The High Energy Transmission Grating (HETG) provides a resolving power[10] of 60 to 1000 for energies of 0.4 keV to 10 keV an the Low Energy Trans-

---

[10]The resolving power is defined as $R = \frac{E}{\Delta E}$ where ΔE is the smallest energy difference, which

mission Grating (HETG) provides a resolving power of 40 to 2000 for energies of 0.09 keV to 3 keV (Smithonian Astrophysical Observatory, 2011).

While ACIS reaches a time resolution of 2.85 ms in its so called *bright source fast timing* mode, the HRC has a time resolution of 16 µs. Due to a wiring error of the HRC, this time resolution can only be maintained at low fluxes. For bright sources, it is only possible to achieve a time resolution in the order of a millisecond.

1.3.3 XMM-Newton

The X-ray Multi Mirror Mission (XMM-Newton) (Jansen et al., 2001) was launched by ESA in December 1999, about half a year after Chandra was launched by NASA, and is also still operational (see Figure 1.15b). XMM-Newton is also designed for imaging and spectroscopy. It carries three X-ray telescopes (each with about 1550 cm^2 effective area) and one optical/UV telescope called the Optical Monitor (OM). Each of the three X-ray telescopes consists of 58 nested mirrors in the previously described Walter Type-I configuration. The effective area of XMM-Newton is four times larger than the effective area of Chandra but the spatial resolution of XMM-Newton is only about 6″ FWHM. In this way the two missions are complementary.

XMM-Newton has one instrument for each telescope, all of which are used simultaneously. The European Photon Imaging Camera (EPIC; Strüder et al., 2001) consists of three CCD detectors, one in the focus of each X-ray telescope. In two of the X-ray telescope beams are the Reflection Grating Spectrometers (RGS), which provide a resolving power of about 200 to 800 at an energy range of 0.35 keV to 2.5 keV.

In the two telescopes with the reflection gratings EPIC MOS CCDs are used, whereas in the third telescope the EPIC PN CCD is used. Both CCD types can be operated in various modes including a timing mode. The best time resolution achievable with the MOS cameras in timing mode is 1.75 ms (Turner et al., 2001). The PN camera, however, achieves 30 µs in the timing mode (Strüder et al., 2001). It also supports a so-called burst mode in which a time resolution of 7 µs is achieved, which however reduces the duty cycle to 3 %. Therefore, the EPIC PN camera is the instrument of choice for timing observations with XMM-Newton.

---

is possible to distinguish at the energy E.

1.3.4 Suzaku

Suzaku (Mitsuda et al., 2007), formerly know as ASTRO-EII, is a JAXA mission launched in July 2005, designed for high-energy resolution spectroscopy over a wide energy range (0.3 keV to 600 keV). Its main science goals are to study hot plasmas, the structure and evolution of the universe, and to perform wide band spectroscopy of black hole candidates and active galactic nuclei. The primary instrument of Suzaku is the X-ray spectrometer (XRS, Kelley et al., 2007), which is based on quantum calorimeters with a superb energy resolution of about 6 eV at 6 keV. Unfortunately, due to a defect in the cooling system shortly after launch, it was not possible to gather any science data with this instrument. The other two instruments are still operational. The X-ray Imaging Spectrometer (XIS, Koyama et al., 2007) has an energy range of 0.2 keV to 12 keV and a field of view of $18' \times 18'$. The Hard X-ray Detector (HXD, Takahashi et al., 2007) is a non-imaging spectrometer with a wide energy range of about 10 keV to 600 keV. With its time resolution of 6 µs the HXD is well suited for high timing observations. Its effect area of $260 \, \mathrm{cm}^2$, however, allows high timing analysis only for very bright sources.

1.3.5 NuSTAR

The Nuclear Spectroscopic Telescope Array (NuSTAR, Harrison et al., 2010) is currently the youngest space-born X-ray mission (see Figure 1.15d). It was launched by NASA in June 2012 to take a census of collapsed compact objects surrounding the galactic center, to map recently synthesized material in young supernova remnants, and to learn more about the mechanism powering relativistic particle jets in active galactic nuclei. NuSTAR carries two co-aligned telescopes with Wolter Type-I optics. This is the first time that X-rays in the energy range of 6 keV to 79 keV are focused with an astronomical instrument in orbit. After deployment in orbit, the telescopes extended to achieve the focal length of 10 m. In the focal plane of each of the two telescopes are four Cadmium-Zinc-Tellurium detectors with 32×32 pixels reaching an energy resolution of 0.4 keV FWHM at 6 keV and 0.9 keV at 60 keV.
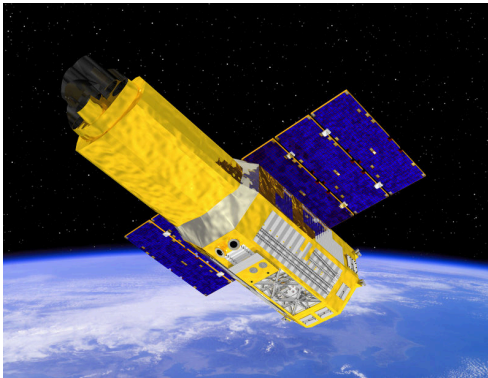
NuSTAR has a superb energy resolution of 2 µs, however, only bright sources can be used for high timing analysis due its active area of about $900 \, \mathrm{cm}^2$. While NuSTAR can measure fluxes of up to 10^4 counts/s without pileup, it can only process 400 events/s, which is a severe limitation of its timing capabilities.
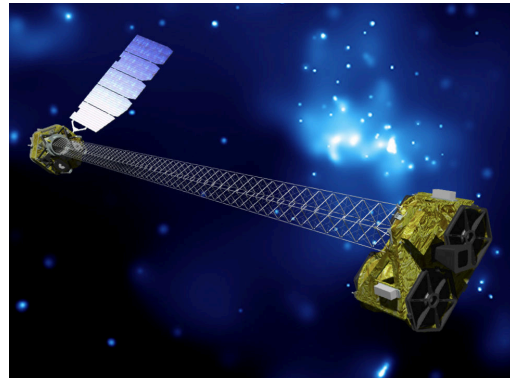
(a) Chandra (NASA/CXC/NGST)

(b) XMM-Newton (ESA/D. Ducros)

(c) Suzaku (JAXA)

(d) NuSTAR (NASA/Caltech)

(e) RXTE (NASA)

Figure 1.15: Artistic views of Chandra, XMM-Newton, Suzaku, NuSTAR, and RXTE

1.4 Observable Objects

There is a huge variety of objects which can be observed in the X-ray range: stellar sources, supernova remnants, pulsars, binaries, active galactic nuclei and galaxy clusters, to only name a few. Most of the targets which are important for LOFT involve compact objects. Therefore, this section briefly describes the end stages of stellar evolution and gives a short description of neutron stars and black holes. Then X-ray binaries, as one of the most important targets for LOFT, are introduced and effects shaping the spectrum of X-ray binaries are explained. This section is also based on Karttunen et al., 2007.

1.4.1 End Stages of Stellar Evolution

Stellar evolution is usually described in the so called Hertzsprung-Russel diagram (see Figure 1.16). It shows the luminosity of a star in dependence of its effective temperature. Luminosity L, effective temperature T_{eff}, and radius R of a star can, according to the Stefan-Boltzmann law, be described as:

$$L = 4\pi R^2 \sigma T_{\text{eff}}^4$$

where σ is the Stefan-Boltzmann constant. This implies that a horizontal movement in the Hertzsprung-Russel diagram towards higher temperatures at a constant Luminosity means a decreasing radius, whereas a vertical movement in the Hertzsprung-Russel diagram toward higher luminosities at a constant temperature means an increasing radius.
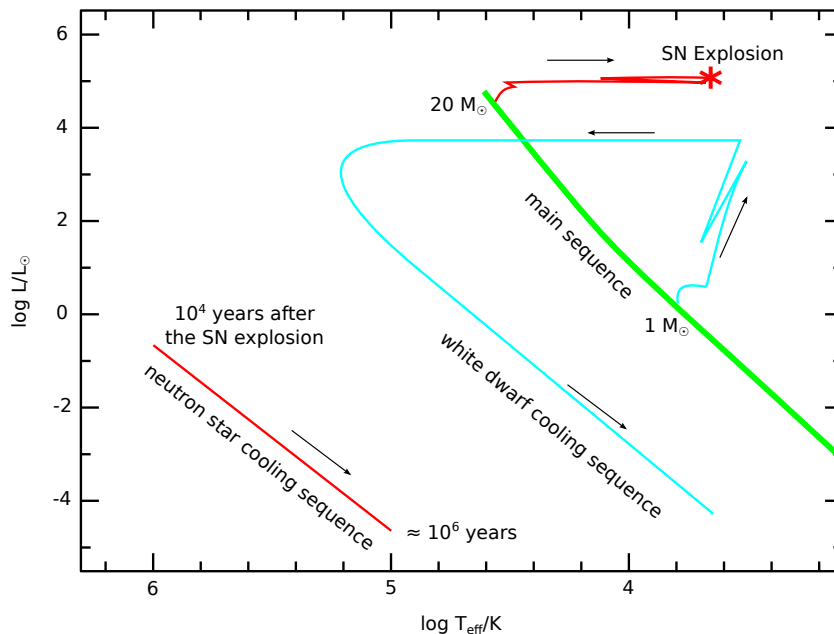

Figure 1.16: Stellar Evolution of a $1\,M_\odot$ and a $20\,M_\odot$ star in the Hertzsprung-Russel diagram. Source: lecture script by Prof. K. Werner/IAAT

The most important parameter when considering the evolution of a star is its (initial) mass as it mostly determines what the star is evolving to and how fast the evolution takes place. The higher the stellar mass, the faster goes the evolution of the star. All stars on the main sequence have in common that their only energy source is hydrogen burning. Stars between $0.08\,M_\odot$ (bottom right) and about $70\,M_\odot$ (upper left) can be found on the main sequence. A star leaves the main sequence when its hydrogen supply in the core region is exhausted. The hydrogen burning continues in a shell around the helium core. The mass and temperature of the helium core increase due to the hydrogen shell burning. In stars with masses above $0.26\,M_\odot$ the helium core reaches a temperature of about $10^8\,K$ where the helium ignites and starts fusing into carbon. When all helium of the core is fused into carbon, the helium burning continues in a shell around the carbon core. Now there are two shells burning in the star: the inner helium shell and the outer carbon shell.

Stars with masses under $8\,M_\odot$ (as shown for the $1\,M_\odot$ star in Figure 1.16) cannot reach the necessary temperature to ignite the carbon burning. At the end of their evolution they eject their outer layers due to radiation pressure creating a so called planetary nebula. The hot core of the star remains as a *white dwarf*, which slowly cools down.

Stars with masses around $10\,M_\odot$ reach temperatures where carbon and oxygen burning is possible. However, either carbon or oxygen will, in this mass range, ignite explosively. This explosion in form of a *supernova*, one of the brightest and most energetic events observable, is likely to destroy the whole star. The remnants of this explosion, the so called *supernova remnant*, will be visible for several thousand years.
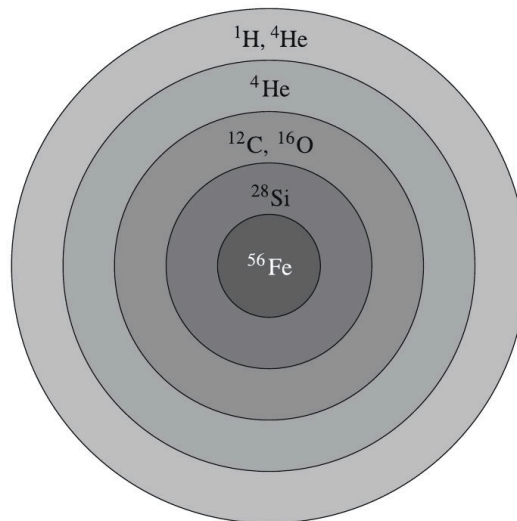

Figure 1.17: The structure of an evolved $30\,M_\odot$ star. Nuclear burning shells separate different layers. Source: Karttunen et al., 2007

In stars with masses even higher than $10\,M_\odot$ none of the fusion phases ignite

explosively. The fusion processes can go on until there is an iron core left (for stars with more than $15\,M_\odot$), surrounded by several burning shells of the previous fusion states. (see Figure 1.17). When the nuclear fusion comes to an end with iron, the core pressure drops and the iron core collapses. While falling down onto the collapsed core, the outer layers heat up very fast and an explosive nuclear fusion is triggered. All outer layers are ejected in this kind of supernova explosion. The iron atoms disintegrate during the core collapse to neutrons, protons and electrons. Due to the high pressure, the electrons and protons recombine to neutrons, which leaves a compact object mainly consisting of neutrons with about a solar mass and a radius of about $10\,km$. This compact object is called a *neutron star*. When the initial mass of the star was even higher (above about $50\,M_\odot$), the mass of the iron core will be so high, that the neutron star cannot withstand its own gravity. Since there is no stable configuration for such high densities the core is likely to collapse into a so called *black hole*.

1.4.2 Compact Objects

As the end product of stellar evolution, there are three kinds of compact objects: white dwarfs, neutron stars, and black holes. Since neutron stars and black holes are involved in most targets LOFT is interested in, they are briefly described in this section. A comprehensive discussion of these objects, including white dwarfs, can be found in Shapiro and Teukolsky, 2008.

Neutron Stars

As described in the previous section, neutron stars are the product of a core collapse of an old massive star, one way to trigger a supernova. When the iron core has a mass above the Chandrasekhar limit of about $1.4\,M_\odot$ the pressure of the electron gas can not withstand the gravitational attraction. Therefore the collapse does not stop at a white dwarf configuration but the contraction goes on. During the collapse, the URCA process (Gamow and Schoenberg, 1941) is of special importance. Usually, the following to reactions form the URCA process:

$$(Z, A) + e^- \rightarrow (Z - 1, A) + \nu_e$$
$$(Z - 1, A) \rightarrow (Z, A) + e^- + \bar{\nu}_e$$
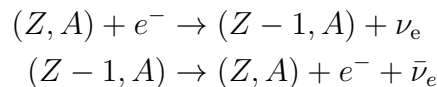
where Z is the proton number, A is the nucleon number, e^- is an electron, ν_e and $\bar{\nu}_e$ are the electron neutrino and anti-neutrino. However, in a degenerate electron gas, the second reaction is forbidden by Pauli's exclusion principle. Therefore almost all protons are converted into neutrons reducing the binding energy of the nuclei. At densities of $10^{17}\,kg/m^3$, no more nuclei exist. The pressure of the degenerate neutron gas opposes the gravitational attraction. The radius of a neutron star is expected to be between $7\,km$ to $15\,km$.

Figure 1.18 shows the structure of a neutron star. The neutron star has an atmosphere of only a few centimeter above its solid metal crust. Beneath the crust, with increasing density towards the center, there is mantle of a neutron superfluid. In the center of the neutron star, where the density is expected to be above 10^{18} kg/m³, there could be a solid core of hyperons or quark matter. Neutron stars have very strong magnetic fields, e.g. the neutron star inside the Crab nebula is expected to have a magnetic field of 5×10^{12} G at its magnetic poles. The magnetic field most likely originates from the progenitor star and has been compressed during the core collapse. As a first approximation the magnetic field of a neutron star can be seen as a dipole field.

The neutron star carries not only the magnetic field of its progenitor star, but also, due to the conservation low, its angular moment. Since the radius of the neutron star is much smaller than the radius of its progenitor star, the neutron star has to spin rapidly. Typical spinning frequencies of neutron stars are several hundred Hertz. It is this rapid spinning, which makes neutron stars preferred targets of X-ray timing analysis.
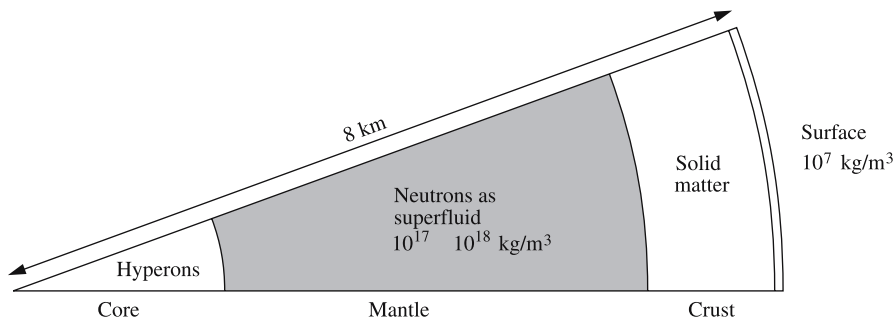

Figure 1.18: Structure of a Neutron Star. Source: Karttunen et al., 2007

Black Holes

When the mass of the iron core of a massive old star is higher than the Oppenheimer-Volkoff limit of about $1.5 \, M_\odot$ to $1.5 \, M_\odot$, there is no stable configuration where the pressure can withstand the gravitational attraction. The core will collapse into a so called black hole. Nothing, not even light, can escape from a black hole. Classically the escape velocity v_e can be calculated as:

$$v_\mathrm{e} = \sqrt{\frac{2GM}{R}}$$

where G is the gravitational constant, M is the mass of the object, and R is the radius, from which the escape starts. A critical radius for the speed of light $(v_\mathrm{e} = c)$ can be calculated as:

$$R_\mathrm{S} = \frac{2GM}{c^2}$$

Beneath the radius R_S, the so called Schwarzschild radius, not even light can escape from the black hole. Surprisingly, a calculation based on general relativity yields exactly the same result. Since no information from beneath the Schwarzschild radius can leave the black hole, it has an event horizon at the Schwarzschild radius. Therefore not much information about the configuration of the black hole can be observed from outside the even horizon. The only observable properties are: mass, angular momentum, and electric charge. There is no reason to be believe that black holes have a significant net electric charge. However, the black hole carries the angular momentum of its progenitor star and is therefore expected to spin very fast.

Today, there are about 20 known compact objects with masses above $3\,M_\odot$. Since this mass is above the Oppenheimer-Volkoff limit, these objects are black hole candidates. Many phenomena in the center of galactic nuclei can be explained with supermassive black holes, with masses of $10^6\,M_\odot$ to $10^9\,M_\odot$. This is possible since there is no upper mass limit for black holes.

So far, the most direct way known to observe a black hole, is when it accretes matter. The radiation of the in-falling matter, powered by its loss of gravitational energy, is visible in the X-ray range as it is described in the next Section.

1.4.3 X-ray Binaries

X-ray binaries are binary star systems with one regular star and one compact object (neutron star or black hole, as described in the previous section). The compact object accretes matter from its companion, which therefore is also called the donor star. When the the donor star is a (massive) O, B, or BE star, the system is called a high mass X-ray binary (HMXB), if the donor star is of type A or later, it is classified as a low mass X-ray binary (LMXB). The energy for the X-ray emission comes mainly from the gravitational energy, which is released, when the accreting material falls onto the compact object. Only a compact object with its deep gravitational potential can provide enough energy to explain the observed X-ray radiation. If the compact object is a white dwarf, the X-ray emission from the binary is weak ($< 10^{33}\,$erg/s) due to its comparatively large radius (about a factor of 700 larger than neutron star radii) and can only be seen when the system is nearby (within $100\,$pc). In the following part of this section only X-ray binaries with neutron stars and black holes as compact objects are considered.

High-Mass X-ray Binaries

In HMXBs, the donor star usually is a massive early-type star with a strong stellar wind, which feeds the accretion of the compact object. The early-type star is so bright in the optical band that it completely dominates the optical spectrum of the binary whereas the X-ray spectrum is completely dominated by the compact object. The visibility of both stars allows to determine the mass of the stars via
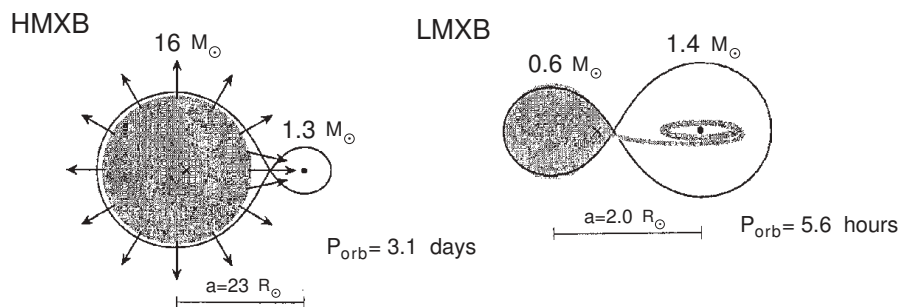
Figure 1.19: Accretion in an HMXB due to the stellar wind and in an LMXB due to the Roche lobe overflow. Source: Trümper and Hasinger, 2007

the orbital parameters of the system in the same way as it is possible for optical binaries. The mass function $f(M)$ (Trümper and Hasinger, 2007) is defined as

$$f(M) = \frac{M_{\mathrm{X}}^3 \sin^3 i}{(M_{\mathrm{X}} + M_{\mathrm{C}})^2} = \frac{PK^3}{2\pi G}$$

where M_{X} is the mass of the X-ray emitting compact object, M_{C} is the companion (or donor) mass, i is the inclination under our viewing angle, P is the orbital period, and K is "the amplitude of the Doppler curve that gives the line-of-sight component of the radial velocity of the companion" (Trümper and Hasinger, 2007). P and K can be measured optically to define the mass function. In order to determine the mass of the compact object it is necessary for the inclination and the mass of the companion to be known. Methods using spectroscopy and photometry to determine both inclination and companion mass, are described in Orosz et al., 2002.

In this way it was possible to determine the mass of many neutron stars. The upper mass limit for neutron stars is important for the neutron star equation of state, which to study is one of the two primary science goals of LOFT (see Section 2.2.1).

Accreting X-ray pulsars are HMXBs, in which mass is accreted onto a neutron star. At some point below the Alfven radius[11], the magnetic field of the neutron star becomes so strong that the material can only move along the field lines. All the in-falling material is directed to the magnetic poles, where it hits the surface. If the accretion rate is high, the in-falling material causes a hot X-ray emitting shock. The X-rays cannot radiate into all directions since there is more in-falling matter above the poles. The X-rays are emitted sideways, which is called a fan beam (see Figure 1.20 a). When the accretion rate is lower, the in-falling material does not cause a shock, which allows the X-rays to escape through the accreting material in the direction of the magnetic field lines in form of a pencil beam (see Figure 1.20 b; Basko and Sunyaev, 1975). In general, the axis of the magnetic

---

[11]The Alfven radius is the radius where the magnetic field density equals the kinetic energy density of the accreted matter.

poles and the rotation axes are inclined to each other, which causes the magnetic pole to rotate through the field of view of the observer. This so called lighthouse effect causes observers to see X-ray pulsations (Meszaros, 1984). Accreting X-ray pulsars will be observed with LOFT as part of the observatory science (see Section 2.2.3).
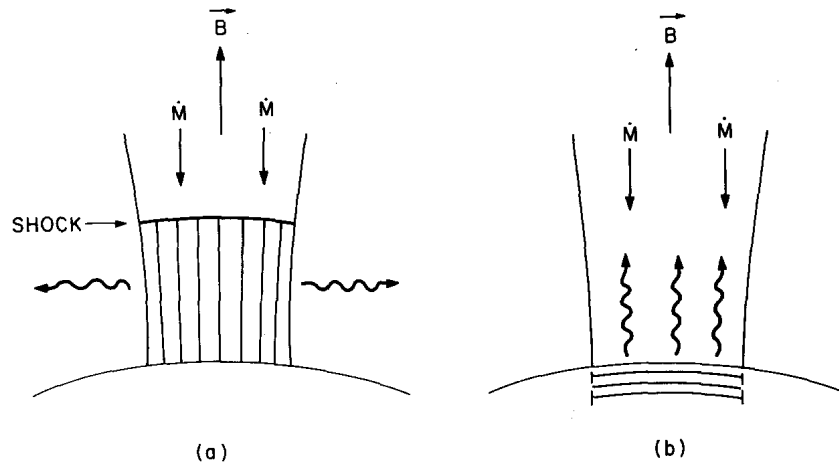

Figure 1.20: Geometry of the emission region of accreting X-ray pulsars. a) For high accretion rates a fan beam is emitted whereas for low accretion rates b) a pencil beam is emitted. Source: Meszaros, 1984

Low-Mass X-ray Binaries

Low-mass X-ray binaries are binary systems with a compact object (neutron star or black hole) and a companion, which is of spectral type A or later with a mass smaller than $2\,\mathrm{M}_\odot$. The evolved companion eventually fills its Roche lobe[12] and transmits matter through the inner Lagrangian point L_1 into the potential of the compact object. The matter ejected this way has a lot more angular momentum than the material of stellar winds, which is why an accretion disk is formed. Accretion in LMXB is described in more detail later in this section.
There are 150 known LMXB with orbital periods from $0.19\,\mathrm{h}$ to $17\,\mathrm{days}$ (Liu, van Paradijs, and van den Heuvel, 2001).
Most of the neutron stars in low-mass X-ray binaries are expected to be old and therefore have a weak magnetic field since the magnetic field decays over time. Due to their low magnetic fields LMXB are, usually no pulsars. However, X-ray bursts and quasi periodic oscillations (QPOs) can be observed in LMXB. The low magnetic field also allows an equatorial accretion of matter onto the neutron star surface. Thereby, a part of the angular momentum associated with the accreted

---

[12]The Roche lobe of a star is defined by the equipotential plane, which touches the same equipotential plane of the other star in the inner Lagrangian point L_1.

matter, is effectively transfered to neutron stars, which therefore can, over a long time, spin-up to ms periods.

Type-I X-ray Bursts

X-ray bursts are a very abrupt increase of X-ray emission. Within $10\,\text{s}$ to $100\,\text{s}$ (Strohmayer and Bildsten, 2003) an energy of about $10^{39}\,\text{erg}$ is emitted. In the first second the luminosity rises in all parts of the X-ray spectrum equally. The decay, however, shows a tail in the lower energy part of the X-ray spectrum ($2\,\text{keV}$ to $6\,\text{keV}$) whereas it is very sharp at higher energies ($6\,\text{keV}$ to $30\,\text{keV}$). This means that the temperature decreases during the burst. At the beginning of the burst the temperature is about $30 \times 10^6\,\text{K}$ and it cools down to $15 \times 10^6\,\text{K}$ within a few $10\,\text{s}$.

These observations are very well explained by thermo-nuclear flashes on the surface of an accreting neutron star in a LMXB. The accreted hydrogen on the neutron star surface undergoes nuclear burning and therefore produces helium. The helium is collected below the steadily burning hydrogen until a critical temperature and density is reached and the helium ignites and starts fusing into carbon. As opposed to the hydrogen burning, the helium burning is unstable and the whole helium is burned at once in a thermo-nuclear flash, which causes the abrupt increase of X-ray emission.

During X-ray bursts so called *burst oscillations* (see Figure 1.21; Strohmayer and Bildsten, 2003) can be observed. Even though they are not completely understood, they clearly seem to be linked to the neutron star rotation. After the ignition of the thermo-nuclear flash, the burning front does not spread symmetrically over the neutron star surface. Thereby a brightness pattern on the neutron star surface is created, which causes oscillations due to the neutron star rotation.

Quasi Periodic Oscillations

Rapidly varying low mass X-ray binary sources were found with periods from $25\,\text{ms}$ to $50\,\text{ms}$. They cannot be explained with the neutron star rotation because the frequencies are too low and most important, an object as massive as a neutron star could not vary its rotation frequency so fast. As the frequency of these oscillations increases with the luminosity the period is not stable. Therefore these oscillations are called quasiperiodic oscillations (QPOs). They were discovered by Michiel van der Klis in the 1980s (van der Klis et al., 1985).

Since the QPOs cannot directly represent the rotation of the neutron star, another model is needed: The QPO frequency can be described as the difference between the rotation frequency of the neutron star and the rotation frequency of the inner disk. Consider a matter clump orbiting the neutron star very close. The magnetic field of the neutron star, rotating under the clump, acts as a barrier, which prevents the clump from falling onto the neutron star. Only when the clump is over the magnetic poles matter can fall onto the surface and cause an X-ray flash. Quasi
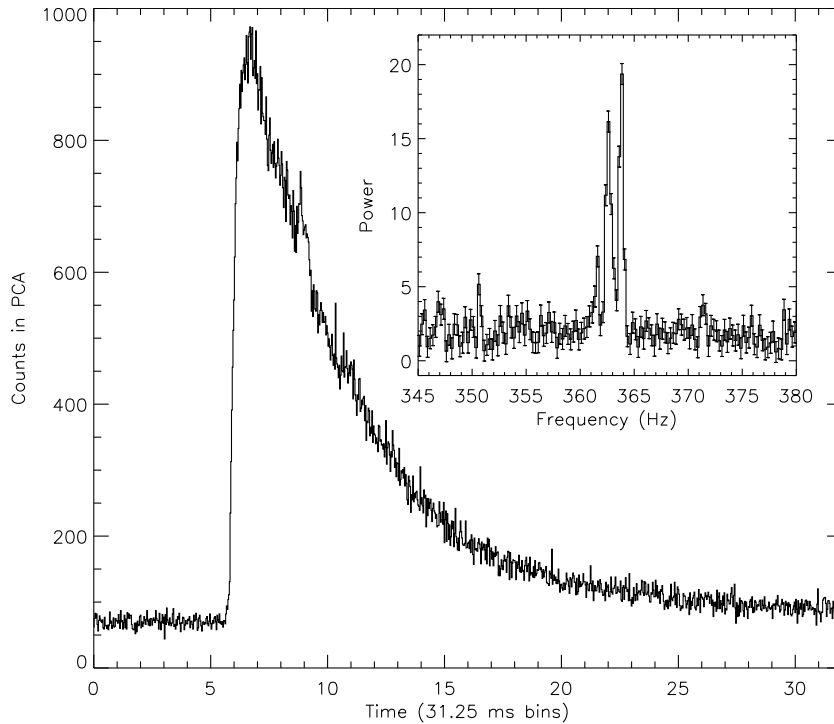
Figure 1.21: Type-I X-ray burst from 4U 1728-34 as it was observed with RXTE/PCA. The main panel shows the PCA counts over time whereas the insert panel shows the power spectrum with a burst oscillation at 353 Hz. Source: Strohmayer and Bildsten, 2003

Periodic Oscillations in the rise of Type-I X-ray bursts will be examined by LOFT (see Section 2.2.1).

In 1996, kHz QPOs have been detected with RXTE by Strohmayer et al. (1996) and van der Klis et al. (1996). For neutron stars, the kHz QPOs always appear as twin frequencies with the peaks separated by about 300 Hz to 400 Hz. This difference is close to the frequency expected for the neutron star rotation whereas the peak frequency is close to the orbital frequency in the inner part of the accretion disk. This strongly suggests an explanation that involves beat frequencies between the neutron star rotation and the rotation in the inner accretion disk. LOFT will be able to discriminate between different models explaining kHz QPOs, see Section 2.2.2.

Black Hole Binaries

Black hole binaries are X-ray binaries, where the compact object is a black hole. It is not straight-forward to determine whether a compact object is a black hole or a neutron star. When X-ray bursts or pulsations are observed, the compact object has to be a neutron star. The most direct way to identify a black hole is to show that there is no material surface and that effects of general relativity can be found, which are truly unique in the vicinity of the event horizon of a black

hole. Such effects include a big gravitational red shift, light bending or particles moving very close to the speed of light. LOFT will contribute to the observations of general relativity effects in this strong-field regime (see Section 2.2).

Today, the most practical way to identify a compact object as a black hole is to determine its mass, as described above in this section. According to general relativity, there is no stable configuration for a compact object with a mass above $3\,M_\odot$. Therefore, compact objects with such a mass are considered to be "secure" black holes. Today, there are 20 known compact objects with a mass above $3\,M_\odot$ (Remillard and McClintock, 2006). So far, all known stellar mass black holes have been discovered in binaries, and X-ray observations are the only known way to discover black hole binaries. Only three (Cyg X-1, LMC X-1, LMC X-3) of the 20 known stellar mass black holes are persistent sources. It is noteworthy that all of them were found in HMXB, whereas the other 17 transient sources were all found in LMXB. More information on black hole binaries can be found in Remillard and McClintock, 2006.

Accretion in Low-Mass X-ray Binaries

In a LMXB, the companion (or donor star) fills its Roche lobe. The Roche lobe of a star in a binary system is defined as the equipotential plane, which touches the same equipotential plane of the other star of the system in the inner Lagrangian point L_1 (see Figure 1.22). Matter of the donor star can flow through L_1 into the potential of the compact object. This is called Roche lobe overflow. Due to its large angular momentum, the overflown matter cannot be directly accreted onto the compact object. Therefore a thin *accretion disk* is formed around the compact object. The gas forming the accretion disk is rotating in Keplerian orbits with the velocity

$$v = \sqrt{\frac{GM}{r}}$$

where G is the gravitational constant, M is the mass of the compact object, and r the radius. This describes a differential rotation of the disk with the inner layers rotating faster than the outer ones. Angular momentum is transported to the outer regions of the disk due to the viscosity. This allows the matter of the inner part of the disk to move further inwards. While moving inwards the matter is heated by the viscosity. In this way, half of the potential energy is converted into rotational energy, the other half is converted into thermal energy. The thermal energy is emitted as blackbody radiation with luminosity L

$$L = \frac{GM\dot{M}}{2R}$$

where $\dot{M}$ is the accretion rate and R the radius of the compact object. This accretion model, as it is described in Shakura and Sunyaev, 1973 is sometimes referred to as standard accretion model.
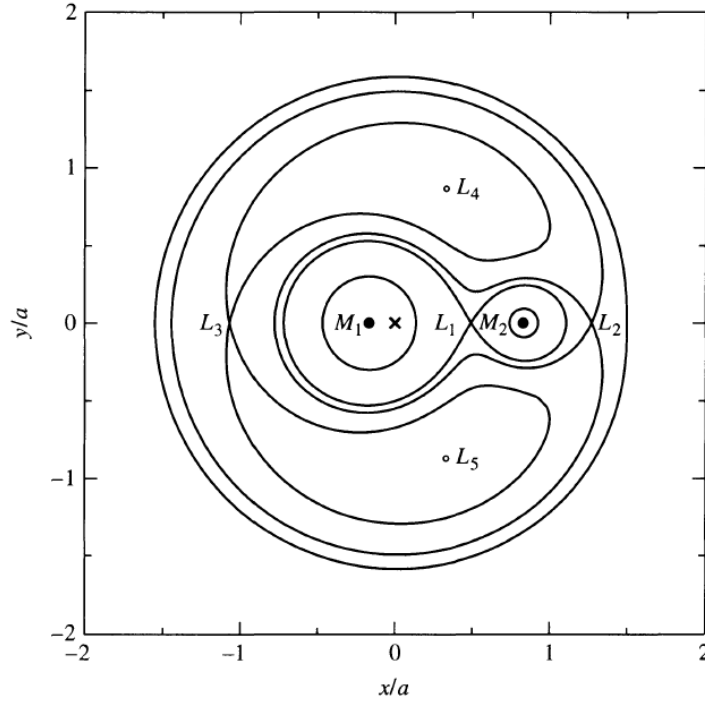
Figure 1.22: Equipotentials in a binary system. $M_1 > M_2$. The x denotes the center of mass. The Roche lobe is the equipotential, which goes through the inner Lagrangian L_1. Source: Carroll and Ostlie, 2007

While the radius of a neutron star is well-defined, for a black hole, the radius of the innermost stable circular orbit (ISCO[13]) is relevant in this context. The ISCO of a non-spinning Schwarzschild black hole is $R_{\mathrm{ISCO}} = 3R_{\mathrm{S}}$. In the inner part of the accretion disk of a black hole (near the ISCO) the temperature is about 10^7 K. The maximum of the blackbody radiation caused by this temperature is in the X-ray range (cf. Section 1.1.1).

Most neutron stars in LMXB have low magnetic fields (below 10^7 G), which is why they are no pulsars. The low magnetic field does not interfere with the accretion very much, allowing the accretion disk to be extended very close to the neutron star surface. The radius of the ISCO of a $1.4\,\mathrm{M_\odot}$ black hole, however, is also in the same range as the neutron star radius: $R_{\mathrm{ISCO}} = 3R_{\mathrm{S}} = 12\,\mathrm{km}$. Therefore, the accretion disk of an $1.4\,\mathrm{M_\odot}$ neutron star and an $1.4\,\mathrm{M_\odot}$ black hole are expected to be very similar.

There is one significant difference, which should allow to differentiate between the spectrum of a neutron star binary and a black hole binary: The neutron star has a solid surface, which gets heated by the kinetic energy of the accreted matter. This should add a second blackbody component to the spectrum.

---

[13]Innermost Stable Circular Orbit (ISCO): In Newtonian Mechanics there is no ISCO, because the gravitational potential is always $\propto 1/r$. In general relativity, however, the gravitational potential deviates from an $1/r$ potential in the vicinity of the central object and therefore there are no stable orbits below the ISCO.
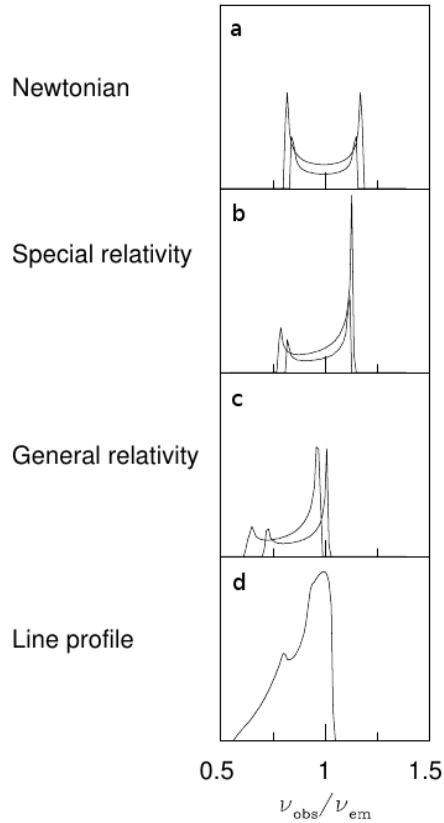
Relativistic Iron Lines

The physical processes in active galactic nuclei (AGN) and black hole binaries are believed to be very similar (Mirabel, 2007). Relativistically broadened iron K-lines have been found in Seyfert Galaxies (Fabian et al., 2000; Nandra et al., 2007) as well as in black hole binaries (Frontera et al., 2001; Miniutti, Fabian, and Miller, 2004). These lines are expected to originate from the innermost part of the accretion disk. The line broadening is caused by several (cumulative) effects (see Figure 1.23). The classical Doppler effect causes a symmetric double peak due to the disk rotation. Special relativity causes the blue peak to be much stronger, since the light emitted by matter moving towards the observer is beamed into the direction of the observer. The transverse Doppler effect shifts the whole peak towards longer wavelengths. General relativity causes another red-shift due to the gravitational potential, from which the light is emitted.

Due to the very hot temperature and the high radiation pressure, there is a hot corona around the disc, which emits hard X-rays. The disk is irradiated by the corona and reflects the X-rays from the corona causing the continuum part of the spectrum with a Fe K absorption edge. The irradiation also causes the Fe Kα fluorescence line, which is broadened as described above.

Figure 1.23: Broadening of the Kα line according to Fabian et al., 2000. (a) shows the symmetric Newtonian double peak from the classic Doppler shift. (b) includes the relativistic Transverse Doppler shift and the relativistic Beaming. The line in (c) is red-shifted due to the gravitational redshift. (d) shows the line profile as a result of all these effects integrated over a part of the disk.

Broadened iron lines have not only been observed from black holes but also from neutron star LMXBs (Asai et al., 2000). However, in neutron star LMXBs also non-broadened iron lines have been observed (Suzuki et al., 1984). These non-broadened iron lines are located at 6.7 keV instead of 6.4 keV which indicates that the iron, where those line originate from, is highly ionized. The difference between these systems is not yet understood. See Section 2.2.2 on how LOFT will be able to contribute to this field.

2 LOFT

The following chapter about LOFT is based on the original LOFT Proposal (LOFT Consortium, 2012c), on the Payload Definition Document (LOFT Consortium, 2012b), on the Mission Requirements Document (LOFT Consortium, 2012a), and on the Science Requirements Document (LOFT Consortium, 2012d). Unfortunately, these documents are not publicly available. They can be requested on-demand from A. Santangelo[1]. Publicly available information on LOFT can be found in Belloni and Bozzo, 2012; Feroci et al., 2012; and also on the LOFT website (LOFT Consortium, 2013).

2.1 Mission Overview

The Large Observatory For X-ray Timing (LOFT, see Figure 2.1) is an M3[2] mission candidate in ESA's Cosmic Vision program. If selected, the launch will be between 2022 and 2024 with a Soyouz launcher. The targeted low earth orbit (LEO) has an altitude of about $600\,\mathrm{km}$ and an equatorial inclination below $5.24°$. The nominal mission duration of LOFT is 4 years.

The main instrument of LOFT is the Large Area Detector (LAD), a collimated instrument for highly time resolved spectra based on Silicon Drift Detectors (SDD) with an effective area of $10\,\mathrm{m^2}$ at $8\,\mathrm{keV}$. It will be able to do sub-millisecond spectroscopy with fluxes as low as $300\,\mathrm{mCrab}$[3]. With a typical $10\,\mathrm{ks}$ exposure, LOFT will be able to study active galactic nuclei (AGNs) with fluxes of about $1\,\mathrm{mCrab}$ with a signal to noise ratio (SNR) of 500. A $1\,\mathrm{ks}$ observation of a $3\,\mathrm{mCrab}$ AGN will suffice to detect the broad iron line in the spectrum.

The LAD is accompanied by the Wide Field Monitor (WFM), a coded mask instrument with a large detecting $(1.5\,\pi)$ field of view centered at the pointing of the LAD. The main tasks for the WFM are long term monitoring of bright sources and to find X-ray transients. It produces images in eight different energy bands and additional data products such as spectra and rate meters.

---

[1]santangelo@astro.uni-tuebingen.de

[2]ESA's third call for medium missions.

[3]$1\,\mathrm{Crab}$ corresponds to the flux of the Crab nebula at the respective energy range. $1\,\mathrm{mCrab} = 2.4 \times 10^{-11}\,\mathrm{erg\,cm^{-2}\,s^{-1}}$ ($2\,\mathrm{keV}$ and $20\,\mathrm{keV}$). Matt et al., 1997
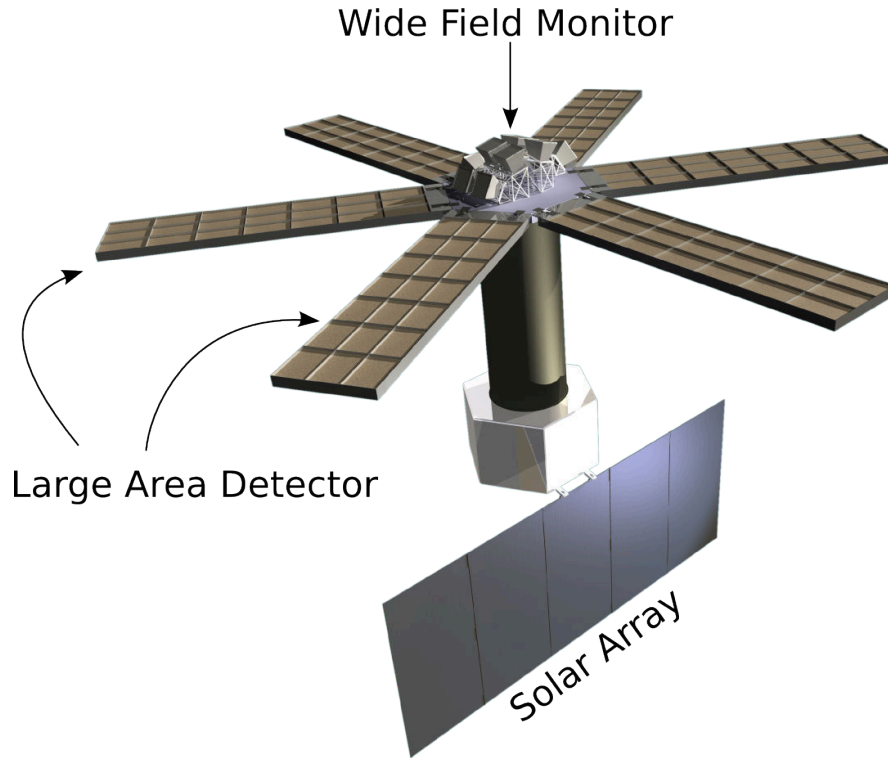
Figure 2.1: Design sketch of the Large Observatory For X-ray Timing (LOFT). The Large Area Detector (LAD) consists of six detector panels (brown), the Wide Field Monitor (WFM) consists of five camera units. Source: INAF-IAPS, CSIC-IEEC

2.2 Scientific Goals

LOFT observations will contribute to answer two main questions related to the ESA Cosmic Vision theme 'matter under extreme conditions':

- What is the equation of state of matter in neutron stars?

- Does matter orbiting close to the event horizon of black holes follow the predictions of general relativity?

The scientific goals are divided into three main fields: 1) Dense Matter and 2) Strong Field Gravity, which are the primary science goals of LOFT, and 3) Observatory Science. The following sections will introduce these fields in more detail.

2.2.1 Dense Matter

The physics of densities much higher than atomic core densities ($\gg 10^{14}\,\mathrm{kg/m^3}$) is yet unknown and beyond the scope of any earthbound laboratory. These densities can be found in neutron stars (NS; Karttunen et al., 2007), which makes

Table 2.1: Maximum Masses of Neutron Stars according to different equation of states. Source: Shapiro and Teukolsky, 2008

Equation of State	Max. Mass [$M_\odot$]
R with charged-pion condensation (π)	1.5
Reid (R)	1.6
Bethe-Johnson (BJ)	1.9
Three-nucleon interaction (TNI)	2.0
Tensor Interaction (TI)	2.0
Mean Field (MF)	2.7

astrophysics an important probe for theories like quantum chromodynamics. Exotic states of matter like Bose condensates, hyperons or even strange quark matter could be found inside neutron stars (Akmal, Pandharipande, and Ravenhall, 1998). The existence of these states of matter is closely linked to the different equations of state (EOS), which describe the relationship between pressure and density. There, mass and radius of a neutron star as well as the maximum mass of neutron stars are important parameters to observe. "Soft"[4] EOSs predict a maximum mass of 1.5 solar masses whereas the "stiffest" EOSs predict maximum masses up to 2.7 solar masses, see Table 2.1 (Shapiro and Teukolsky, 2008).

Mass and Radius Measurements

While it is possible to determine neutron star masses precisely with the observation of radio pulsars (Thorsett and Chakrabarty, 1999), simultaneous constrains of mass and radius are expected to come from X-ray observations. One of the most promising possibilities to determine mass and radius of neutron stars is to model pulse profiles of accreting ms pulsars in LMXB. The pulsations are caused by the brightness pattern of the spinning neutron star. A 'hot spot' on the surface caused by in-falling matter from the accretion disk emits X-rays. Gravitational self-lensing makes it possible to see parts of the back hemisphere and, therefore, to see the spot longer. This and other relativistic effects, such as frame-dragging, Doppler boosting, or gravitational red-shifts, strongly depend on the ratio between mass and radius (M/R) of the neutron star. Simulations based on RXTE[5] data similar to those by Strohmayer (2004) have been performed by the LOFT consortium (LOFT Consortium, 2012c) and show that LOFT will be able to achieve the required precision of 5 % (90 % confidence) in mass and radius observations to constrain the EOSs.

Another very promising way to determine mass and radius of neutron stars is to model pulse profiles of oscillations in the rise of Type-I X-ray bursts (see Sec-

---

[4]A soft equation of state means matter is more compressible. Therefore, a neutron star of the same mass has a smaller radius with a softer EOS.

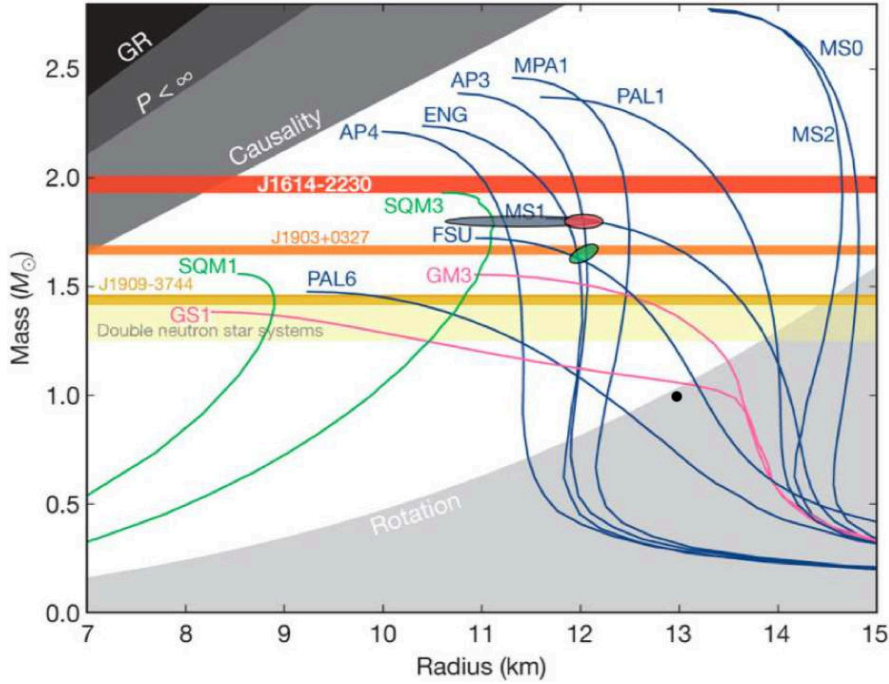[5]Rossi X-ray Timing Explorer (see Section 1.3.1).

Figure 2.2: Mass-Radius diagram of neutron stars. Curves represent different EOSs (blue: nucleonic matter, pink: nucleonic plus exotic matter, green: strange quark matter). Horizontal bars: masses from binary radio pulsars. Top left: excluded by general relativity and causality. Bottom right: excluded by centrifugal break-up of the highest frequency pulsar known (716 Hz). Ellipses: Derived 90 % confidence interval (with < 5 % uncertainty) of M and R for a simulated pulse profile, as observed by LOFT, of: the rising phase of a Type-I X-ray burst (green), of SAX J1808.4-3658, the first millisecond X-ray pulsar discovered (gray) and Swift J1749.4-2807, the first eclipsing millisecond X-ray pulsar (red). The difference of the uncertainty of the red and the gray ellipse is mostly due to different system inclinations. Source: LOFT Consortium, 2012c

tion 1.4.3): When the accreted helium envelope of the neutron star ignites, the burning front spreads over the surface for about 1 s, during which oscillations can be observed due to the spinning of the neutron star. Besides these two methods the large area oft LOFT will allow to "exploit continuum spectral modeling in photospheric radius expansion bursts, or global seismic oscillations during intermediate flares of magnetars" (Feroci et al., 2012). See Figure 2.2 for examples on how LOFT could constrain the EOS using M and R measurements.

2.2.2 Strong-Field Gravity

General relativity (GR) has not been tested in the strong-field regime yet. Effects such as frame dragging or an innermost stable circular orbit, that have so far been

tested in the weak- and intermediate field regime, can be tested by LOFT for the very first time with high precession in the strong-field regime. Such effects can be observed from the inner part (i.e. within a few Schwarzschild radii for black holes, or close to the surface for neutron stars) of the accretion disk around black holes and neutron stars. Observing QPOs (van der Klis, 2000) with frequencies associated with the matter moving in the innermost part of accretion disks in LMXB or even active galactic nuclei (AGN) allows to detect strong-field gravity effects. Another way is to observe the relativistically broadened and red-shifted iron Kα line (Fabian et al., 1989), originating from the innermost part of accretion disks from neutron stars and black holes in binaries, as well as supermassive black holes in AGNs. In the following part of this section, there are two examples given of how LOFT will be able to exploit these effects.

Millisecond Quasi Periodic Oscillations

Up to now there are about 40 known accreting compact objects oscillating at a millisecond timescale (LOFT Consortium, 2012d) corresponding to the inner parts of their accretion disks. These Quasi Periodic Oscillations (QPOs), with frequencies of up to 450 Hz for black holes (BH) and up to 1250 Hz for neutron stars, are not yet fully understood. There are competing theories that explain these QPOs, e.g.: The relativistic epicyclic resonance model (Abramowicz and Kluźniak, 2001), which predicts static frequencies and the relativistic precession model (Stella, Vietri, and Morsink, 1999) which predicts a time evolution of the frequencies. It is not possible to discriminate between those models with current instruments like RXTE (see Figure 2.3a) because the sensitivity does not allow for measurements within the coherence time of the millisecond QPOs. However, with the large area of LOFT/LAD (see Figure 2.3b) it will be possible to observe the time evolution of these QPOs within their coherence times and therefore to discriminate between those models.

Fe K-alpha line

Observations of the Fe Kα fluorescence line originating from the innermost part of the accretion disks of compact objects in LMXB or supermassive black holes in AGNs are another independent possibility to probe strong-field general relativity effects (Fabian et al., 1989). Section 1.4.3 explains how the Fe Kα fluorescence line (see Section 1.1.1) is broadened by various (relativistic) effects: The Newtonian and the relativistic Doppler effect cause the line to appear as a red-shifted, broadened double peak. Relativistic beaming makes the blue peak stronger and another red-shift is caused by the gravitational potential. As current simulations show, LOFT will be able to measure the profile and variability of the Fe Kα line with unprecedented accuracy. With a 1 ks exposure LOFT will be able to "collect more than 5×10^5 counts in the 2 keV to 30 keV energy range for a 3 mCrab AGN" (LOFT Consortium, 2012b).
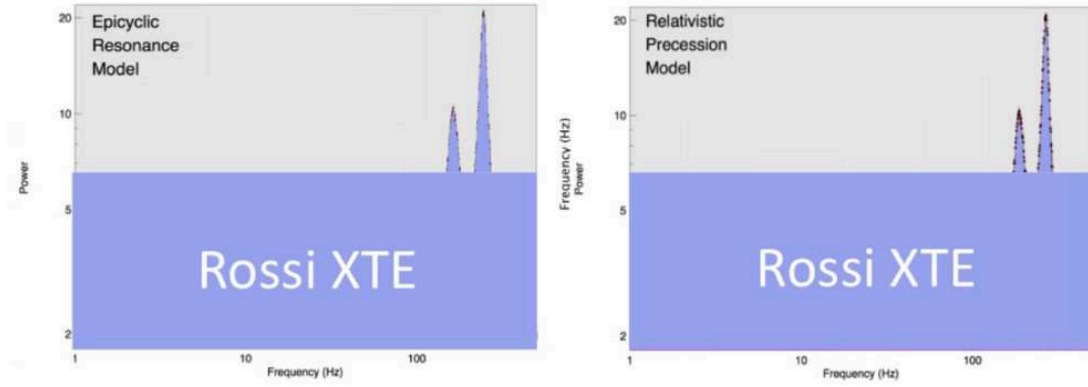
(a) Observed with RXTE
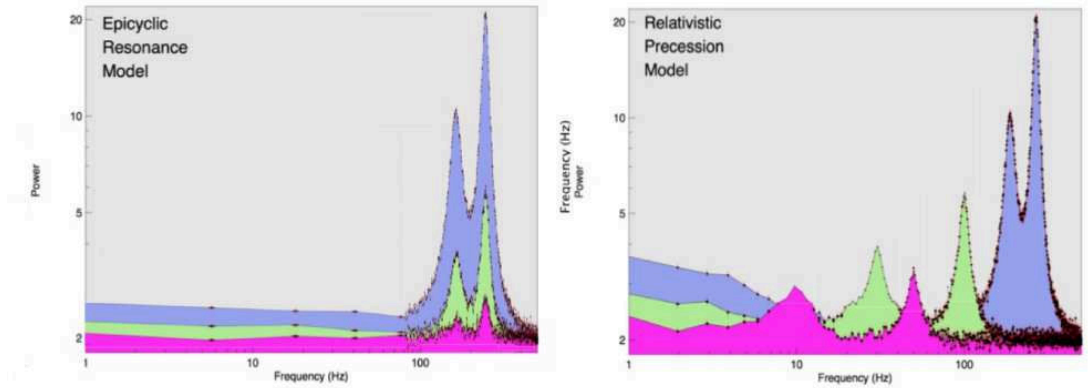
(b) Observed with LOFT

Figure 2.3: Simulations for millisecond black hole QPOs (Belloni and Bozzo, 2012). Time evolution within the relativistic epicyclic resonance model (left) and the relativistic precession model (right). Exposure time is 16 ks for all curves and the intensity is 1 Crab (blue), 400 mCrab (green) and 300 mCrab (pink).

A comprehensive summary of the primary science goals of LOFT can be found in Feroci et al., 2012.

2.2.3 Observatory Science

While LOFT is designed with a focus of achieving the primary science goals it is also very suitable for additional observations involving X-ray variability: The WFM observations and about 60 % of the observing time of the LAD will be used for Observatory Science. The target objects for the LOFT observatory science are listed in Table 2.2.

Current missions have found indications for absorption edges in the spectra of a subset of Type I X-ray bursts, the so called extreme radius-expansion bursts (in't Zand and Weinberg, 2010). These edges are probably caused by nuclear burning

ashes and might be used to determine the compactness of the neutron star. It is very difficult to observe extreme radius-expansion bursts with pointed observations since they occur unpredictably and infrequently. The WFM, however, will be able to observe these bursts with their absorption edges (see Figure 2.4) and to verify whether it is actually possible to determine the compactness of neutron stars utilizing these absorption edges.

The WFM is also very suitable for the detection of Gamma Ray Bursts (GRBs) or X-ray flashes. It could be able to detect absorption features in the GRB caused by the circum-burst material which would give valuable information about the progenitor object. The LAD will contribute to the observatory science, too. Triggered early by the WFM it will—for example—be able to observe how jets are launched in new transient X-ray sources: Cross-correlations with optical and infrared observations allow to measure the jet speed by looking at how long it takes for the material to propagate from the hot X-ray emitting inner part to the outer part where optical and infrared radiation is produced. This method would also work for systems where the jet cannot be resolved spatially.

Other topics are the observation of already known sources which will include the continuation of the work of RXTE with a much higher sensitivity.
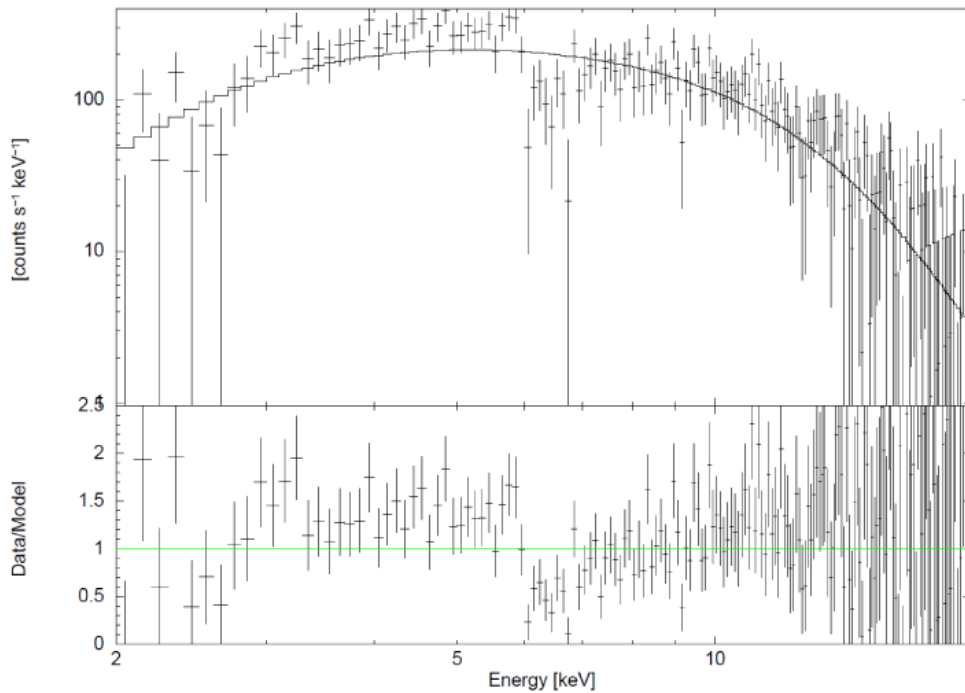

Figure 2.4: Absorption Edges in extreme radius-expansion bursts. A 5 Crab X-ray burst has been simulated with a $\tau = 1$ absorption edge at 6 keV. A LOFT WFM observation with a exposure of 1 s can detect the edge. Source: LOFT WFM-SIM Group, as cited in Belloni and Bozzo, 2012

Table 2.2: Target objects for the LOFT observatory science. Source: LOFT Consortium, 2013

Object	Accretion/ Ejection Physics	Strongly Magnetized Objects	Cosmic Explosions	Cosmol. Meas.	Transient Phenomena
Accreting White Dwarfs	LAD, WFM	LAD	LAD, WFM		LAD, WFM
Low-Mass X-ray Binaries	LAD, WFM	LAD, WFM			LAD, WFM
LMXB – X-ray Bursters	LAD, WFM		LAD, WFM		LAD, WFM
High-Mass X-ray Binaries	LAD, WFM	LAD, WFM	LAD, WFM		LAD, WFM
Isolated Neutron Stars		LAD			LAD
Magnetars		LAD, WFM	LAD, WFM		LAD, WFM
Flare Stars		LAD			LAD, WFM
Nearby Galaxies	LAD, WFM	LAD, WFM	LAD		LAD
Tidal Disruption Events	LAD, WFM				LAD, WFM
Seyfert, Blazars	LAD, WFM				LAD, WFM
Gamma-ray Bursts	WFM		WFM	WFM	WFM
X-ray Background Fluctuations				LAD	

2.3 Instruments

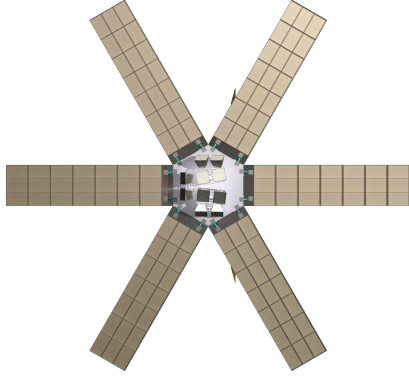### 2.3.1 Large Area Detector (LAD)

Figure 2.5: The Large Area Detector (LAD) with its six panels. The Wide Field Monitor (WFM) is in the middle. Source: INAF-IAPS, CSIC-IEEC

The Large Area Detector (see Figure 2.5) is a collimated instrument for highly time resolved spectroscopy. Its most important key parameter is the large effective area of $12\,\text{m}^2$ at $8\,\text{keV}$ (see Figure 2.7). This size is possible due to recent developments in the size of monolithic silicon drift detectors (SDD).

The design of the LAD is very hierarchical (see Figure 2.6). It consists of six identical panels, each of which consists of 21 detector modules with each module containing 16 monolithic silicon drift detectors. One detector is divided into two (almost) independently operated detector halves. There are 112 anodes per detector half, handled by 7 ASICs. This is a total of 451 584 anodes or 28 224 ASICs for the LAD. To handle this large number of anodes it is necessary that the electronics design (see Chapter 3) follows the hierarchy of the mechanical design. Table 2.3 shows the key parameters of the LAD.

Table 2.3: Key parameters of the LAD

The requirements are determined by the scientific goals.

|	Requirement	Goal
Geometrical Area	N/A	$18\,\text{m}^2$
Effective Area @ 8 keV	$10\,\text{m}^2$	$12\,\text{m}^2$
Time resolution	$10\,\text{μs}$	$7\,\text{μs}$
Energy range (nominal)	$2\,\text{keV}$ to $30\,\text{keV}$	$1.5\,\text{keV}$ to $30\,\text{keV}$
Energy range (extended)	$30\,\text{keV}$ to $80\,\text{keV}$	$30\,\text{keV}$ to $80\,\text{keV}$
Energy resolution @ 6 keV (all events)	$260\,\text{eV}$	$200\,\text{eV}$
Energy resolution @ 6 keV (singles only)	$200\,\text{eV}$	$160\,\text{eV}$
Field of View	$0.9°$ to $1.1°$	$0.45°$ to $0.55°$
Max flux	15 Crab	30 Crab
Dead time @ 1 Crab	$< 1\,\%$	$< 0.5\,\%$
Power consumption	N/A	$713\,\text{W}$
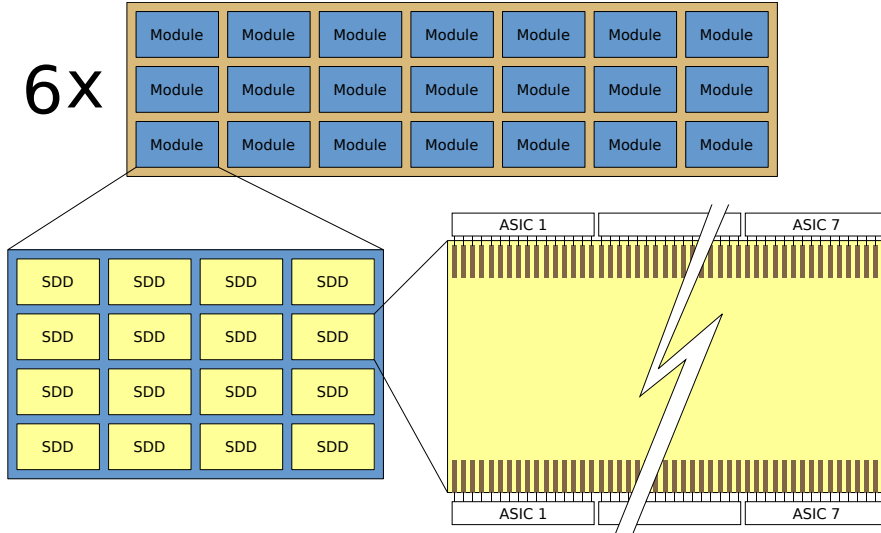
Figure 2.6: LAD Hierarchy. The LAD consists of six identical panels (brown), each of which consists of 21 detector modules (blue) with each module containing 16 monolithic silicon drift detectors (SDD, yellow). One detector is divided into two (almost) independently operated detector halves. There are 112 anodes per detector half, handled by 7 ASICs.

LAD – Silicon Drift Detector

The history and the general working principle of silicon drift detectors (SDD) are described in Section 1.2.1. For the LOFT LAD design, the following key parameters[6] are most important: large area, high timing resolution, high energy resolution, small weight and low power consumption. Therefore a silicon drift detector is a suitable choice: An energy resolutions of 137 eV has been reached with SDDs (Lechner et al., 1996). Their timing resolution is only limited by the maximum drift time, which is in the order of µs and their small weight of about $1 \, \mathrm{kg \, m^{-2}}$ allows for large areas aboard spacecrafts.

The SDD used for LOFT is an optimized version of the silicon drift detector developed for the Inner Tracking System in the ALICE experiment of the Large Hadron Collider (LHC) at CERN (Vacchi et al., 1991; Rashevsky et al., 2002). With 450 µm thick 6″ wafers it is possible to produce 76 cm² (70 mm × 108 mm) monolithic detectors. The anode pitch of 970 µm is the result of an optimization towards low power consumption and high energy resolution. The maximum drift time of 7 µs is the main uncertainty in the arrival time and therefore defines the constraints of the time resolution.

The SDD used for the LAD is shown in Figures 2.8. An incident photon creates a charge cloud inside the detector, which is proportional to its energy. High voltage applied to the cathodes generates a drift field of $370 \, \mathrm{V \, cm^{-1}}$ causing the

---

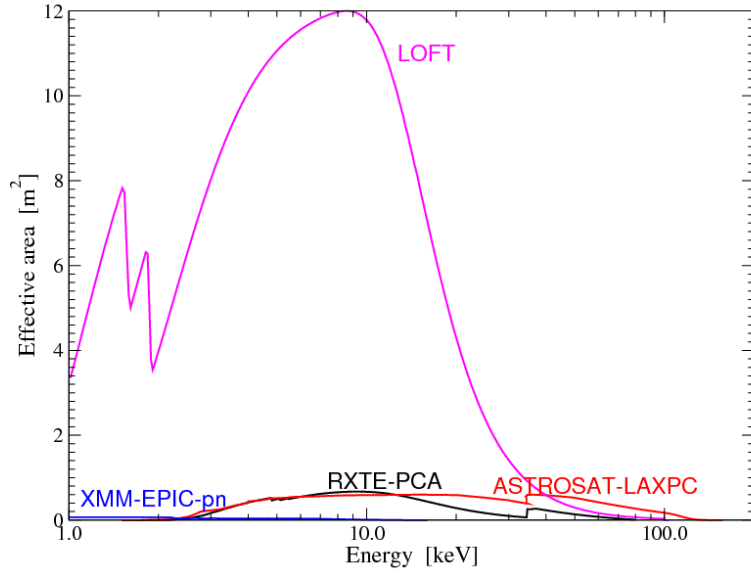[6]Since the LAD is a collimated instrument spatial resolution of the detector is not important.

Figure 2.7: The effective area of the LAD (goal) compared to X-ray timing instruments of other missions. Source: LOFT Consortium

electrons to drift towards the anodes with a velocity of $5\,\text{mm}/\mu\text{s}$. The electron cloud accumulates at one or two anodes which can be read out. If the incident photon interacts on the center-axis of an anode, the whole charge cloud gets absorbed by this one anode (single anode event, $40\,\%$ of all events). If the incident photon interacts in between two anodes, the charge cloud splits up (double anode event, $60\,\%$ of all events). During the drift the charge cloud gets bigger due to diffusion. This means the closer the incident photon hits to the middle of the detector, the bigger the chances are for a double anode event. Due to the relatively large pitch of $970\,\mu\text{m}$ no more than two anodes can be hit by one cloud.

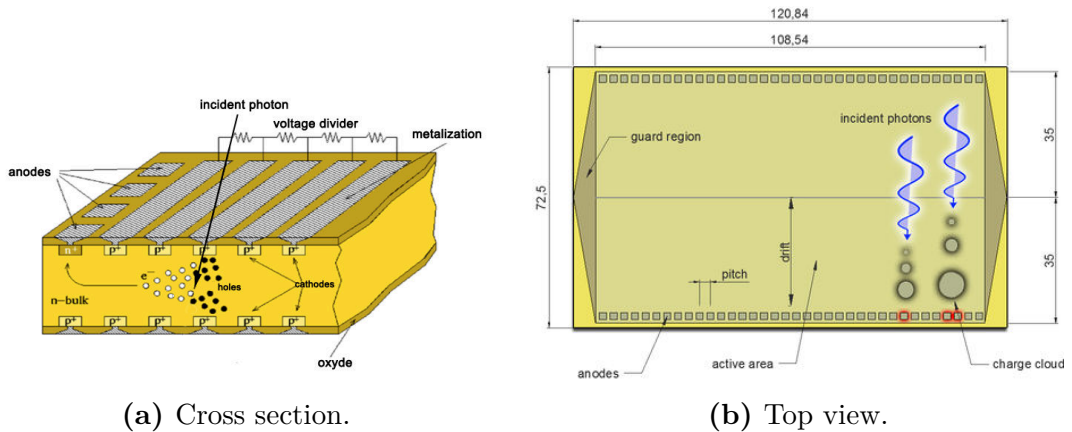
(a) Cross section.

(b) Top view.

Figure 2.8: The silicon drift detector used for the LAD. a) The charge cloud created by an incident photon drift towards the anodes, where it can be read out. b) Depending on the position where the incident photon hits the detector, the charge cloud is accumulated at one or two anodes. Source: LOFT Consortium, 2012b

LAD – Collimator

The Collimator determines the field of view of the LAD and the energy-dependent off-axis background . In the current configuration, led silicate glass micro-capillary plates based on the same technique as micro channel plates, are going to be used as the collimator for the LAD. The micro-capillary plates are based on the EXOSAT[7] and the BepiColombo[8] Mercury Imaging X-ray Spectrometer (MIXS) heritage, see Figure 2.9. While the stopping power of the lead glass is sufficient below 30 keV, it becomes transparent above 30 keV or 40 keV. This results in a higher background for these energies, which however can be handled very well since there are no variations in time to be expected. The size of a collimator tile will be 8 cm × 11 cm so that the whole active area of one detector is covered by only one collimator. The key parameters of the LOFT LAD collimator are described in Table 2.4. Other configurations for the collimator are currently being studied.

Table 2.4: Key parameters of the LAD collimator.

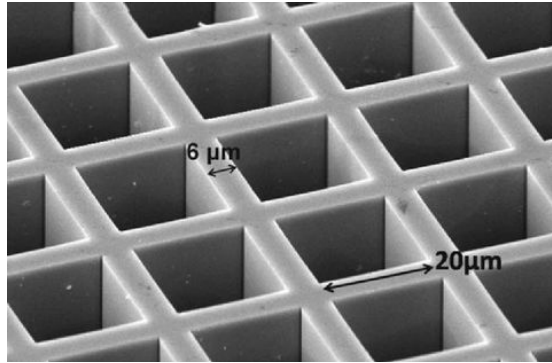| Parameter	Value
Pore size	$100\,\mu m$
Septal thickness	$20\,\mu m$
Open area fraction	$70\,\%$
Channel aspect ratio	60:1
Channel length	6 mm
Lead oxide fraction	$\sim 37\,\%$
Background Leakage	acceptable up to 30 keV

Figure 2.9: Scanning Electron Microscope image of the BepiColombo MIXS collimator with a pore size of $20\,\mu m$ and a wall thickness of $6\,\mu m$. A similar collimator will be used for the LOFT LAD. The values for LOFT are described in Table 2.4. Source: LOFT Consortium, 2012b

---

[7]The European X-ray Observatory Satellite (EXOSAT), launched in 1983, was ESA's first satellite mission entirely devoted to X-ray observations.

[8]BepiColombo is an ESA mission to Mercury scheduled for launch in 2015.

LAD – Module

16 Detectors of the LAD are arranged as a 4 x 4 grid in one Module (see Figure 2.10a). The Module contains the mechanical structure to mount the detectors and collimators as well as the electronics necessary to read out the detector (ASICs on the Front End Electronics) and to perform the event reconstruction (Module Back End Electronics).

The co-alignment of all collimator tiles is very important for the pointing accuracy which again is important to achieve the field of view goal. In order to reduce alignment errors all collimator tiles are held in one large Aluminum frame. The co-alignment will be tested in calibration facilities in later phases.
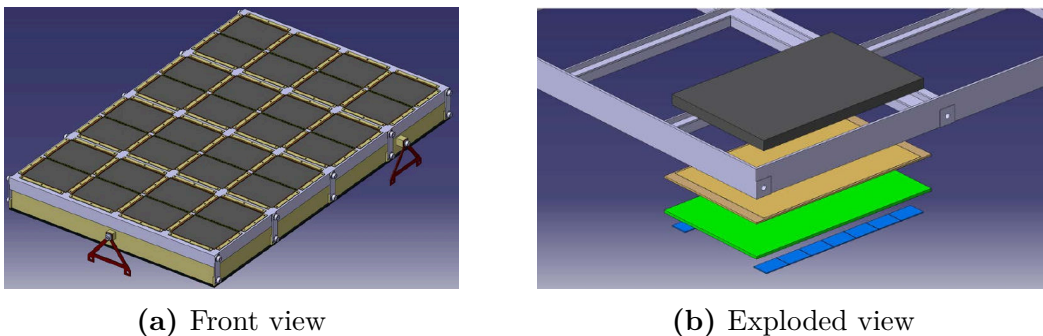

(a) Front view

(b) Exploded view

Figure 2.10: (a) Front view of a Detector Module with 16 detectors aligned in an 4 x 4 grid. (b) shows the collimator tile in grey, the detector in brown, the Front End Electronics in green and seven ASICs on each side of the detector in blue. Source: LOFT Consortium, 2012b

The Module Back End Electronics (MBEE), which validates an event and applies calibration data to reconstruct the photon energy, is mounted on the back side of the Module. Due to the large cabling harness between the MBEE and the Front End Electronics (FEE) the MBEE is split up into two boards. This makes it easier to handle both, all the wires and the amount of data. For more detail on the FEE–MBEE interface see Section 3.2.3.
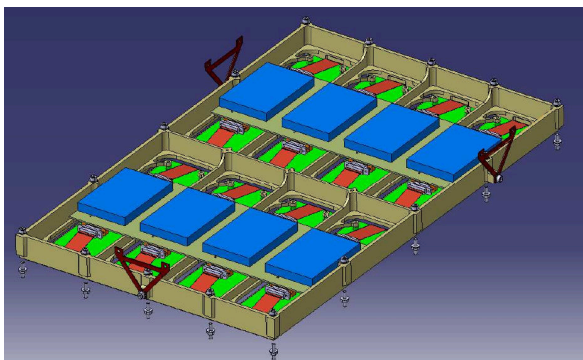

Figure 2.11: Rear view of the Module. The blue boxes are radiators mounted on the Printed Circuit Boards of the MBEE (dim green) to cool the electronics passively. The wires between the FEE (bright green) and MBEE are red. The MBEE is split up into two boards which makes it easier to interface the detectors. Image by Berend Winter (MSSL).

LAD – Panel

Figure 2.5 shows the 6 panels of the LAD, each of which contains 21 modules aligned as a 3 x 7 grid. The Panel Back End Electronics (PBEE), which collects the event data from the 21 modules, is likely going to be mounted on the panel as well, so less cables have to cross the panel hinge to the spacecraft. The mechanical structure of the panels (see Figure 2.12) is developed by industry partners, including a deployment mechanism, which was also used for the SMOS[9] ESA mission. During launch, the panels are in a hinged position, which allows the large detector area to fit into a Soyuz rocket. When LOFT is successfully inserted into orbit, the panels can be deployed. The co-alignment of the panels as well as the co-alignment of the modules in each panel is as important as the alignment of the detectors within one module in order to achieve an accurate pointing.
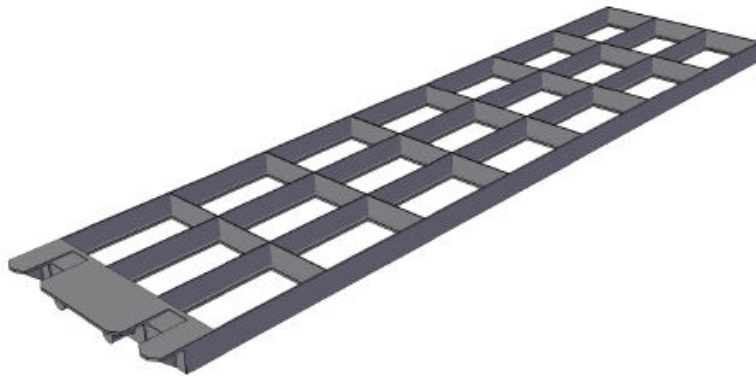

Figure 2.12: Mechanical structure of one Detector Panel. Source: LOFT Consortium, 2012b

2.3.2 Wide Field Monitor (WFM)

The Wide Field Monitor (see Figure 2.13a) is a coded mask instrument with a field of view (FOV) of $1.5\,\pi$ FWZI (Brandt et al., 2012). It is co-aligned with the pointing of the LAD. Its main tasks are to trigger on active sources for the LAD, to perform long term monitoring of bright sources and to identify X-ray transients (especially Gamma Ray Bursts). Additionally the WFM notifies ground stations within the LOFT Burst Alert System (see Section 2.3.2) to allow fast follow-up observations with ground bases telescopes. For the specifications of the WFM see Table 2.5. Compared to the all-sky monitor (ASM) of RXTE (see Section 1.3.1) the WFM has a better angular resolution ($3'$ to $5'$ instead of $20'$ and a higher energy resolution ($300\,\text{eV}$ to $500\,\text{eV}$ instead of only three energy bands). While the ASM needs to rotate in order to scan the sky, the WFM simultaneously monitors a large fraction of the sky, which increases the probability to detect transient events.

---

[9]The Soil Moisture and Ocean Salinity (SMOS) mission is an ESA earth observatory, launched in 2009.
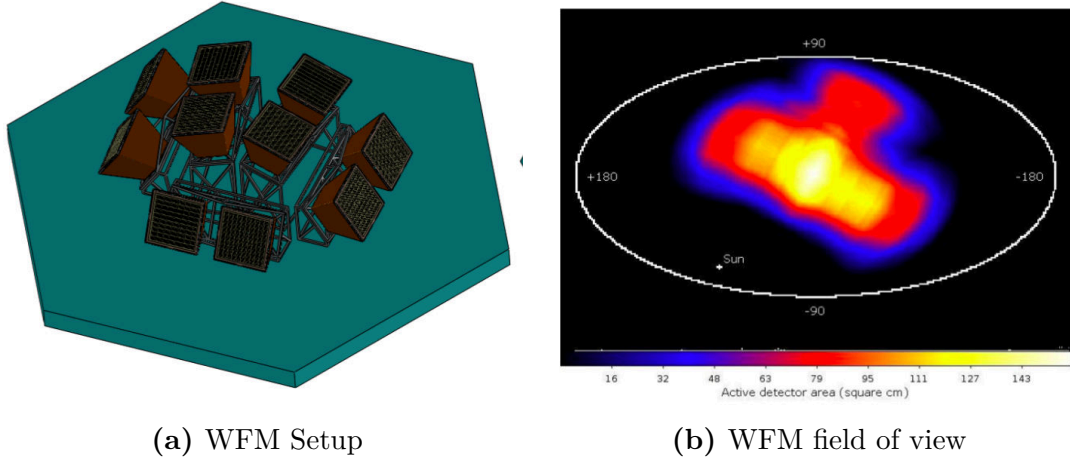
(a) WFM Setup

(b) WFM field of view

Figure 2.13: WFM Setup and Field of View. (a) The Units are arranged in a way to cover as much of the sky as possible with a good resolution. (b) All-sky map of the active detector area in Galactic coordinates for an observation on April 1st of the Galactic Center. The separate Unit facing the viewer is in the anti-sun direction to increase the field of view. This is reflected in the top right corner in (b). Source LOFT Consortium, 2012b

Table 2.5: Key parameters of the WFM

The requirements are determined by the scientific goals.

	Requirement	Goal
Angular resolution	5′	3′
Sensitivity (5 σ, 1 s)	1 Crab	0.2 Crab
Sensitivity (5 σ, 50 ks)	5 mCrab	2 mCrab
Field of view	1π sr	1.5π sr
Energy range (primary)	2 keV to 50 keV	1.5 keV to 50 keV
Energy range (extended)	50 keV to 80 keV	50 keV to 80 keV
Energy resolution @ 6 keV	500 eV	300 eV
Alert Broadcast	< 30 s after event for 75 % of the events	< 20 s after event for 75 % of the events
Power consumption (peak)	N/A	109 W

WFM – Detector

The WFM uses the same SDD technology (see Section 2.3.1) as the LAD. The most significant modification of the SDDs for the WFM is a smaller anode pitch of 145 µm. For the cost of a decreased energy resolution the smaller anode pitch increases the spatial resolution of the SDD. It allows also a localization of the incident photon in the drift direction: After the energy reconstruction of the event the drift distance can be determined with an accuracy of about 5 mm. This takes

advantage of the effect that the size of the charge cloud gets bigger the longer the drift distance is (diffusion). The coded mask reflects the different resolution in the two dimensions with a fine structure in one direction (250 µm) and a coarse structure in the other direction (16 mm). Because of the high resolution in one dimension and the very low resolution in the other dimension the detector is also called a 1.5D detector.

WFM – Unit

Each of the ten WFM cameras consists of four silicon drift detectors in the detector plane, a coded mask (see Section 1.2.2 for the working principle), and a shield in order to reduce background due to photons coming from outside the field of view. One camera can locate a source within an angle of a few arcmin in the high resolution direction and a few degrees in the low resolution direction. A WFM Unit (see Figure 2.14) consists of two 1.5D cameras oriented at 90° to have an arcmin resolution in both directions.
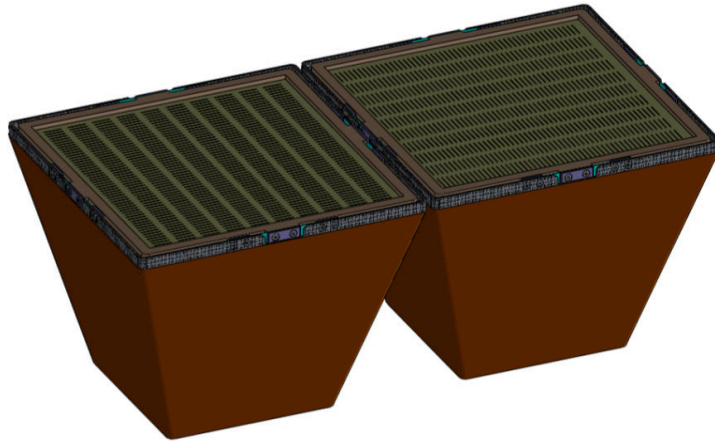

Figure 2.14: Wide Field Monitor Unit. One WFM Unit consists of 2 orthogonally aligned cameras, each of which consists of 4 Silicon Drift Detectors, shields, and a coded mask. Source: LOFT Consortium, 2012b

WFM – Data products and Burst Alert System

During normal science operations of the WFM, there are a primary and three secondary data products which are generated: The primary data product is the photon-by-photon event data, which is required to create the secondary data products:

- images: every 300 s in 8 or 16 energy bands.

- detector rate meters: 8 energy bands, 16 ms resolution

- energy spectra: every 30 s, full energy resolution

These secondary data products are regularly transmitted to ground during each telemetry pass. The photon-by-photon event data is usually not transmitted due to telemetry restrictions. However, there is a triggering algorithm employed in order to detect X-ray transients (new sources or changes in flux) on different time scales up to 300 s. If this algorithm detects a significant variability in flux, the image is reconstructed on-board. This demands a large amount of computing power because several discrete fast Fourier transformations (DFFT) have to be performed. Therefore, a special board will process these DFFTs and calculate the position of the transient source.

Once the position of the source in the image is known it is transformed to a position on the sky (making use of the pointing knowledge). The position will be compared to an on-board database of known X-ray sources and if the transient is unknown, it will be send to ground immediately using the LOFT Burst Alert System (LBAS). The LBAS is a network of VHF[10] ground stations covering almost the whole orbit of LOFT. Using the LBAS, the position and time of 75 % of the bursts can be transmitted to ground within 20 s to 30 s after occurrence enabling fast follow-up observations with ground based telescopes. If a burst has been confirmed, the photon-by-photon event data is stored and transmitted during the next regular telemetry pass.

Summary

At the beginning of this chapter, the Large Observatory For X-ray Timing (LOFT) has been introduced as an ESA M3 mission candidate for a launch opportunity between 2022 and 2024. The science goals of LOFT have been briefly described. The physics of dense matter and especially the neutron star equation of state as well as the effects of general relativity in the strong-field regime, which can be observed close to black holes or neutron stars, are the primary science goals of LOFT. The WFM observations and about 60 % of the LAD observation time will be dedicated to observatory science.

The two scientific instruments of LOFT have been described in the second part of this chapter. With $12\,\mathrm{m}^2$ the effective area of the LAD is is an order of magnitude larger than the effective area of all previous X-ray observatories. The high sensitivity achieved with such a large area, allows for time resolved spectroscopy in the sub-millisecond range. The WFM, a coded mask instrument with a large field of view, monitors the sky for transient events. It provides triggers for the LAD, creates images and spectra, and notifies ground stations of transient events in order to allow fast follow-up observations with ground based telescopes. Since the scope of this thesis is on the development of the Module Back End Electronics (MBEE) for the LAD, the next chapter describes the electronics design of the LAD only.

---

[10]Very High Frequency (VHF) denotes the radio frequency range from 30 MHz to 300 MHz.

3 LAD Electronics Design

The electronics design of the LAD reflects the hierarchy of the instrument itself. For each detector there is one Front End Electronics (FEE). Each Module, containing 16 detectors, has its own Module Back End Electronics (MBEE) and each of the six panels, consisting of 21 Modules each, its own Panel Back End Electronics (PBEE). This means that one MBEE interfaces 16 FEEs and one PBEE interfaces 21 MBEEs. The Data Handling Unit (DHU) collects the data from the six PBEEs and prepares them for transmission before it hands the data over to the On-Board Data Handling system (OBDH).
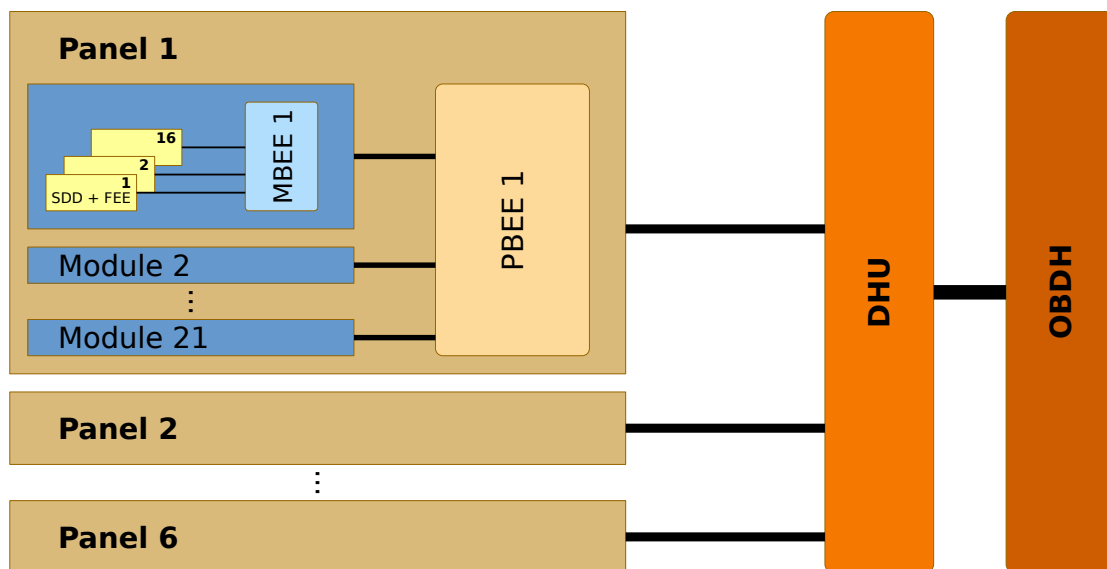

Figure 3.1: Electronics Design of the Large Area Detector. The electronics design reflects the hierarchy of the instrument. 16 Detectors with their respective Front End Electronics (SDD + FEE) are read out by one Module Back End Electronics (MBEE). The 21 MBEEs on each panel transmit event packets to their respective Panel Back End Electronics (PBEE). The six PBEEs pass the processed data to the Data Handling Unit (DHU), where it is prepared for transmission, before it is handed over to the On-Board Data Handling system (OBDH). Source: based on a figure of LOFT Consortium, 2012b

---

This chapter is based on the LOFT Payload Definition Document (LOFT Consortium, 2012b) but also includes recent design changes.

3.1 Front End Electronics (FEE)

The Front End Electronics is the first stage of the hierarchical electronics setup. There is one FEE for each detector. Its main task is to read out the 112 anodes on each half of the detector. This is done with ASICs[1], currently developed at IRAP, Toulouse. One ASIC reads signals from 16 anodes, so that there are 7 ASICs necessary per detector half. The ASICs will detect and report a trigger in order to create a trigger map[2] and perform the analog/digital (A/D) conversion. In addition, the FEE is responsible to distribute the high-, medium-, and low system voltages provided by the MBEE. As the FEE is developed at SRON, Utrecht, it is out of the scope of this thesis. More information on the FEE can be found in Zane et al., 2012.

3.2 Module Back End Electronics (MBEE)

In the hierarchy of the electronics the Module Back End Electronics is between the Front End Electronics and the Panel Back End Electronics. It is connected to the 16 FEE boards of one module with their two detector halves each. The MBEE reads out the event data, verifies whether an event is valid or not and applies calibration data to the event in order to perform the energy reconstruction (see Figure 3.2). Afterwards it passes the processed event packets on to the Panel Back End Electronics. *The data processing pipeline as well as a hardware prototype of the MBEE have been developed within this thesis.*

3.2.1 MBEE Tasks

The main tasks of the LAD Module Back End Electronics are:

time tagging: For a timing mission it is crucial that each event is precisely tagged with the time of its occurrence. A 20-bit timestamp allows time tagging with microsecond resolution. For time tagging the MBEE receives a stable 1 MHz clock from the panel which is synchronized once per second with a GPS Pulse Per Second signal distributed by the Data Handling Unit through the PBEE to all modules.

trigger validation and filtering: Triggers can not only be caused by incident photons but also by minimum ionizing particles (MIPS), which makes it necessary to validate the trigger first. When a trigger occurs, the whole detector half is handled as one unit. After a short coincidence window, all 7 ASICs are requested to send their 16-bit trigger map to the MBEE, which makes an overall trigger map of 112 bits. Each bit stands for one of the 112 anodes

---

[1]Application-Specific Integrated Circuit

[2]This is a 112 bit value—1 bit for each anode—indicating which anodes have triggered, i.e., have reached a charge above a configurable threshold.
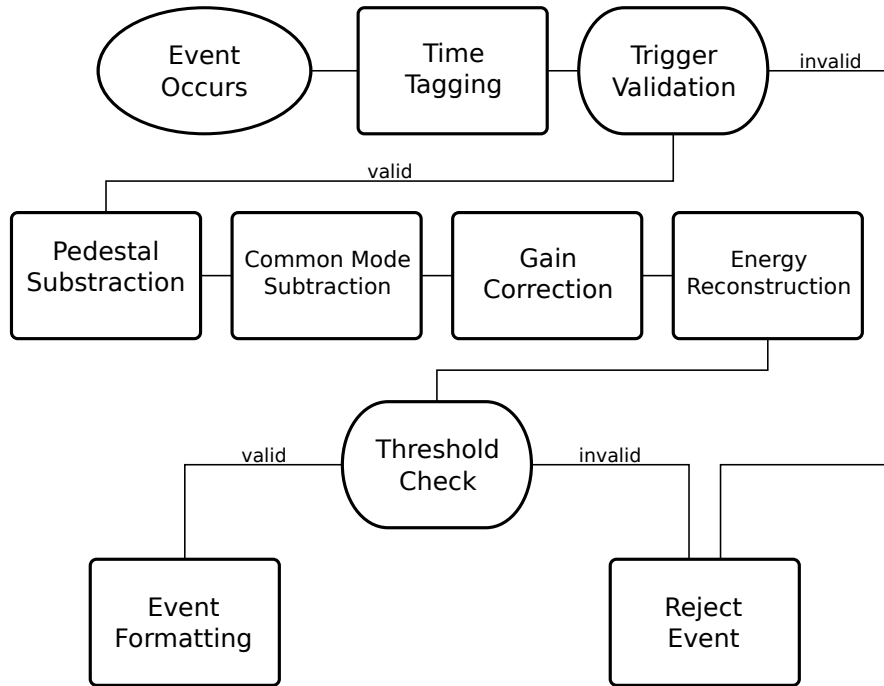
Figure 3.2: Flow chart of the event reconstruction inside the MBEE.

and indicates whether the respective anode has triggered (1) or not (0). The event is considered valid if only one anode alone or two adjacent anodes have triggered. Otherwise the trigger is most likely caused by minimum ionizing particles and will be rejected.

If the trigger map is valid the MBEE commands the triggered ASICs[3] to perform the A/D conversion and to send all the anode values to the MBEE.

pedestal subtraction: Due to manufacturing tolerances each anode has a different pedestal value. As a first processing step the respective pedestal value is subtracted from each anode value. There is one corresponding pedestal value for each anode stored aboard the MBEE. These values can be determined and updated by on-board calibration or by telecommand from ground.

common mode subtraction: Small variations in the supply voltage of the FEE cause an offset, which is the same for all anodes of one ASIC. The common mode offset is calculated as the median of all non-triggered anodes from the respective ASIC and is subtracted from all its anode values.

gain correction: The gain varies slightly from anode to anode due to manufacturing tolerances and is also temperature dependent, therefore a gain correction

---

[3]It is possible that a two-anode event is split up between two ASICs if the triggered anodes are anode 16 and anode 1 of the respective ASICs. This means there are 16 anode values to handle if one ASIC is concerned or 32 anode values if two ASICs are concerned. The non-triggered anode values are needed to perform the common mode subtraction.

will be applied. There are gain correction values for a certain calibrated temperature for each anode stored aboard the MBEE. The difference to the actual temperature is accounted for by a linear correction[4] procedure. The storage values can be updated by on-board calibration or by telecommand from ground. The local temperature of the instrument is provided by a separate housekeeping board.

energy reconstruction and threshold: For a two-anodes event the energy must be reconstructed by adding up the two previously corrected anode values. It will be checked whether the reconstructed energy value is within the valid energy range of 2 keV to 80 keV. Otherwise the event will be marked as invalid by a flag and discarded later.

event formatting: In the last step an event packet is built, which can be passed on to the PBEE. The event packet consists of a 9-bit energy value[5], a 20-bit timestamp, and a 3-bit event-id which distinguishes between one or two anode events and non-science packets.

housekeeping: Housekeeping tasks, such as monitoring voltages and temperatures of the system, are performed by a special housekeeping board. While this board is considered to be part of the MBEE it is not within the scope of this thesis.

configure the ASICs: The ASICs of the FEE can be reconfigured by the MBEE with updated trigger thresholds or other configuration data. Single anodes can be turned off to avoid triggers from noisy anodes, if necessary.

3.2.2 MBEE Modes

The MBEE can be set into different modes by the PBEE to account for a variety of circumstances the instrument can be operated in. There are modes used for launch, for passing through the South Atlantic Anomaly (SAA), for calibration and for scientific observations (Zane et al., 2012). The following modes are important for this thesis. Note that the mode of each of the 21 modules on a panel can be set individually:

Science Mode: The Science Mode is used for regular science operations. Each detected photon (in the valid energy range) produces a 32-bit event packet with a 9-bit energy value and a 20-bit timestamp as well as the information about the multiplicity[6] of the event. All other information (ASIC number,

---

[4] $E_{\mathrm{cor}} = E \cdot (1 - C(T - T_0))$. The gain variability factor C is expected to be 0.1 %/K

[5] The binning is about 60 eV for energies below 30 keV and about 2 keV in the expanded range of 30 keV to 80 keV.

[6] The multiplicity of an event provides information about how many anodes are involved in the event, i.e., whether it is a one-anode or a two-anodes event.

anode number, values of non-triggered anodes) is not recorded in Science Mode. The Science Mode is implemented in this thesis and if not stated otherwise all further descriptions refer to the Science Mode.

Engineering Mode: The Engineering Mode is used for calibration and error detection. Depending on what is requested, in Engineering Mode all data can be passed on. Single steps in the processing pipeline can be bypassed. The future implementation of the Engineering Mode is already considered in this version of the MBEE design, but it is not yet fully implemented.

Configuration Mode: The Configuration Mode is used to set new storage values for the MBEE and the ASICs. The PBEE can send new pedestal, gain or threshold values to the MBEE. In Configuration Mode no scientific data is processed by the MBEE. This mode is implemented for the update of MBEE storage values but the ASICs cannot be reconfigured, yet, since the MBEE–ASIC interfaces protocol is not yet determined.

3.2.3 MBEE–FEE Interface

The main purpose of the interface between the Module Back End Electronics and the Front End Electronics is to transmit the digitized anode values from the ASICs on the FEE to the MBEE and to reconfigure the ASICs. It is also used to provide the high- and medium voltages (HV and MV) necessary to operate the Silicon Drift Detector and the low voltage (LV) necessary to operate the ASICs. It is important that the interface allows for a fast data transfer since the transmission time of an event contributes to the detector dead time, but it is also important to reduce the number of wires to a minimum since one MBEE has to interface 16 FEEs. The latest draft for the MBEE-FEE interface is shown in Figure 3.3. The following items describe how the interface works when a photon is detected:

Trigger occurs: One or more anode voltages are higher than the (analog) threshold. The ASIC sets its trigger output signal. The logic OR of the separate trigger signals from the seven ASICs of one detector half is connected to the MBEE. The MBEE is informed about on which detector half the trigger has occurred but not which of the seven ASICs has triggered. The detector dead time starts with the occurrence of the trigger.

Hold: After a short coincidence time window has passed, in which the charge can be accumulated on the anodes, the MBEE sends a HOLD signal to all ASICs of the triggered detector half to freeze the analog voltages.

Request trigger map: The MBEE requires the trigger map to be able to validate the event and to determine which anodes of which ASICs have triggered. There are two data lines per detector half, which can be used simultaneously to transmit the trigger map. The odd numbered ASICs (1, 3, 5) share the
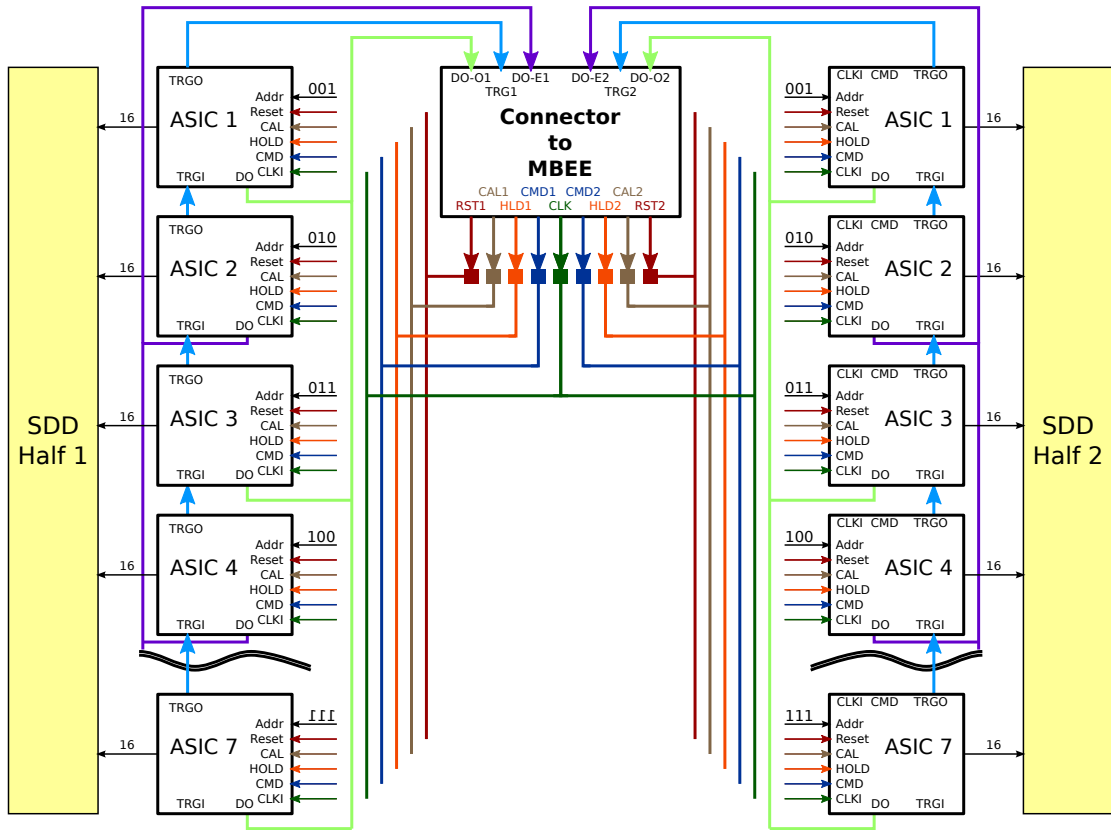
Figure 3.3: MBEE–FEE interface. The diagram shows the interface lines on the FEE. Note the symmetry: One half of the signal lines is connected to the left detector half, the other half of the signal lines is connected to the right detector half, only the CLK signal is shared. See Table 3.1 for an explanation of the signals. Source: based on a figure by Yannick Favre, University of Geneva

> data line DO-O and the even numbered ASICs (0, 2, 4, 6) share the data line DO-E. The MBEE requests the trigger map of two ASICs simultaneously to minimize the detector dead time. This is repeated another three times until the complete trigger map is received.

Validate trigger map: The MBEE determines if the trigger map is valid, i.e., if only a single anode or two adjacent anodes have triggered. If the trigger map is not valid, the reset signal for the ASICs is set and the detector dead time terminates.

Request A/D conversion: If the event has a valid trigger map, the MBEE commands the (up to two) concerned ASICs to perform the A/D conversion of the anode voltages. After the conversion both ASICs send their anode values to the MBEE at the same time using the DO-O and DO-E lines[7]. The

---

[7]Valid events can only involve adjacent ASICs. Therefore one ASIC is always odd-numbered and the other always even numbered.

other ASICs are still on HOLD to ensure a constant detector dead time for the whole detector half.

Reset: If the data transfer is completed, the MBEE sends the Reset signal to the ASICs and the detector dead time is over. Now the MBEE and the ASICs are ready to process a new event.

Interface Lines

The interface has five power lines to provide the FEE with different voltages. Since the two detector halves are handled independently, Table 3.1 describes all signal lines per detector half. The complete interface consists of the five power lines plus two times the signal lines described in Table 3.1. However, the clock signal line is shared between the two detector halves.

Table 3.1: MBEE–FEE interface signal lines per detector half. Signal directions are described from the FEE perspective.

Signal	I/O	Diff	Description
CLK	in	yes	System clock for all ASICs.
HOLD	in	yes	Connected to all seven ASICs. Freezes the analog signals inside the ASICs.
CMD	in	no	Connected to all seven ASICs. Serial command line. Single ASICs can be addressed via protocol with a 3-bit address.
RESET	in	no	Connected to all seven ASICs. Used to clear all circuits (peak holder, trigger logic) after an event has been read out
CAL	in	yes	Connected to all seven ASICs. Used together with HOLD for calibration purposes.
TRIG	out	yes	The logic OR of the trigger output lines of the seven ASICs is connected to the MBEE.
DO-E	out	no	Data Output line shared by ASICs 2, 4, 6
DO-O	out	no	Data Output line shared by ASICs 1, 3, 5, 7

3.3 Panel Back End Electronics (PBEE)

There is one Panel Back End Electronics on each panel. In the hierarchical structure it is between the MBEEs and the Data Handling Unit, which collects the data from all six panels and prepares it for transmission to ground. Since it is not in the main scope of this thesis it is only briefly described. It interfaces all 21 MBEEs on a panel directly and its main tasks are:

- Collecting and buffering event packets from the 21 MBEEs on the panel via the 21 MBEE–PBEE interfaces (see Section 3.3.1).

- Reformatting the event data using differential timestamps to reduce the amount of data, which needs to be transmitted to ground.

- Creating spectra and re-bin data according to the observation mode: The Event-by-Event Mode is possible up to intensities of 500 mCrab. At higher intensities the telemetry limit would be exceeded in the Event-by-Event Mode. The PBEE creates (user-defined) spectra to reduce the total amount of data.

- Interfacing the Data Handling Unit (DHU) via a SpaceWire[8] Link to pass on the science data and to receive commands.

- Housekeeping: Collect and reorganize the housekeeping data from all 21 MBEEs on the panel.

- Configuring the MBEEs: Set the mode of the MBEEs individually or send new configuration values like pedestal and gain values to a MBEE.

3.3.1 MBEE–PBEE Interface

The purpose of the MBEE–PBEE interface is to transmit event packets from the MBEE to the PBEE and to send commands in the opposite direction. There is one interface between each of the 21 MBEEs and the PBEE of a panel. The interface uses a single bidirectional LVDS[9] signal for both commands and data to reduce the number of wires. MBEE and PBEE exchange alternately 40-bit packets over the same signal line. The protocol is capable of error detection and handling. In the event mode it is always the Module that starts the communication by sending an event packet to the PBEE, which then acknowledges the successful reception of the packet. However, the PBEE is able to change the communication direction in order to set the MBEE into another mode or send configuration data, such as pedestal and gain values.

---

[8]SpaceWire is a communication protocol designed by ESA especially for communication aboard spacecrafts.

[9]Low-Voltage Differential Signaling is a digital signaling standard for the differential transmission of one signal over two lines.

Event Mode

The Event Mode is the corresponding interface mode used to transmit event pack-
ets to the PBEE when the MBEE is in science mode. It is always the MBEE which
starts the communication by sending an event packet. This way the Module does
not need to wait for a time slot to transmit an event. It can send the event to the
PBEE the moment it arrives (if there are no other events waiting in the queue).
Figure 3.5 describes the communication flow for the event mode. The 40-bit event
packet always consists of an 8-bit header and a 32-bit data part:

Header 8 bit	Timestamp 20 bit	Energy 9 bit	Event ID 3 bit

Figure 3.4: Event packet of the MBEE – PBEE interface.

Data Mode

The Data Mode is the interface mode used whenever the PBEE wants to transmit
data to the MBEE. It is used to update configuration values, such as pedestal and
gain values, as well as for the transmission of single commands. The PBEE can
send the command to switch to data mode only as a response to a received packet
from the MBEE. The Data Mode and the procedure of how to change modes are
described in Figure 3.6.

Error Handling and Stability

When transmitting data over a wire it is always possible that a transmission
error occurs, i.e., a bit which has been sent as 1 is read as 0 by the receiver or
vice versa. This can have a variety of causes especially in orbit where charged
particle interactions and changing electromagnetic fields are to be expected. The
transmission protocol has to be able to detect errors and to react properly, i.e.
either to request a retransmission of the failed packet or to mark it as broken.
In each communication, no matter whether the MBEE or the PBEE is the sending
unit, a parity bit is transmitted after the 40-bit event packet is sent. In this way
the receiving unit can check the integrity of the message and detect a single bit-flip.
Two separate bit-flips in the same packet cannot be detected, but the probability
for such an event is very low. When a parity error is detected, the receiving unit
sends a Not-Acknowledged (NACK) packet. The sending unit re-transmits the
same packet until it receives an ACK packet or it reaches a limit of maximum
retries.
Since MBEE and PBEE use the same line to transmit and receive data it is crucial
that both units agree about the direction of the transmission at any time, even if
there are bit-flips during the transmission. The following measures where taken
to ensure communication stability: Each packet has the same size of 40 bit, even

if it is only an ACK packet. When changing the transmission direction for data mode (see Figure 3.6) it is only the logical transmission direction that is changed. The physical transmission direction stays the same: In both modes it is always the MBEE which triggers a new communication packet. In event mode, the MBEE triggers to send an event packet and the PBEE answers with an ACK packet. In Data Mode, the MBEE "pulls" data from the PBEE. It starts a communication pass with an ACK packet related to the previous communication pass, which gives the PBEE the opportunity to answers to this ACK packet with a new data packet.

Data Throughput

Assuming a 5 MHz clock frequency and no errors, the transmission of one 40-bit packet (including the corresponding ACK packet) takes 25 µs. This leads to a data throughput of 40 000 packets per second or 1.6 MBit/s. In science mode, this corresponds to the amount of data that a 20 Crab observation would generate per module.

3.4 Data Handling Unit (DHU)

The Data Handling Unit (DHU) is on top of the hierarchical data processing electronics. It interfaces the six PBEEs in order to collect the science data and to send commands. Since it is out of the main scope of this thesis, it is only briefly described. The main tasks of the Data Handling Unit are:

- Interfacing the PBEEs in order to collect the science data and to send commands and configuration data for the PBEE itself and to be forwarded to single MBEEs.

- Interfacing the spacecraft's On-Board Data Handling system (OBDH) in order to send science and housekeeping data to ground.

- Instrument configuration and control of the on-board mass memory.

- Data compression in order to reduce the amount of data which needs to be sent to ground.
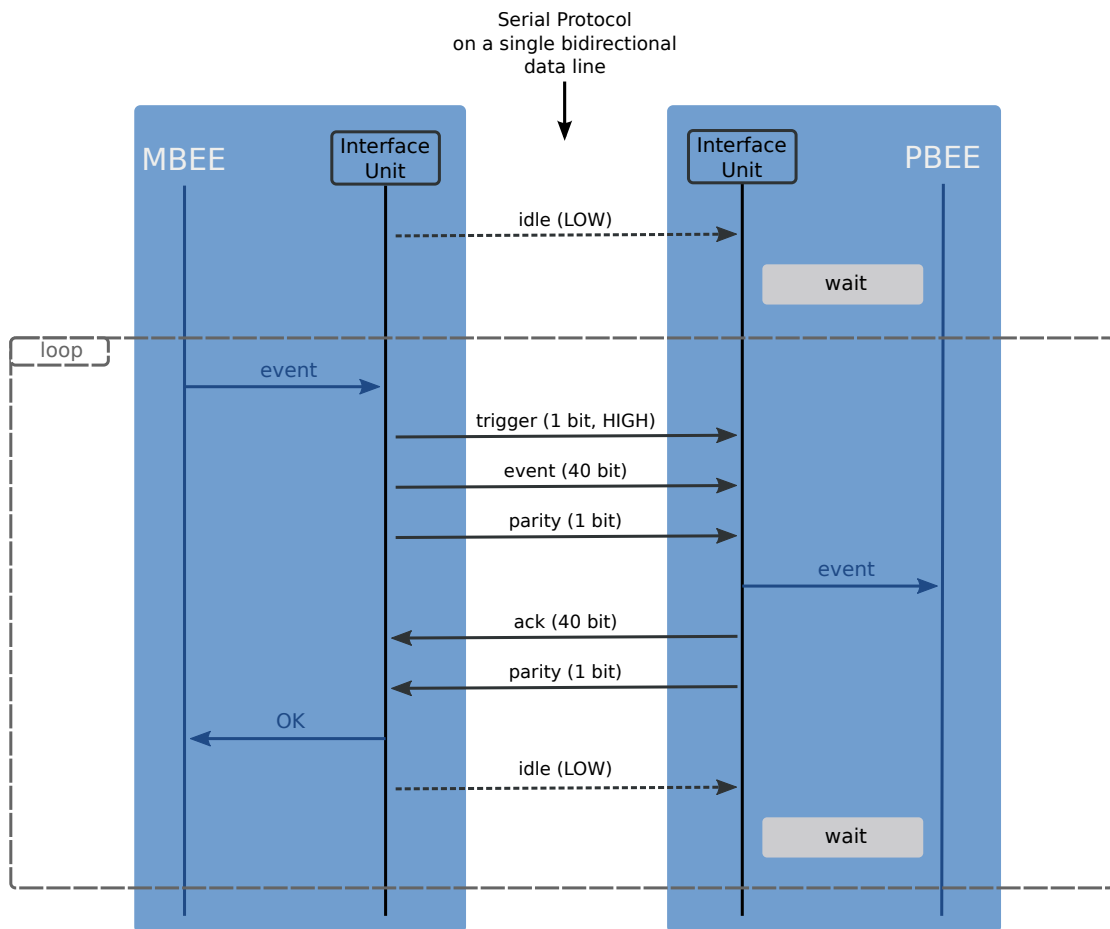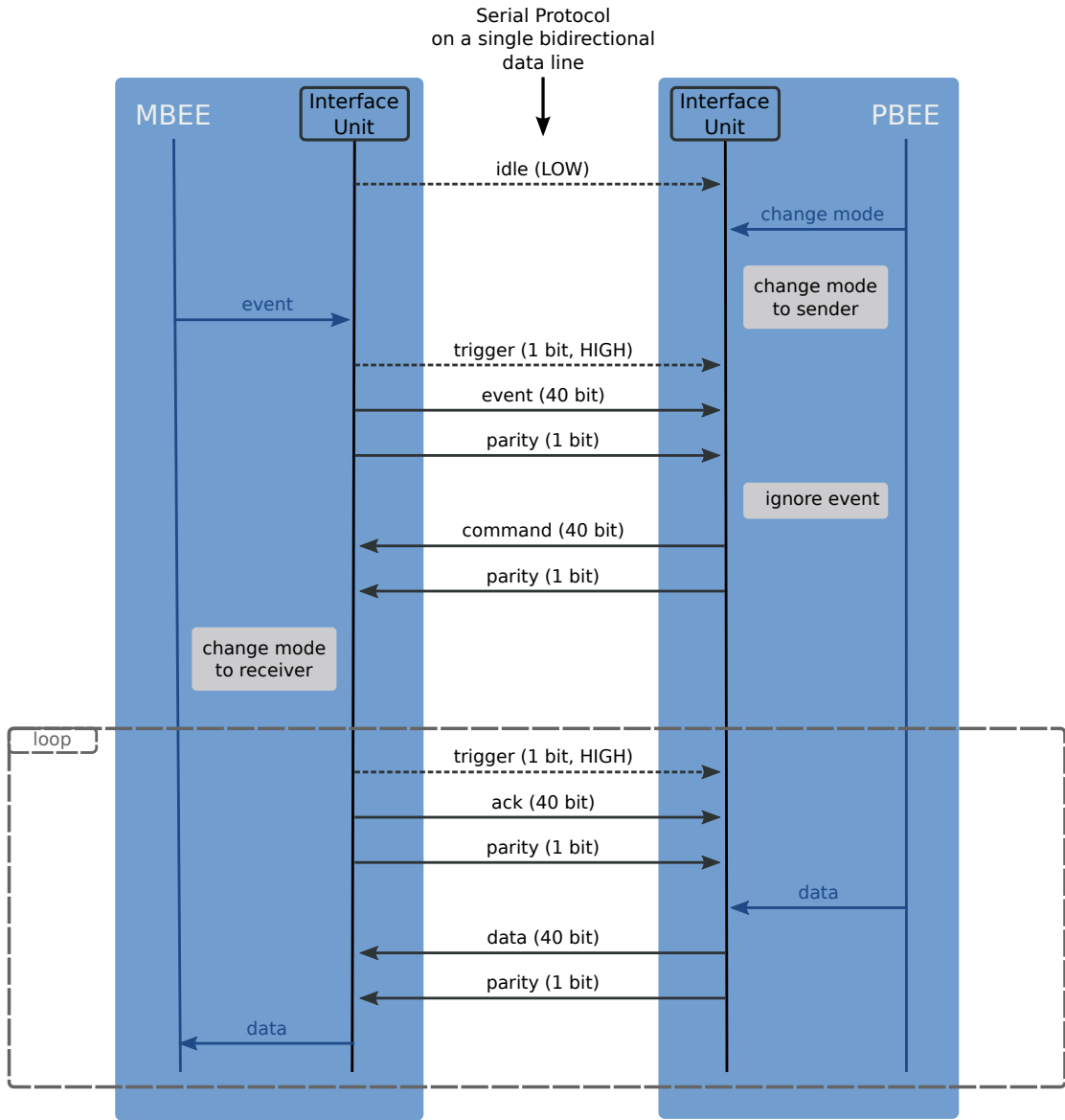
- Collect the housekeeping data from all panels.

Figure 3.5: Communication Flow in Event Mode. The diagram shows from top to bottom the communication flow between MBEE and PBEE. Black arrows describe the status of the data line between MBEE and PBEE. Blue arrows describe how the Interface Unit communicates with the MBEE or PBEE respectively. When there is no event to send, the MBEE pulls the data line to low. Before it starts transmitting a 40-bit event packet (bit by bit) it triggers the PBEE by pulling the line to high for one clock cycle. The PBEE checks the parity bit after the transmission and if correct, it sends a 40-bit packet to acknowledge the reception of the event. After the MBEE has received the ACK packet, it can send a new event packet. Source: based on a figure by H. Wende/IAAT

Figure 3.6: Communication Flow in Data Mode. The diagram shows from top to bottom the communication flow between MBEE and PBEE. Black arrows describe the status of the data line between MBEE and PBEE. Blue arrows describe how the Interface Unit communicates with the MBEE or PBEE respectively. When the interface is idling, the PBEE commands its interface to change the mode to sender. The interface waits for the next event packet to arrive and instead of acknowledging it, it sends the command to change mode to the MBEE. The MBEE changes its mode to receiver and triggers to send a new packet. But instead of sending a new event packet it begins the communication with the acknowledgement of the change mode command. What technically is a response to the acknowledgement of the MBEE, is logically the beginning of a new communication: a new command, or any other data the PBEE wants to send to the MBEE. This can be repeated as long as necessary. Source: based on a figure by H. Wende/IAAT

4 MBEE VHDL Design

This chapter describes the VHDL[1] design of the MBEE, which was one of the main subjects of this thesis. First the general structure of the VHDL design is explained and the pipeline concept is introduced. This is followed by a detailed description of each pipeline unit including its tasks, functionality, internal interfaces, and modes of operation. The external interfaces of the MBEE VHDL design, i.e., the FEE interfaces and the PBEE interface, are also described in detail. Additionally it is explained how the MBEE VHDL code has been simulated to verify its proper functionality. The ASIC simulator, which is required to perform these simulation and was also part of the development for this thesis, is also described. The chapter ends with an analysis of the device usage of the target FPGA and the performance achieved with this VHDL code.

The MBEE is split up into two almost identical boards[2] as shown in Figure 2.11. As the focus of this thesis is on the development of a prototype of these boards, the term MBEE refers here to the prototype if not explicitly stated otherwise.

4.1 Structure

The general structure of the MBEE VHDL design is shown in Figure 4.1. On the top level, there are 16 pipelines, a PBEE Handling Unit and a Global Control Unit. The number of pipelines is parameterized permitting to scale the design for different scenarios. Due to the amount of logic circuits one pipeline occupies within the FPGA, it is merely possible to instantiate 8 pipelines with the current design (see Section 4.7). However, it is reasonable to assume that future improvements of the design will shrink the device usage of one pipeline by at least a factor of two which would allow to instantiate all 16 pipelines in a single FPGA.

4.2 Pipeline

The general idea of using a pipeline is to be able to receive new events while the processing of the old events is not yet completed, which reduces the detector dead time. In general, there is a trade off between data throughput and signal

---

[1]VHDL is a hardware description language used to describe the configuration, and thereby the behavior, of an FPGA (see Section 5.1.1).

[2]In a later revision there will be an interface between the two boards which allows to forward the events of one MBEE–PCB through the other MBEE–PCB to the PBEE.
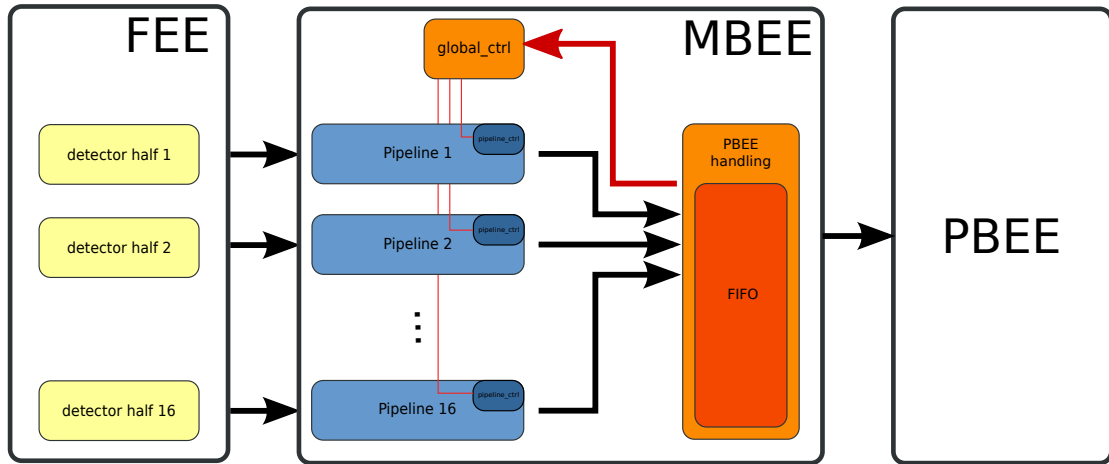
Figure 4.1: Structure of the VHDL Design of the MBEE. There are 16 pipelines, each of them processing the data of one detector half. After the processing in the pipeline an event packet is handed over to the PBEE Handling Unit where it is buffered in a FIFO and passed on to the PBEE using the MBEE–PBEE interface. When the PBEE sets the MBEE into another mode (e.g. changes it from science mode into engineering mode) the PBEE Handling Unit passes this information on to the Global Control Unit, which is connected to each of the 16 pipelines.

latency: both are increased at the same time, when a pipeline gets "stretched out" by splitting up the tasks into several simultaneously working steps, which are undergone by one event sequentially.

4.2.1 Pipeline Design

This section describes the working principle of the data processing pipeline. First, a general overview of the pipeline design is given, then the flow of the anode values through the pipeline is described in detail. The tasks of the pipeline are to validate the trigger map, to perform a pedestal- and common mode subtraction, and to account for the different gain of each anode. After these corrections, it needs to be checked whether the energy value is still in the valid range. Afterwards, an event packet is created, which can be transmitted to the PBEE. The individual tasks have already been discussed in Section 3.2.1 in more detail. Figure 4.2 shows the resulting VHDL design of the pipeline.

Overview of the Pipeline Design

Even though a valid event can only trigger one or two anodes at once, it is not sufficient to read out only these two anodes. In order to subtract the common mode offset it is necessary to process all 16 anode values of the ASIC concerned. If the event is split up between two neighboring anodes controlled by adjacent
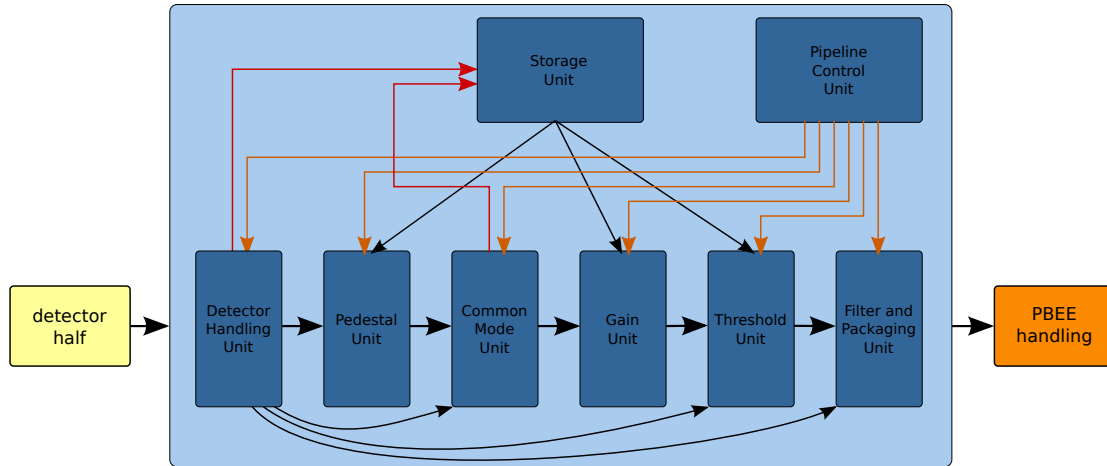
Figure 4.2: Pipeline Design. Bold black arrows indicate the main data stream through the pipeline. Thin black arrows represent supplementary data. Colored arrows represent control lines. The Detector Handling Unit is responsible for the communication with the FEE of one detector half. It decides whether a trigger map is valid and feeds the anode values into the data processing pipeline. It also controls the flow of the anode values through the pipeline. The Pipeline Control Unit sets the operational mode (active, bypass, engineering, . . .) of all other units. The Storage Unit provides stored values, such as pedestal or gain values, in synchronization with the flow of the anode values through the pipeline.

ASICs (see Figure 4.3) it is required to process all 32 anode values of the two involved ASICs. Since the hardware must be prepared for the "worst processing case" the pipeline is designed to handle two sets of 16 anodes each, for one event. Therefore, the interface between the Front End Electronics and the MBEE is capable of reading out two adjacent ASICs in parallel in order to minimize the detector dead time.

As it has been found to be most efficient, the pipeline is processing the events on a one-anode basis: Merely one anode value is handed over from one unit to the next within a clock cycle. This concept keeps the units and the internal interfaces small and simple. To avoid overhead, no meta data is passed along with the anode values. This means that the data stream through the pipeline does not contain any information about which ASICs or which anodes have been involved in the currently processed event. This information is, as far as it is necessary for the processing, directly provided by the Detector Handling Unit.

Flow of the Anode Values through the Pipeline

This section describes the flow of the anode values through the pipeline, as illustrated in Figure 4.2. After the Detector Handling Unit has received the last anode values, it starts to pass the anode values to the Pedestal Unit. Before the
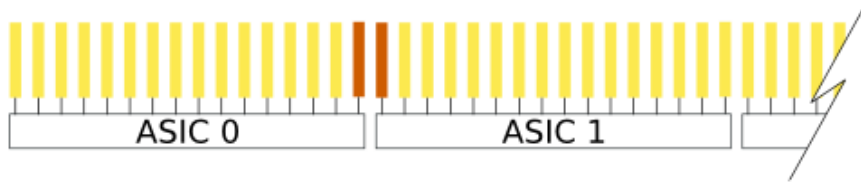
Figure 4.3: A split event between two ASICs. Each ASIC controls 16 anodes (yellow). All 32 anodes of ASIC 0 and ASIC 1 need to be read out to be able to determine the common mode offset of both ASICs individually. The FEE–MBEE interface and the Detector Handling Unit of each pipeline are designed to be able to read out two ASICs simultaneously to reduce the detector dead time.

beginning of the transmission, the Detector Handling Unit provides the Storage Unit with the number of the triggered ASIC, which allows the Storage Unit to stream the respective pedestal values to the Pedestal Unit.

The Pedestal Unit passes the corrected anode values further to the Common Mode Unit. In order to calculate and subtract the common mode, the Common Mode Unit must process the full set of all 16 anodes. Since the common mode processing cannot start before the 16th anode value has been received, the calculation takes the time of additional 17 clock cycles. The Common Mode Unit triggers the Storage Unit to provide the gain values to the Gain Unit before it starts transmitting the corrected anode values. The Common Mode Unit subtracts the common mode offset from one anode value at a time and transmits the results during the next subsequent 16 clock cycles. The Common Mode Unit cannot receive new anode values until it has transmitted its last corrected anode value. The Detector Handling Unit delays the transmission of further anode values until this moment before it starts to feed the Pedestal Unit with the second set of 16 anode values. The Gain Unit applies a gain correction to the anode values and transfers them to the Threshold Unit, one clock cycle after receiving them. The Threshold Unit is provided with the anode number of the triggered anode from the Detector Handling Unit. It counts the anodes, which it reads in, in order to determine the triggered anode. The Threshold Unit does not store the anode values of the non-triggered anodes, nor does it pass them on any further. Only the up to two triggered anodes are selected for the energy reconstruction and threshold checks. The reconstructed energy and the result of the threshold checks are passed on to the Filter and Packaging Unit, where this information is encapsulated into event packets, which will be passed on to the PBEE Handling Unit in order to be transmitted to the PBEE. The Pipeline Timing is illustrated in Table 4.1.

Timing Considerations

The pipeline must match the transmission speed of the interface between the Front End Electronics and the Module Back End Electronics in order to avoid an increase

Table 4.1: Pipeline Timing. The timing data is obtained by a simulation of the current design. After all anode values are received via the FEE–MBEE interface it takes $469 - 446 = 23$ clock cycles until the MBEE is ready to receive a new event.

	Clock	Comment
Trigger occurs	0	
Trigger map received	49	
Anode data received	446	
Start feeding pipeline	448	processing begins
Pedestal Unit processes 1. anode	449	
Pedestal Unit processed 16. anode	465	
Common mode read (1-16) complete	466	
Reset sent	469	ready for a new event
common mode calculation done	483	
Common Mode Unit passed on 16. anode	499	
Pedestal Unit processes 17. anode	501	
Pedestal Unit processed 32. anode	518	
Common Mode Unit passed on 32. anode	551	
Threshold Unit read last anode (32)	553	
Filter/Packaging Unit done	555	processing completed

of the detector dead time. Even though the interface clock will probably be slower than the MBEE system clock, the following estimation is based on the assumption that the interface clock between FEE and MBEE is the same as the MBEE system clock. This leads to a conservative estimate of the available processing time for the pipeline between two events: There are at least 206 clock cycles between the arrival of two consecutive events according to Table 4.2. This is sufficient since the current pipeline design is capable of processing a new event every 70 clock cycles.

Table 4.2: Estimation of the minimum time between two events arriving at the pipeline. These values are not recommended for estimating the detector dead time due to the FEE–MBEE interface, because the actual interface might be significantly slower as is the implemented interface.

Event	Clock Cycles	Comment
request trigger map	7	3-bit addr + 4-bit cmd
transmit trigger map	16	16-bit trigger map
start conversion command	7	3-bit addr + 4-bit cmd
transmit anode values	176	16 x 11-bit
total	206	

4.2.2 Unit-Unit interface

Since new data is not available with every system clock cycle, the input of each unit has an `is_data_flag`, indicating when data is actually available. Each unit displays the result at its output for exactly one clock cycle. Therefore, if a certain unit has an active `is_data_flag` for 16 subsequent clock cycles, 16 different results have been transmitted. This demands, however, that the next unit has to be ready to read the result immediately. As already described, the Detector Handling Unit controls the flow of the anode values through the pipeline and ensures that new anode values are only transmitted into the pipeline when the units are ready to receive new data.

This concept only applies to the interfaces between the subsequent processing pipeline units, i.e. from the Detector Handling to the Filter and Packaging Unit. It does not apply to the interfaces between pipeline units and the Storage Unit or the Pipeline Control Unit, neither does it apply to the interface between the Filter and Packaging Unit at the end of the pipeline and the PBEE Handling Unit. The Filter and Packaging Unit is the only unit that displays its output longer than one clock cycle with an active `is_data_flag`, which is necessary to serialize the data from all pipelines within the PBEE Handling Unit with a minimal effort (see Section 4.4).

4.3 Pipeline Units

In this section, the pipeline units are described in detail. A short introduction explains the purpose of the respective unit within the pipeline. All inputs and outputs of each unit are listed in tables and the functionality as well as the supported operational modes are described in detail.

4.3.1 Detector Handling Unit (DH)

The purpose of the Detector Handling Unit is to interface a detector half, and to control the the flow of the anode values inside the pipeline. The implementation of the interface between FEE and MBEE is described in detail in Section 4.5.1. The interaction of the Detector Handling Unit with the pipeline units has already been described in Section 4.2.1.

DH–I/Os

Event data communication from the ASICs to the Detector Handling Unit is performed by exclusive single line interfaces[3], whereas commands from the Detector Handling Unit to the ASICs are transmitted on a single line bus-like structure,

---

[3]This deviates from the FEE interface description in Section 3.2.3, because the interface has been already implemented, when the number of data lines was reduced. The implemented FEE–MBEE interface is described in detail in Section 4.5.1.

Table 4.3: Detector Handling Unit I/Os

Name	I/O	Bits	Sign	Scaling	Comment
clk_in	in	1	-	-	system clock
ctrl_in	in	2	-	-	from pipeline_ctrl
data_in	in	7	-	-	1 line per ASIC
trigger_in	in	1	-	-	
asic_cmd_out	out	1	-	-	
to_pedestal.anode	out	11	u	1	
to_pedestal.is_data_flag	out	1	-	-	
to_common_mode.trigger_count	out	2	u	1	
to_threshold.trigger_count	out	2	u	1	
to_threshold.triggered_anode_no	out	5	u	1	
to_threshold.reset	out	1	-	-	
to_storage.asic_no_ped	out	5	u	1	
to_storage.asic_no_gain	out	5	u	1	
to_storage.pedestal_trigger	out	1	-	-	

which is connected to all ASICs simultaneously and is utilizing a protocol based addressing scheme. The I/Os of the Detector Handling Unit are described in Table 4.3.

DH–Functionality

The Detector Handling Unit contains two (independent) finite state machines (FSM): One called `state` which controls the actual detector handling including the communication with the ASICs. The other one is called `feed_state` and feeds the anode values into the pipeline in the way described in Section 4.2.1 under "Flow of the Anode Values". The feed_state FSM gets triggered by the `newDataAvail` signal from the `state` FSM.

The trigger map evaluation (see Section 3.2.3) is a two-step process: While the trigger map is received from all ASICs in parallel, the Detector Handling Unit checks if there are at most two triggered anodes per ASIC and, if there are two, whether they are adjacent. If there are no invalid patterns within an ASIC, the Detector Handling Unit checks in a second step if there are no more than two triggered ASICs, and in case of two trigger ASICs whether the joined trigger map of these two ASICs is still valid. When the transmission of all anode values from the triggered ASICs is completed, the `state` FSM triggers the `feed_state` FSM to start feeding the anode values into the pipeline. At this point, the reset command is sent to the ASICs, which ends the detector dead time. The time that is required to send the reset command and to read and validate the trigger map of a new event is used by the Detector Handling Unit to feed all anode values into the pipeline in order to be ready to receive the new anode values. In fact it is sufficient if the

Detector Handling Unit has fed the first 17 anodes into the pipeline, when it starts reading in new values: It reads in the first anode from each ASIC in parallel. The first anode from the second ASIC is the 17th anode to be fed into the pipeline. The anode values can be fed into the pipeline faster with the parallel bus than it is possible to read in new anode values with the serial interface. Therefore the newly read in anode values will not override the yet to be fed anode values from the old event if the first 17 anodes have already been fed.

DH–Modes

The Detector Handling Unit currently only supports the science operation mode. The engineering mode however will not require any changes in the Detector Handling Unit since all information is already passed on in science mode. Nevertheless, it has to be modified for configuration mode to be able to send configuration data, such as new trigger thresholds, to the FEE–ASICs.

4.3.2 Pedestal Unit (PU)

The task of the Pedestal Unit is to subtract from an anode value its respective stored pedestal value. The pedestal unit expects both values (anode and pedestal) as inputs and gives the result of the subtraction as its output.

PU–I/Os

Table 4.4: Pedestal Unit I/Os

Name	I/O	Bits	Sign	Scaling	Comment
clk_in	in	1	-	-	system clock input
ctrl_in	in	2	-	-	input from pipeline_ctrl
data_in.anode	in	11	unsigned	1	
data_in.is_data_flag	in	1	-	-	
storage_in	in	13	signed	2^{-1}	pedestal value
data_out.anode	out	13	signed	2^{-1}	result
data_out.is_data_flag	out	1	-	-	

The 11-bit precision of the A/D converter directly translates into the bit-width of the input anode value. The stored pedestal value has a precision of 12-bit in order to maintain accuracy.[4] The result needs to be a signed number to account

---

[4]The pedestal values are determined during calibration as the mean of non-triggered anodes. To avoid loss of information the mean value needs to be stored with higher precision than the values it is calculated from

for the possibility of negative values after the pedestal subtraction.[5] Hence, the bit-width is increased to 13 bit.

PU–Functionality and Latency

The anode value is expanded to a signed 13-bit value with one position after the radix point and the subtraction is executed as a 13-bit signed operation. The result is available at the output one clock cycle after the `data_in.is_data_flag` was set.

PU–Modes

The operational mode of the Pedestal Unit is controlled by the `ctrl_in` port. The supported modes are:

00 Active. The unit performs standard operations as described in this section.

01|10 Bypass. The anode value will be expanded to a 13-bit signed signal, which will be at the output one clock cycle after the `data_in.is_data_flag` has been set. No pedestal subtraction is performed.

11 Off. The outputs will be zero at all times.

4.3.3 Common Mode Unit (CMU)

The task of the Common Mode Unit is to subtract the common mode offset from all anode values in the data stream. The common mode is calculated as the median[6] of all non-triggered anodes of one ASIC. The Common Mode Unit accumulates 16 anode values, calculates the median and outputs the resulting anode values in 16 subsequent clock cycles. The I/Os of the Common Mode Unit are described in Table 4.5.

Table 4.5: Common Unit I/Os

Name	I/O	Bits	Sign	Scaling	Comment
clk_in	in	1	-	-	system clock input
ctrl_in	in	2	-	-	input from pipeline_ctrl
data_in.anode	in	13	signed	2^{-1}	
data_in.is_data_flag	in	1	-	-	
from_dh.trigger_count	in	2	unsigned	1	no. of triggered anodes
to_storage.gain_trigger	out	1	-	-	
data_out.anode	out	13	signed	2^{-1}	result
data_out.is_data_flag	out	1	-	-	

---

[5]Statistically, half of the non-triggered anode values are expected to be negative after the pedestal subtraction

[6]It is easier to calculate the median than the mean with an FPGA.

CMU–Functionality and Latency

The common mode is calculated using the Odd-Even-Transportation-Sort (OETS) algorithm (Leighton, 1991). It is utilizing $n/2$ comparators to sort n values in n clock cycles. An additional clock cycle is necessary to determine the median value, which is based on the sorted list of anode values and the number of triggered anodes[7]. The working principle of this algorithm is explained in Figure 4.4. After the 16th anode is read in, it takes 17 clock cycles until the Common Mode Unit has determined the common mode offset and is ready to transmit its results.
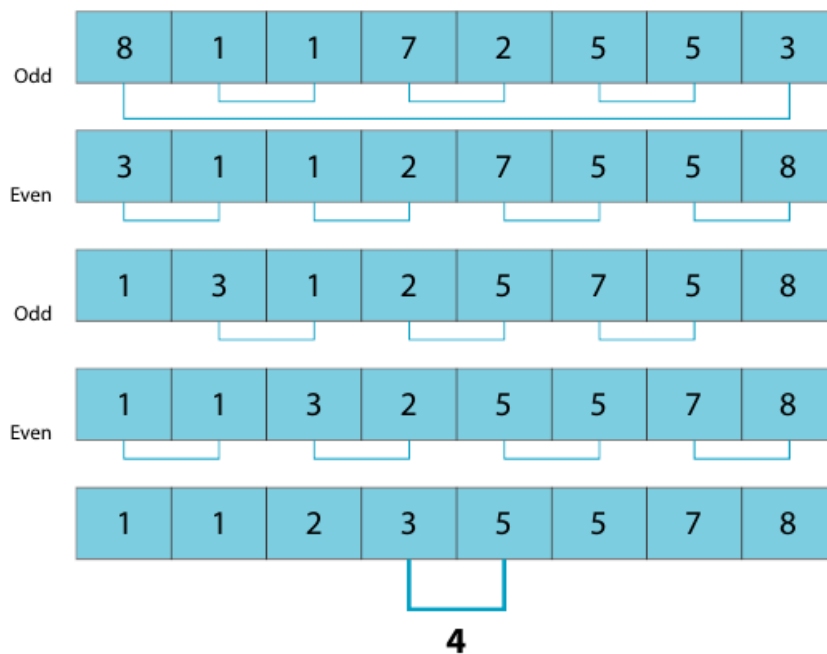
Figure 4.4: Working principle of the Odd-Even-Transportation-Sort (OETS) algorithm. This algorithm works with two repetitive steps: In the first step odd pairs $(1/2, 3/4, \ldots)$ are compared and, if necessary, switched in a way that the smaller value of each pair is at the position with the smaller index. The next step proceeds the same way with even pairs $(0/1, 2/3, \ldots)$. (Leighton, 1991) showed that no more than n steps are necessary to sort n numbers with this algorithm. Source: Christmann, 2011

---

[7]In a hardware implementation it is easier to sort a list of constant size (16 anode values) than a list of variable size (15 or 14 anode values, depending on whether one or two anodes have triggered). The number of triggered anodes is considered when selecting the median from the sorted list.

CMU–Modes

The mode is controlled by the `ctrl_in` port. The supported modes are:

00 Active. The unit behaves as described in this section.

01 Bypass (delayed). The unit outputs the anode values unchanged but with the same latency as described in this section.

10 Bypass (undelayed). The unit outputs the anode values unchanged with no latency.

11 Off. The outputs will be zero at all times.

4.3.4 Gain Unit (GU)

Each anode has a slightly different gain due to tolerances in the manufacturing process of the SDD and the readout ASICs. The task of the Gain Unit is to correct for those differences by multiplying each anode value by its stored respective gain factor.

GU–I/Os

Table 4.6: Gain Unit I/Os

Name	I/O	Bits	Sign	Scaling	Comment
clk_in	in	1	-	-	system clock input
ctrl_in	in	2	-	-	input from pipeline_ctrl
data_in.anode	in	13	signed	2^{-1}	
data_in.is_data_flag	in	1	-	-	
storage_in	in	7	unsigned	2^{-4}	gain value
data_out.anode	out	17	signed	2^{-2}	result
data_out.is_data_flag	out	1	-	-	

The resolution of the stored gain correction value is 7 bit and represents a binary number with 3 bits before and 4 bits after the radix point. This allows to correct for gain differences up to a factor of $2^3 - 1 = 7$ with an accuracy of $2^{-4} = 0.0625$ in the factor. These values can be easily adjusted, when the actual necessary factor of precision will be determined later on in the project.

GU–Functionality and Latency

The gain correction is executed on an anode by anode basis. The 13-bit anode value is multiplied with the stored 7-bit gain correction value resulting in a 20-bit

value with a scaling of 2^{-5}. For the output the last 3 bits are truncated resulting in a 17-bit value with a scaling of 2^{-2}. The result is available at the output of the Gain Unit one clock cycle after the `data_in.is_data_flag` was set.

GU–Modes

The operation mode of the Gain Unit is controlled by the `ctrl_in` port. The supported modes are:

00 Active. The unit behaves as described in this section.

01|10 Bypass. The anode value will be expanded to a 17-bit signed number, which will be at the output one clock cycle after the `data_in.is_data_flag` has been set. No gain correction is performed.

11 Off. The outputs will be zero at all times.

4.3.5 Threshold Unit (TU)

The Threshold Unit checks on a per anode basis whether a lower threshold is exceeded, performs an energy reconstruction (summation of the two triggered anode values), and checks if the reconstructed energy is below the upper limit for a valid event. The result of these tests is passed on as a flag to the Filter and Packaging Unit. The I/Os of the Threshold Unit are described in Table 4.7.

Table 4.7: Threshold Unit I/Os

Name	I/O	Bits	Sign	Scaling	Comment
clk_in	in	1	-	-	system clock input
ctrl_in	in	2	-	-	input from pipeline_ctrl
data_in.anode	in	17	s	2^{-2}	
data_in.is_data_flag	in	1	-	-	
storage_in.lower_threshold	in	16	u	2^{-2}	per anode
storage_in.upper_threshold	in	17	u	2^{-2}	for reconstructed energy
from_dh.trigger_count	in	2	u	1	no. of triggered anodes
from_dh.triggered_anode_no	in	5	u	1	no. of the (first) triggered anode
from_dh.reset	in	1	-	-	
data_out.anode	out	17	s	2^{-2}	
data_out.is_data_flag	out	1	-	-	
data_out.energy	out	18	s	2^{-2}	
data_out.lower_limit_flag	out	1	-	-	0: ok, 1: not ok
data_out.upper_limit_flag	out	1	-	-	0: ok, 1: not ok
data_out.event_id	out	3	-	-	000: no event 001: single, 010 double

TU–Functionality and Latency

The Detector Handling Unit supplies the Threshold Unit with information about the number of triggered anodes (i.e., one or two triggered anodes). It also provides the anode address of the (first) triggered anode counting from 0 (first anode of the first ASIC) to 31 (16$^{\text{th}}$ anode of the second ASIC). Since the anode address is not transmitted along with the anode values, the Threshold Unit has to count[8] up the incoming anode values in order to determine which anode values are the triggered ones.

After the corrections in the earlier units of the pipeline have been applied, an anode value which was initially high enough to trigger the analog threshold of an ASIC, might now be reduced in energy and no longer be high enough to pass the lower threshold limit of the Threshold Unit. If the anode value of a triggered anode overcomes the lower threshold limit, its value counts towards the reconstructed energy. Only triggered anodes that overcome the lower limit affect the multiplicity of the event. Therefore, in some cases, an event which was initially classified as a two-anodes event by the Detector Handling Unit can end up as an one-anode event or even a non-valid event if only one or none anode passes the lower threshold of the Threshold Unit.

One clock cycle after the last anode value has been received, it is checked whether the reconstructed energy is below the upper threshold. During the same clock cycle the results of the threshold checks, the reconstructed energy, and the event ID are passed on to the Filter Packaging Unit.

TU–Modes

The operational mode of the Threshold Unit is controlled by its `ctrl_in` port. Since the Threshold Unit only adds information (flags, energy, event ID) but does not modify any data, there is no need for a bypass mode. The supported modes of the Threshold Unit are:

00 Active. The unit behaves as described in this section.

01|10 Engineering. The unit behaves as described in this section, but in addition all anode values are passed on to the Filter Packaging Unit one clock cycle after it was received by the Threshold Unit. In this mode the Filter Packaging Unit has to use a counter: First the 32 anode values are passed on. Then the regular information about energy, flags and event ID is passed on.

11 Off. The outputs will be zero at all times.

---

[8]A rising edge of the reset signal resets this counter (as well as the energy and the even id) before a new event is fed into the pipeline to prevent the counter to get out of synchronization for ever by a single bit flip of the `is_data_flag`.

4.3.6 Filter and Packaging Unit (FPU)

In science mode, the Filter and Packaging Unit filters for events in the valid energy range only and creates an event packet to be sent to the Panel Back End Electronics (PBEE). The Filter and Packaging unit is the first unit (behind the Detector Handling Unit) where processed events can be dropped. The concept, which utilizes flags and filters instead of dropping anode values inside the processing pipeline, is preferred in preparation for the engineering mode: Different requests about the amount of details to be passed on to the PBEE can be realized by different filter configurations inside the Filter and Packaging Unit.

FPU–I/Os

Table 4.8: Filter and Packaging Unit I/Os

Name	I/O	Bits	Sign	Scaling	Comment
clk_in	in	1	-	-	system clock inp
ctrl_in	in	2	-	-	from pipeline_ctrl
data_in.anode	in	17	s	2^{-2}	
data_in.is_data_flag	in	1	-	-	
data_in.energy	in	18	s	2^{-2}	
data_in.lower_limit_flag	in	1	-	-	0: ok, 1: not ok
data_in.upper_limit_flag	in	1	-	-	0: ok, 1: not ok
data_in.event_id	in	3	-	-	
to_PBEE_handling.energy	out	9	u	1	re-binned energy
to_PBEE_handling.timetag	out	20	u	1	
to_PBEE_handling.event_id	out	3	-	-	
to_PBEE_handling.anode	out	17	s	2^{-2}	simulation only
to_PBEE_handling.energy_full	out	18	s	2^{-2}	simulation only
to_PBEE_handling.lower_limit_flag	out	1	-	-	simulation only
to_PBEE_handling.upper_limit_flag	out	1	-	-	simulation only
to_PBEE_handling.is_data_flag	out	1	-	-	

The signals in Table 4.8 marked as "simulation only" are used to test the pipeline on a simulation testbench. An ASIC simulator can feed the testbench with event data, and the results can be written into a file by a special testing unit which replaces the PBEE Handling Unit. Those signals will not be needed for hardware verification with the not yet implemented engineering mode. If requested by the PBEE, it is the task of the Filter and Packaging Unit to form regular "event packets" of 32 bit for all anode values.

FPU–Functionality and Latency

In science mode, the event packet is handed over to the PBEE Handling Unit one clock cycle after the data was read in from the Threshold Unit. In contrast to all other units where the output is available only for one clock cycle, the Filter and Packaging Unit holds its output for 16 clock cycles. This is required in order to buffer the data in a FIFO inside the PBEE Handling Unit and due to the fact that there are 16 pipelines interfaced in parallel by one PBEE Handling Unit. For more information on the PBEE Handling Unit see Section 4.4.

FPU–Modes

The operational mode of the Filter and Packaging Unit is controlled by the `ctrl_in` port. The supported modes are:

00 Active. The unit operates as described in this section.

01|10 Engineering. In this mode different filters can be applied. Information on a certain set of anodes (including only one or all) can be requested. The Engineering mode of this unit is yet to be implemented.

11 Off. The outputs will be zero at all times.

4.4 PBEE Handling Unit (PHU)

The PBEE Handling Unit is the interface between the MBEE-pipelines and the PBEE. In the worst case 16 packets (one from each pipeline) can arrive simultaneously at the PBEE Handling Unit, whereas only one packet can be transmitted to the PBEE at once. With the current MBEE–PBEE interface specifications, one packet can be transfered every 25 µs, whereas one pipeline can process an event in 1.75 µs. For these reasons, the PBEE Handling Unit needs to buffer the incoming event packets, which is discussed in more detail in Section 4.8.

PHU–I/Os

The I/Os of the PBEE Handling Unit are described in Table 4.9. The PBEE Handling Unit is the only unit without a `ctrl_in` signal input, which means it is not controlled by the Global Control Unit of the MBEE (cf. Figure 4.1); its operational modes are set via commands from the PBEE. The `inp(<>)` port is a signal input to the PBEE Handling Unit, which provides as many inputs as there are pipelines implemented inside the MBEE. The `inp(<>)` port is organized as a VHDL array type.

Table 4.9: PBEE Handling Unit I/Os

Name	I/O	Bits	Sign	Scaling	Comment
clk_in	in	1	-	-	system clock inp
clk_interface	in	1	-	-	interface clock inp
inp(<>).energy	in	9	u	1	re-binned energy
inp(<>).timetag	in	20	u	1	
inp(<>).event_id	in	3	-	-	
inp(<>).anode	in	17	s	2^{-2}	simulation only
inp(<>).energy_full	in	18	s	2^{-2}	simulation only
inp(<>).lower_limit_flag	in	1	-	-	simulation only
inp(<>).upper_limit_flag	in	1	-	-	simulation only
inp(<>).is_data_flag	in	1	-	-	
to_PBEE	inout	1	-	-	bidirectional interface

PHU–Functionality

The PBEE Handling Unit interfaces 16 pipelines simultaneously. In order to transmit event packets via the MBEE–PBEE interface, these data need to be serialized first, before they can be transmitted to the PBEE. Even one single pipeline can process events faster than they can be transmitted (see Section 4.8). A buffer is needed, which will delay the amount of data. Therefore the Filter and Packaging Unit holds its output for 16 clock cycles. This enables the PBEE Handling Unit to circle through all 16 pipelines and to write one event packet per clock cycle into the FIFO buffer without missing any incoming packets. The PBEE Handling Unit could copy all inputs simultaneously into internal registers rendering it unnecessary for the Filter and Packaging Unit to hold its output for more than one clock cycle. However, such a design approach would be less efficient in terms of the required device usage: The current approach requires only slightly more control logic to hold the outputs for 16 clock cycles (instead of one clock cycle) in already existing (output) registers, whereas the "internal registers" approach would require additional registers in order to store a copy of all 16 inputs registers.

The FIFO buffer of the PBEE Handling Unit has a depth of 128 steps, which is sufficient to achieve the design goal peak intensity of 30 Crab. Moreover, there is still a fair amount of hardware resources left in the FPGA in order to increase the depth of the FIFO in the future. The interface of the PBEE Handling Unit to the PBEE is described in Section 3.3.1.

PHU–Modes

The operating mode of the PBEE Handling Unit is directly controlled via commands from the PBEE sent over the MBEE–PBEE interface. The PBEE Handling

Unit sets the mode of the Global Control Unit of the MBEE, which again set the modes of each Pipeline Control Unit within the MBEE. The Pipeline Control Units distribute the mode to each individual unit inside their respective pipelines. The following modes have been described in more detail in Section 3.2.2:

- Science Mode. All event processing units are active and everything works as described in this chapter.

- Engineering Mode. The Engineering Mode allows the PBEE to request more information about the events than what is normally passed on in Science Mode. The Engineering Mode is not implemented for the time being but the pipeline design is already prepared for the Engineering Mode.

- Configuration Mode. The Configuration Mode is partially implemented: It allows to set and update pedestal, gain, and threshold values for the pipelines. It does not support reconfiguration of the FEE–ASICs so far.

4.5 Interfaces

This section describes the MBEE interfaces to the FEE and the PBEE.

4.5.1 MBEE–FEE Interface

The interface between the MBEE and the FEE is used to read out event data from the detector and to reconfigure the FEE–ASICs. One MBEE controls eight detectors and therefore has eight MBEE–FEE interfaces. The current interface design is described in Section 3.2.3. However, the latest design changes have not been implemented in VHDL yet. Since the implementation of the interface, the number of data lines has been reduces from seven lines, one per ASIC, to two lines (even and odd). This reduces the amount of necessary wires significantly, but it also increases the read out time of the trigger map and therefore increases the dead time of the detector. In contrast, the use of a dedicated reset line instead of a reset command, which is send over the serial command line, decreases the dead time. Which of these effects will finally prevail depends on the actual protocol that will be used. Also new and not implement in the current version of the interface are the CAL and HOLD lines, as they are described in Section 3.2.3.
The implemented interface which is described in this section is based on preliminary discussions with the ASIC developers at IRAP, Toulouse. However, there is no protocol between the FEE and the MBEE defined yet. The goal of the implementation in this thesis is not to propose a protocol, but rather to setup an MBEE testing environment, and to estimate the device usage of the FEE–MBEE interface. The current protocol is a reasonable approach to the extent that it is a serial protocol with one shared command line for all ASICs and several serial lines for the transmission from the ASICs to the MBEE. There is no transmission error

detection or correction, as it is not designed to be stable against single bit-flip errors, for the time being.

Commands to the ASICs

A command packet that is sent from the Detector Handling Unit to the ASICs has a fixed size of 21 bits:

Start 101	Address 3 bit	Command 4 bit	Data 11 bit

Figure 4.5: Command Packet MBEE – FEE.

The first three bits of the packet have always the pattern `101` to inform the ASICs about an incoming command. The next three bits address the ASIC: `001` for the first ASIC to `111` for the seventh ASIC with `000` addressing all seven ASICs at once. Table 4.10 describes the implemented commands. The 11-bit data can be used with commands to reconfigure the ASIC, e.g. to send new trigger thresholds to the ASICs. This is not yet implemented in the design.

Table 4.10: Commands in the FEE–MBEE interface protocol. Only science mode commands are already implemented. Reserved commands will be used for configuration mode implementation.

Value	Command
0001	Send trigger map
0010	Start A/D conversion
0011	Reset
others	Reserved

Data from the ASICs

Packets send from an ASIC to the Detector Handling Unit have a fixed size of 22-bit:

Start 101	ID 3 bit	DATA 16 bit

Figure 4.6: Data Packet FEE – MBEE.

The first three bits to alert the MBEE about an incoming packet have the pattern `101` as well. The ID is either `001` to indicate that the next 16 bits belong to the trigger map or `010` to indicate the transmission of anode data. When anode

data is transmitted, the first eleven data bits contain the anode value followed by five zero bits to fill up the packet size. There is no field indicating to which anode number an anode value belongs. The Detector Handling Unit expects the anode values to be transmitted in the correct order starting with anode 0 counting upwards to anode 15.

4.5.2 MBEE–PBEE Interface

The interface between MBEE and PBEE is used to transmit event packets from the MBEE to the PBEE during science mode. In configuration mode it is used to send new storage values, such as pedestal or gain values, to the MBEE. The MBEE–PBEE Interface is implemented as described in Section 3.3.1. It is used in the simulation testbench as well as in the hardware setup, both described below. As opposed to the FEE interface, the MBEE–PBEE Interface, currently developed at IAAT, is meant as a baseline for the actual interface.

4.6 Simulation

VHDL designs are generally simulated before they are implemented in hardware. For this case a testbench is required, which provides the necessary inputs for the unit under test and a way to analyze the output. Therefore the MBEE testbench requires an ASIC simulator, which provides an input for the MBEE, and a PBEE simulator (developed at IAAT), that sends configuration data to the MBEE and reads out the processed events. The testbench is parameterized to handle an MBEE with 1 to 16 pipelines. For full verification, 16 pipelines should be used. For analyzing a certain bug in the process it can be useful to simplify the system to fewer pipelines to decrease the time needed for a single simulation run.

4.6.1 ASIC Simulator

The ASIC simulator provides the functionality of an ASIC necessary to feed the MBEE with events. The ASIC simulator reads the events out of a disk file with the input file format described in Table 4.11. The `wait before` value describes how many clock cycles the ASIC simulator should wait before it raises the trigger line, in order to transfer the event described in the current line of the file. The 112-bit `trigger map` describes the trigger map of a whole detector half. Each simulated ASIC transmits its respective part from the trigger map upon request. The same applies to the `anode value`s.

The ASIC simulator consists of an ASIC Unit, which simulates the behavior of a single ASIC, and a Detector Half Unit, which instantiates seven ASICs with their respective data out line, as well as the logic OR of all seven trigger lines. All ASICs of one detector half read in their data from the same file.

Table 4.11: Input File Format for the ASIC Simulator. Each bit is represented by an ASCII 0 or 1. There is one space between two values (also between two anode values). To test the creation of dummy events by the MBEE, the `wait before` value can be set very large.

Name	Bit width	Comment
wait before	29	
trigger map	112	
anode value	11	112 times

4.7 Device Usage

The device usage is a critical parameter when configuring an FPGA with a VHDL design. It describes the amount of logical cells of the targeted FPGA device that will be utilized by the VHDL design after configuration, and provides a parameter that determines whether the VHDL design actually "fits into" the FPGA. The target device for the LOFT prototype design is a Microsemi RTAX2000 FPGA. The device has two different kind of cells (see Section 5.1.1): combinatorial cells and sequential cells.

The design described in this chapter (later referred to as Serial Anodes Approach) allows to instantiate 8 pipelines, including the FEE interfaces together with the full PBEE interface in an RTAX2000 FPGA with a device usage of 91 % of combinational cells and 73 % of sequential cells. In order to be able to instantiate all 16 pipelines in the final design, it is necessary to decrease the device usage of a single pipeline by a factor of two, which is only a small factor, when compared to the device usage of the First Approach.

4.7.1 First Approach

The first design approach concentrated on the functional design of individual pipeline units by implementing a single processing pipeline. In this first design individual units passed on all 16 anode values in parallel, together with meta information about the ASIC number, the triggered anodes and the timestamp. The Pedestal- or Gain Units, for instance, have requested the stored values directly from the Storage Unit so that precise timing was not a complex issue. This design was easy to understand, good to debug and the code was well readable. However, the device usage was enormous. After a lot of effort put into optimization, which shrunk the device usage by about a factor of two, a device usage of 38 % of combinational cells and 15 % of sequential cells was achieved. Note, that these numbers are only for one pipeline without a Detector Handling Unit, an FEE interface or a PBEE Handling Unit with the PBEE interface. In order to fit the design including 16 pipelines into the RTAX2000 FPGA, a decrease of device usage by a factor of eight would have been necessary, which was not a realistic

perspective. Hence, a new design approach was considered: the Serial Anodes Approach, which is outlined in more detail in Section 4.7.2.

Analyzing the Device Usage

In order to decrease the device usage substantially, it was necessary to analyze the cause of the enormous device usage of the first approach. For simplicity, this analysis was performed with a single unit instead of the whole pipeline: Since the Pedestal Unit is the unit with the simplest task (to subtract two numbers), it was perfectly suited for such an analysis. It can barely be optimized algorithmically which leaves the focus on the structural overhead causing the high device usage. For this analysis, a version of the Pedestal Unit handling 32 anodes was used. Three different versions have been analyzed:

32 anode values, 32 subtractors The Pedestal Unit has parallel inputs for 32 anode values. 32 subtractors are used to perform 32 subtractions in one clock cycle.

32 anode values, 1 subtractor The Pedestal Unit has parallel inputs for 32 anode values but only one subtractor is used to perform one subtraction in 32 subsequent clock cycles. After 32 clock cycles all resulting anode values are available at the output at the same time.

1 anode values, 1 subtractor The Pedestal Unit only has one input for one anode value at a time. One subtractor is used to output the result each clock cycle for 32 subsequent clock cycles.

Table 4.12 shows the device usage for these three different versions of the Pedestal Unit. It is notable that the second version does not bring a big improvement compared to the first version. The third version shows a device usage which is very reasonable considering that the only task of the pedestal unit is to subtracting two numbers.

Table 4.12: Device Usage of different versions of the Pedestal Unit. There is a decrease in the use of Combinational Cells from the first to the second version. However, there is also a small increase in the use of Sequential Cells. Only the drastic changes of the third version bring the desired little device usage in both Combinational and Sequential Cells.

Version	Combinational Cells	Sequential Cells
32 anode values, 32 subtractors	884 of 12096 (7 %)	423 of 6048 (7 %)
32 anode values, 1 subtractor	470 of 12096 (4 %)	454 of 6048 (8 %)
1 anode values, 1 subtractor	33 of 12096 (0 %)	20 of 6048 (0 %)

4.7.2 Serial Anodes Approach

The Serial Anodes Approach (the current design, described in all detail above in this Chapter) is based on the idea that it is most efficient to only pass and process one anode with each clock cycle. As mentioned earlier, this design allows it to instantiate eight pipelines, including the interfaces to FEE and PBEE into an RTAX2000 FPGA. This is an improvement by a factor of eight towards the first version of the first approach. A further decrease by a factor of two is still necessary to reach the design goal of 16 pipelines. However, the current version of the Serial Anodes Approach is not yet optimized for device usage, leaving some room for further improvements.

Scheduled Improvements

The following improvements can reduce the device usage without a loss in functionality:

Futile Registers Futile registers need to be found an eliminated. Output registers can be used to store results also before the `is_data_flag` is set. It also needs to be analyzed whether it is more efficient to reuse certain registers for different purposes in different states of the finite state machine (FSM) or if it is more efficient to use new registers even if there are unused registers in the current state.

Common Mode The Common Mode Unit is the single most complex processing unit in the MBEE pipeline. It might be possibilities to improve the implementation of the OETS algorithm by using references to the anode list instead of copying the list in order to sort it. Another approach would be to sort the original list, determine the median and have the Detector Handling Unit send the anode values a second time to perform the actual subtraction. If the OETS algorithm cannot be improved substantially, another algorithm can be used to trade in some computing time for fewer device usage.

More RAM usage Many RAM block of the RTAX2000 FPGA are unused. It needs to be analyzed whether passing on only the triggered anode values after the Common Mode Unit and storing the other values in RAM for Engineering Mode could decrease the device usage.

More Primitives More manufacturer Primitives[9] can be used. Parts of the code, which can be replaced with Primitives, need to be found. This makes the code less portable but more efficient on the target device.

If contrary to expectations, it is not possible to reduce the device usage, with the measurements described above, to fit 16 pipelines in one RTAX2000 FPGA, it

---

[9]In general, VHDL code is device independent. FPGA manufacturers, however, provide so called Primitives, which allow to use device-specific features.

might be an option to reduce the features of the Engineering Mode. The Engineering Mode could be implemented for only one pipeline which allows the other 15 pipelines to drop unnecessary anode values after the Common Mode Unit. Another possibility would be to use a buffer before the pipelines and to use fewer pipelines than the number of Detector Handling Units. As the pipeline processing time is much faster than the expected event rate, the reduced number of pipelines would not cause a bottleneck, as it can be seen below.

4.8 Performance

With the current design the pipeline is able to process a new event every 70 clock cycles. Using a 40 MHz system clock, the pipeline can process a new event every 1.75 µs which equals to 571 428 events per second. The FEE–MBEE interface will most likely need more than 208 clock cycles (cf. Table 4.2) to read in one event. This means the pipelines would process events much faster than the expected event rate from the detectors, even if one pipeline would have to handle the events of 2 detector halves.

An average intensity of 500 mCrab would cause a count rate of about 120 000 cts/s for the whole LAD (Suchy et al., 2012), which translates into a count rate of only about 30 cts/s per detector half. Even for the instrument goal of 30 Crab peak intensity, this leads to only about 1800 cts/s per detector half. Therefore, even at peak intensity, one pipeline could handle all events of a whole module. However, each buffer that is used will complicate the dead time estimation and complex saturation effects have to be taken into account, too. Therefore, it is still desirable to have one pipeline per detector half in order to decrease the number of required buffers.

5 MBEE Hardware Prototype

This chapter describes the development of the MBEE Hardware Prototype used for VHDL design verification and general feasibility verification. Since the LOFT MBEE is the first project at IAAT that uses the Microsemi RTAX2000 FPGA as its target device, a development platform, as described in Section 5.1, had to be established prior to the development of the actual MBEE prototype, which is described in Section 5.2. Further testing is recommended to guaranty the functionality of the prototype, which is described in Section 5.3.

5.1 RTAX2000 Development Platform

This section briefly describes the Microsemi RTAX2000 FPGA, gives an overview about commercially available prototyping solutions, and presents the sustainable RTAX2000 development platform, developed in the context of this thesis.

5.1.1 Microsemi RTAX2000

The RTAX2000 (Microsemi, 2011) is a radiation tolerant FPGA[1] with antifuse technology based on Microsemi's commercial Axcelerator family. It contains 10 752 register cells (R-Cells), also called sequential cells, and 21 504 combinatorial cells (C-Cells). The output of the C-Cells only depends on the current input, whereas the output of the R-Cells is also dependent on previous inputs (storage capability). These cells can be inter-connected during configuration of the FPGA to build logical circuits, described with the hardware description language VHDL. The number of cells available in an FPGA limits the size of the logical circuit, which can be configured into the FPGA. In contrast to flash-based FPGAs, antifuse based FPGAs can be configured only once. The antifuse technology has, as the name implies, the opposite behavior of a fuse. While a fuse permanently breaks the connection when a threshold current is reached once, an antifuse permanently creates a connection, when a threshold voltage is reached once. Besides other advantages, the permanence of the connections is inherently a contribution to the radiation tolerance of the device. However, it also makes the

---

[1]A field-programmable gate array (FPGA) is an integrated circuit (IC) which can be configured for its application after manufacturing ("in field").

prototyping process more complicated and expensive.

5.1.2 Prototyping Devices

This section describes different prototyping solutions for RTAX FPGAs and explains why the Aldec Adapter has been chosen as the appropriate prototyping solution for the current design phase.

The need for prototyping solutions arises from the fact, that the flight version of the RTAX is very expensive and can be configured only once. The different RTAX prototyping solutions commercially available for different design phases are shown in Figure 5.1 and described below:

Aldec Adapter The Aldec Adapter is footprint compatible with the RTAX, but uses a flash-based ProASIC FPGA and is therefore reconfigurable. A so called netlist converter allows to use VHDL code written for an RTAX[2] to configure the ProASIC. It also performs a complete pin-mapping, so that the Aldec Adapter is pin-compatible to the RTAX footprint. This adapter can be used for design verification but is not suitable for timing verification or power consumption analysis of the design, since it utilizes a completely different FPGA, based on a different technology.

Sockets for Commercial Axcelerators Commercial Axcelerator FPGAs can be used for prototyping since the RTAX is based on the Axcelerator FPGA family. Timing and power consumption are closer to the target device. The socket maps the footprint of a commercial Axcelerator to the RTAX footprint and allows the exchange of the (one time configurable) Axcelerator without soldering the device.

Commercial Axcelerators Commercial Axcelerators are also offered in pin-compatible ceramic packages so that no socket is required. An update of the FPGA configuration is only possible by exchanging the device via soldering.

RTAX Proto Unit The RTAX Proto Unit is identical to the RTAX flight version, however space qualification tests have not been performed on these devices. It can be used for all tests including timing verification and power consumption. It is not suitable for radiation hardness tests.

RTAX Flight Version The RTAX flight version is the space qualified version of the RTAX, which means it has undergone a certified testing procedure. It is intended for use on the final flight hardware only.

Since the MBEE is in a very early design phase and easy reconfiguration is crucial, only the Aldec Adapter and the sockets for using commercial devices (a and b in Figure 5.1) come into consideration. The power supply aboard the spacecraft is limited and the waste heat of the electronics will, at least to some extent, increase

---

[2]In general, VHDL code is device independent. FPGA Manufacturers, however, provide so called Primitives, which allow to use device-specific features.

the detector temperature, which results in a degradation of the energy resolution. This makes power consumption a critical quantity in the design of the MBEE and is a sound argument for using the sockets for commercial Axcelerator FPGAs. While it is indeed possible to exchange the Axcelerator quickly in order to test a modified VHDL design, the financial effort is immense. The number of expected reconfigurations is high for two reasons: The functional verification in hardware is expected to need several iterations, and changing boundary conditions[3] will demand changes in the design. While the number of necessary hardware verification iterations can be minimized by extensive simulations, the boundary conditions will be defined in a later phase of the project. In the current design phase, the need for flexibility outweighs the advantages the use of commercial Axcelerators would bring, which is why the Aldec Adapter has been chosen.

5.1.3 Aldec Adapter Carrier Board

In this section, the Aldec Adapter Carrier Board is introduced, its advantages and disadvantages are discussed, and its key role in the IAAT RTAX development platform is explained.

While the Aldec Adapter is reconfigurable, it is still not reusable in the sense that it has to be soldered onto a printed circuit board (PCB). This means it can be reconfigured for new versions of the VHDL design, but it cannot be used for future revisions of the MBEE prototype PCB or even for other projects. It might be possible to unsolder the Aldec Adapter and to solder it onto a new board, but this is costly and time-consuming, and always involves the risk of permanently damaging the Aldec Adapter.

The Aldec Adapter Carrier Board (see Figure 5.2) has been developed to make the Aldec Adapter pluggable. The Aldec Adapter is soldered onto the top side of the PCB and there are connectors on the bottom side of the PCB, which allow the Carrier Board to be plugged onto different base boards. The Carrier Board has been developed together with an industry partner, that designed the four-layer PCB, which connects all pins from the Aldec Adapter to the connectors on the bottom side. The pin assignment on the bottom side of the Carrier Board approximately reflects the pin assignment of the Aldec Adapter and therefore the pin assignment of the RTAX. All pins from one side of the Adapter are mapped to the connector on the same side of the Carrier Board with a pin order very similar to the RTAX. The Carrier Board is also prepared for the use of differential signals. The additional flexibility of the Carrier Board comes with the price of loosing the RTAX footprint compatibility on the base board. Hence, a re-design of the MBEE prototype PCB will be necessary, when moving on to a prototyping solution closer to the RTAX. The effort necessary for the re-design, however, is small since the

---

[3]Since neither the development of the FEE-ASICs nor the development of the PBEE is completed yet, changes in the interfaces are very likely. Other boundary conditions, such as the number of detectors per module, can also be subject to change.
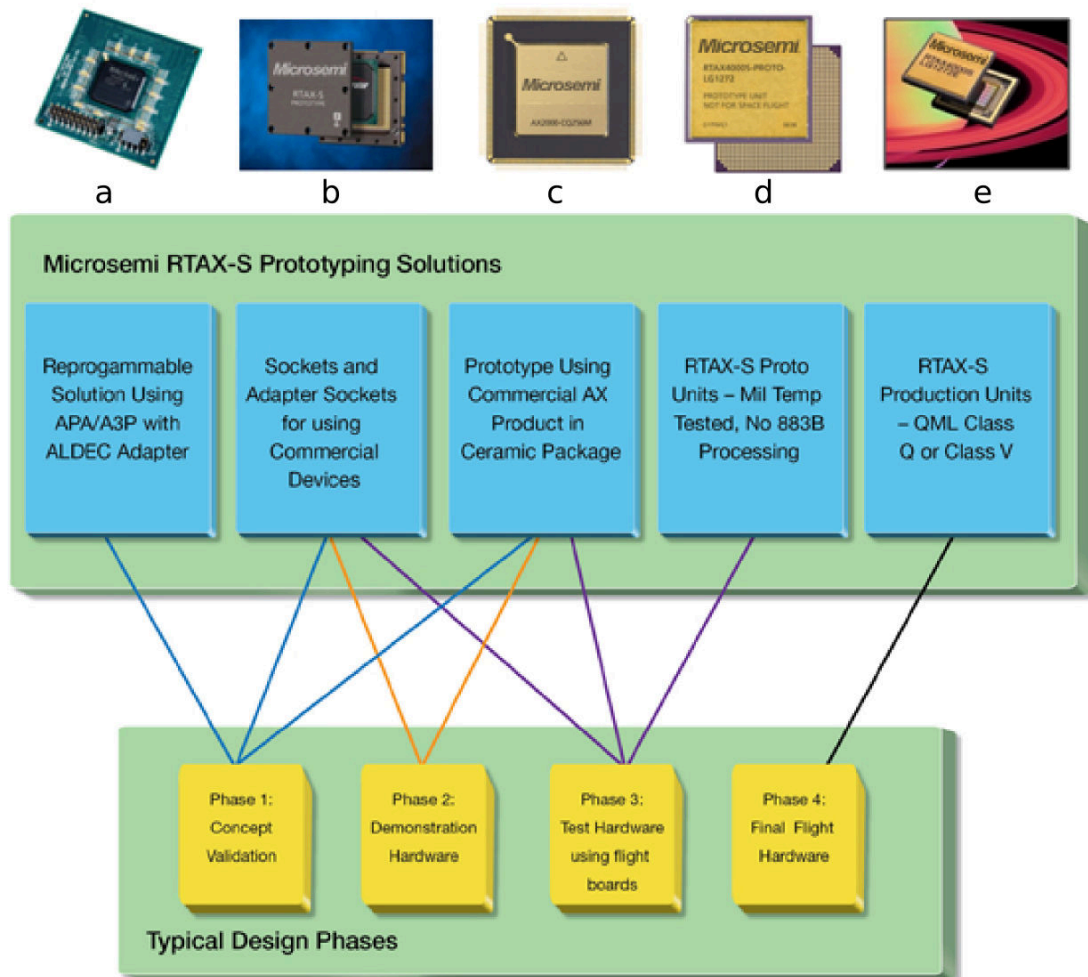
Figure 5.1: Commercial prototyping solutions for RTAX devices. From left to right the prototyping devices are intended to be used in a later design phase. (a) (b) A socket to use commercial Axcelerator versions. The Axcelerator FPGA can be configured only once, but it can be exchanged without soldering. (c) A pin-compatible commercial Axcelerator FPGA can be used in a soldering version. (d) The RTAX Proto Unit is identical to the RTAX flight version, however space qualification tests have not been performed on these devices. (e) The RTAX flight version. Source: Microsemi

pin assignment of the Carrier Board is close to the original pin assignment of the RTAX.

The Carrier Board is a sustainable solution in multiple ways. It allows to reuse Aldec Adapters for different PCB revisions and even for different projects. The PCB layout files of the Carrier Board are available at IAAT, which allows a relatively inexpensive production of further Carrier Boards, if needed. Another possibility is to assemble a Carrier Board with a socket for commercial Axcelerators, which would allow to reuse these expensive sockets, too. In this way, the first two prototyping design phases can be executed with the same Carrier Board footprint and even allow for an easy exchange of the prototyping method within the same revision of the base board, which will minimize development time and cost.

(a) top view   **(b)** bottom view
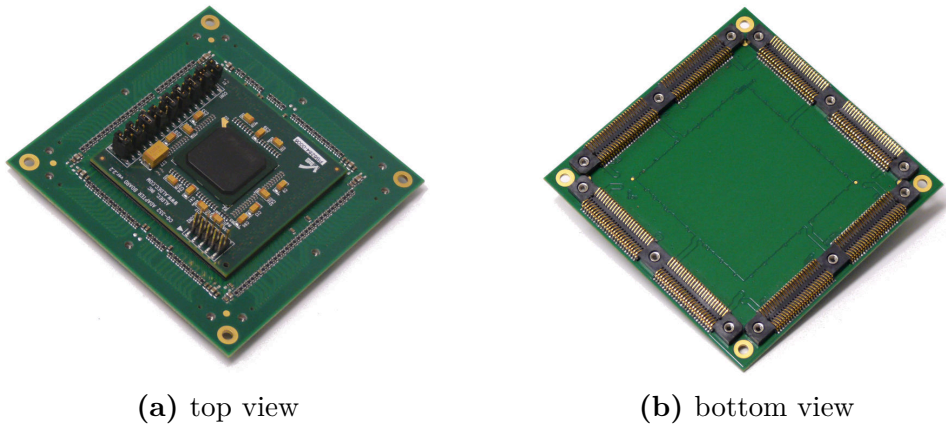
Figure 5.2: The Aldec Adapter Carrier Board. (a) Shows the Aldec Adapter soldered onto the top side of the Carrier Board. (b) Shows the connectors on the bottom side, which make the Carrier Board pluggable.

5.1.4 RTAX FPGA Development at IAAT

This section briefly describes the requirements for an RTAX FPGA development platform at IAAT and how the newly established platform meets these requirements.

In order to be able to use the platform in the long term it is important that the running costs are low. For the hardware, this is achieved by the completely reusable Aldec Adapter Carrier Board and a spare Carrier Board is ready for assembly, if necessary. Two software licenses are necessary to operate the Aldec Adapter Carrier Board. One license for the netlist converter, which allows to use VHDL code designed for an RTAX FPGA with an Aldec Adapter, and one license for the Microsemi FPGA IDE[4] Libero. For the netlist converter, there is one perpetual license present at IAAT, hence there are no further license costs to be expected. The license for the Microsemi IDE Libero needs to be renewed on a yearly basis, however, the IAAT account manager at Microsemi signaled

---

[4]Integrated Development Environment

willingness to accommodate IAAT concerning the license renewal in order to make an RTAX development platform for students possible at IAAT.

Another important requirement for the development platform is the availability of documentation. Comprehensive documentation is available for the RTAX and the Aldec Adapter. Besides the overview in this thesis, there is also technical documentation available for the Carrier Board.

5.2 MBEE Hardware Prototype

The MBEE hardware prototype is presented in this section. First, the required features are explained, then the MBBE hardware prototype PCB (hereafter referred to as the MBEE-PCB) is introduced, and it is shown how the MBEE-PCB assembly meets the requirements.

5.2.1 Requirements

This section describes the requirements for the MBEE hardware prototype concerning the mechanical dimensions, the interfaces, electronic properties, diagnosis possibilities, and space qualification.

Since the dimensions of the mechanical structure of the MBEE are not yet fixed, there is no strict requirement for the mechanical dimensions of the MBEE-PCB. Considering the size of one detector ($72.5\,\text{mm} \times 120.84\,\text{mm}$, see Figure 2.8b) the approximate size of the PCB can be estimated from Figure 2.11 to $150\,\text{mm} \times 300\,\text{mm}$. Interfaces to eight FEEs and one PBEE are necessary. Each FEE interface requires 23 signal lines (1 GND, 2×7 data lines, 2×1 CMD lines, 1 differential pair for CLK, and 2 differential pairs for trigger; cf. Sections 3.2.3 and 4.5.1). The interface to the PBEE needs to have six signal lines (1 GND, 1 differential pair for CLK, 1 differential pair for data, and 1 reset; cf. Section 3.3.1). The current baseline for the MBEE system clock frequency is $40\,\text{MHz}$, hence the MBEE-PCB must be designed accordingly. Several signals, including the clock, require LVDS, which must be considered in the PCB layout, too. Additionally, it is desirable to have as many diagnosis ports as possible on the MBEE-PCB to simplify the debugging process. Since this is a very early prototyping phase, space qualification is not necessary for the PCB or the parts used for the assembly. The last requirement is that the MBEE prototype can be operated in the FEE–MBEE–PBEE chain and also as a standalone system. For the chain configuration the clock signal can be fed into the MBEE from the PBEE. For the standalone configuration, the board needs to be able to generate its own clock signal instead. Additionally an FEE Simulator is needed.

5.2.2 PCB Assembly

The MBEE-PCB assembly and its interfaces are described in this section. Since the Aldec Adapter on the Carrier Board replaces the actual RTAX FPGA and substitutes its functions, it is here also referred to as RTAX-Adapter.

Four Detectors can be attached to the MBEE prototype board via four SUB-D 25 connectors. The prototype board also contains an on-board ASIC simulator, which can simulate the FEE–ASICs of four detectors and will be used to feed the RTAX-Adapter with simulated events. Therefore, the RTAX-Adapter has 8 FEE interfaces, four of them can be connected externally via SUB-D 25 connectors and the other four are connected to the ASIC simulator via the MBEE-PCB. The ASIC simulator is described in Section 4.6.1 and is implemented in a Xilinx Spartan 3 FPGA. A USB port is connected to the Spartan 3 FPGA, which allows to feed external event data into the simulator[5]. The clock signal is distributed by an LVDS clock buffer to the RTAX-Adapter, the Spartan 3 FPGA, and the four external FEE interfaces simultaneously. The clock buffer has two selectable inputs, one is connected to a 40 MHz oscillator on the MBEE-PCB, and the other one to the SUB-D 9 connector, which is used to interface the PBEE. A jumper determines whether the internal or an external clock signal is used.

MBEE-PCB Layout

The MBEE-PCB layout has been designed in the context of this thesis. Figure 5.3 shows the PCB layout and Table 5.1 describes the six PCB layers. The top and bottom layers are used to connect single ended signals, whereas the differential signals are routed in the inner two layers, which are shielded by a ground layer beneath and above. Using two layers for differential signals allows to route the two signal lines of one pair on top of each other, which is reducing the electromagnetic susceptibility and ensuring that both lines have the same length.

Table 5.1: Layers of the MBEE Prototype PCB.

Layer	Name	Description
1	TOP	Mainly used for power supply, to connect the RTAX-Adapter with the FEE interface connectors and the ASIC simulator
2	GND	GND layer to shield the LVDS connections.
3	LVDS_P	Mainly used for all LVDS connections.
4	LVDS_N	Mainly used for all LVDS connections.
5	GND	GND layer to shield the LVDS connections.
6	BOT	Mainly used to connect the RTAX-Adapter with the ASIC simulator.

---

[5]While the hardware is prepared for the use of the USB port, it is not implemented yet.
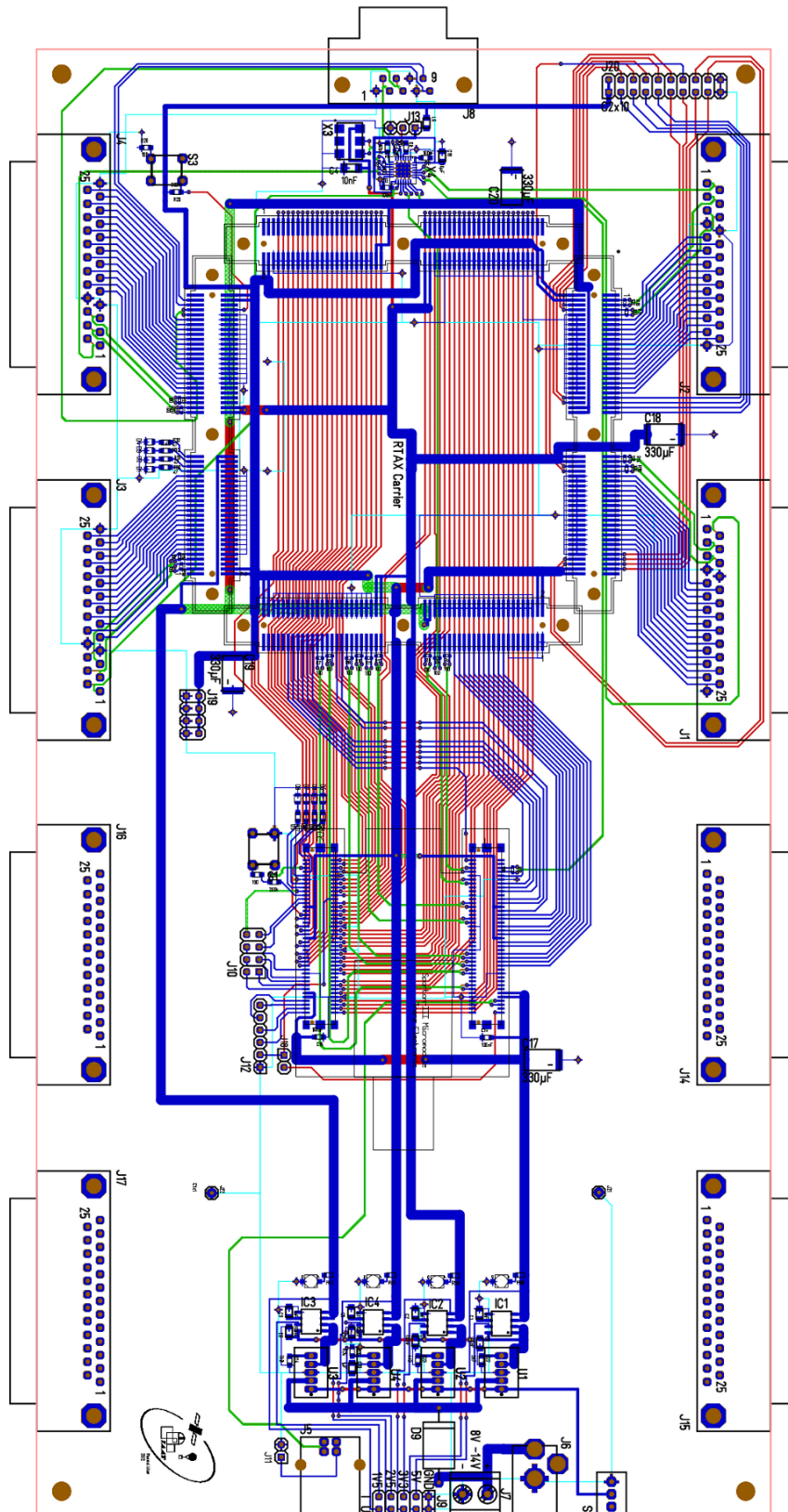
Figure 5.3: MBEE Prototype PCB Layout. The MBEE-PCB has 6 layers: 1 (TOP) blue, 2 (GND) hidden, 3 (LVDS_P) green, 4 (LVDS_N) brown, 5 (GND) hidden, 6 (BOT) red. All GND areas hidden. Size: $150\,\mathrm{mm} \times 300\,\mathrm{mm}$
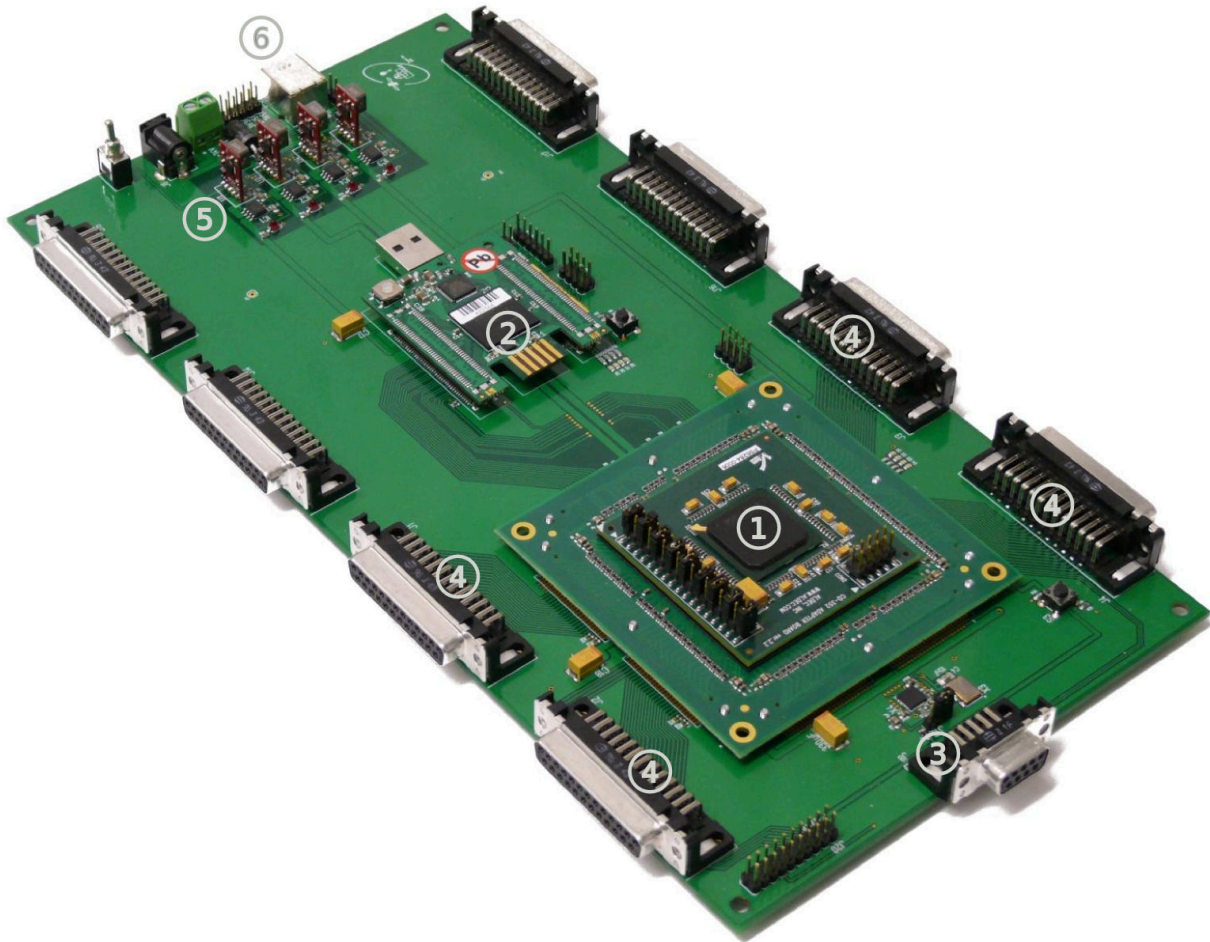
Figure 5.4: MBEE Prototype PCB Assembly. (1) Aldec Adapter, (2) Spartan 3, (3) PBEE-Interface, (4) FEE-Interface, (5) Power Supply, (6) USB Port

5.3 Testing the MBEE Prototype

Testing the MBEE prototype is essential to ensure its functionality under a wide range of conditions. This section describes how the MBEE Prototype has been tested and what further testing is recommended.

Each pipeline unit of the MBEE has been verified separately in simulation with a set of random anode values. The complete pipeline has been tested successfully in simulation with a set of realistic anode values, and the MBEE VHDL code has been tested with 16 pipelines processing event data simultaneously at various event rates. All tests have been passed successfully. Before powering up the MBEE prototype for the first time, the MBEE-PCB has been visually and electrically inspected. All voltages were found to be within the tolerances and the clock buffer worked as expected. The functionality of the Aldec Adapter and the Spartan 3 FPGA has been verified separately.

Further tests are required to ensure the full functionality of the MBEE prototype. Single units of the VHDL design need to be tested in hardware, which can be accomplished through bypassing the other pipeline units in the engineering mode. A complete pipeline with all units active has to be tested as well. The functionality of the MBEE must be verified when all pipelines are operating simultaneously. All tests need to be repeated with a variety of simulated events, such as realistic event data to ensure the functionality under the expected circumstances, and random event data in order to find problems that only occur in situations, which were not expected. Besides operating the prototype with event rates as they are predicted, tests need to be performed with event rates unusually low and as high as the interface transfer rate allows. The event processing has to be verified in the engineering mode as well as in science mode. The configuration mode needs to be verified as well. Not only the functionality of the MBEE prototype itself must be ensured, but also the functionality and stability of the interfaces. While the functionality of the interface is, at least to a certain degree, implicitly tested, when testing the MBEE, some features of the interfaces need more explicit testing. Since only very few communication errors are to be expected under laboratory conditions, errors must be artificially introduced to test the error handling capabilities of the interfaces. Those tests are strongly recommended in order to ensure further improvements in functionality and stability of the MBEE prototype.

6 Summary, Results and Outlook

The results of this thesis are summarized in this chapter and a brief outlook on the future development of the MBEE and LOFT is given.

Results of this Thesis

The three main results of this thesis are 1) a working VHDL design for the LOFT Module Back End Electronics (MBEE), 2) the establishment of an RTAX FPGA development platform at IAAT, and 3) a functional hardware prototype of the LOFT MBEE including a PCB layout.

The VHDL design of the MBEE includes a pipeline design for fast event reconstruction, an interface to read out and control the ASICs of the Front End Electronics (FEE–ASICs), the structure required for the simultaneous operation of multiple pipelines, and an interface to the Panel Back End Electronics (PBEE) to pass on the processed event data. Two different design approaches for the data processing pipeline, one with a parallel processing of the anode values and one with a serial processing, have been implemented, each with its own simulation environment. Both design approaches have been evaluated and compared. The Serial Anodes Approach was chosen, as it has been found to be more efficient. The data processing units of the pipeline have been tested individually with automated testbenches, created especially for this purpose. Since there has been no protocol defined for the MBEE–FEE interfaces within the collaboration yet, a protocol has been devised and implemented solely for the use within this thesis. This implementation can, however, also serve as a starting point for the final protocol. It allows to feed event data into the pipeline for testing and can be used to estimate the FPGA resource usage required by the interface. The structure which allows to operate multiple pipelines simultaneously has been designed in a way that allows to adjust the number of pipelines easily and its functionality has been verified. The event data from all pipelines are transmitted via the MBEE–PBEE interface, which has been implemented in the MBEE and modified for the use with an RTAX FPGA in the context of this thesis[1]. The complete behavior of the MBEE can be reproduced in an end–to–end simulation, which is especially important during the current assessment phase of LOFT in order to determine parameters such as event processing times and transfer rates to evaluate the capabilities of the system.

---

[1]The interface to the PBEE has been implemented and modified but was not originally developed in the context of this thesis.

While it is possible with the current MBEE VHDL design to implement eight pipelines in an RTAX2000, it has been shown that an increase of this number to the design goal of 16 is likely to be achieved with further optimizations. For the unlikely case that it will not be possible to implement all 16 pipelines, the current eight pipelines are sufficiently fast to reach the design goal of 30 Crab peak intensity. In fact, the pipelines are so fast that even a single pipeline could handle the events of an entire module, generated by a 30 Crab observation[2].

The second main result of this thesis is the establishment of an RTAX FPGA development platform at IAAT. Since the RTAX FPGA can be configured only once and is, as a space qualified FPGA, rather expensive, a variety of prototyping solutions are commercially available. These solutions have been reviewed and the most appropriate one has been chosen, the Aldec Adapter. While the Aldec Adapter is reconfigurable, it still needs to be soldered onto a PCB, which does not allow to use this expensive device in future prototype revisions or even other projects. Therefore, a carrier board has been developed together with an industry partner, which makes the Aldec Adapter pluggable and allows to reuse it. The Aldec Adapter Carrier Board is a sound foundation for a sustainable RTAX development platform at IAAT. Also licensing options have been reviewed and a solution was found, which allows to use the RTAX development platform in the long term.

The third important result of this thesis is the MBEE hardware prototype. It is prepared to handle, in accordance with the design goal, eight detectors. Four FEE interfaces can be connected externally, and the other half is internally connected to the ASIC simulator. The ASIC simulator, developed especially for this purpose, is another FPGA, which simulates the behavior of the ASICs towards the MBEE and can be used to feed the MBEE with event data. The PCB of the prototype, also designed in the context of this thesis, has six layers and differential signals are routed on top of each other in two shielded layers. The prototype is operational and ready for further testing. It allows to verify the MBEE VHDL code in hardware, which is mandatory to ensure the full functionality of the MBEE. The MBEE–FEE and MBEE-PBEE interfaces can now be tested in hardware, which is especially important since behavioral simulations do not include delays introduced by signals routed over wires with a finite length. The future development of other devices, such as the FEE and particularly the FEE–ASICs, the PBEE, or even the detectors, will strongly benefit from the existence of an MBEE hardware prototype.

Finally, the feasibility of the MBEE being based on an RTAX2000 FPGA has been conclusively demonstrated and key quantities, such as physical dimensions, weight, and power consumption can be compared to previous estimates.

---

[2]While this would indeed be possible, it is not desirable for reasons explained in Section 4.8

Outlook

Further testing is required to ensure the functionality of the MBEE under a wide range of conditions. It is necessary to test the MBEE in science and in engineering mode with a wide range of event data, from realistic data, as they are expected from simulations, to completely random data in order to ensure functionality in unexpected situations. The VHDL code of the MBEE will be further optimized and the integration of the current MBEE prototype with the PBEE is a priority at IAAT. Later revisions of the MBEE with prototyping devices closer to the RTAX flight version will be built in Phase B, after the mission selection by ESA, and will allow to optimize the MBBE towards power consumption, dimensions and weight. The MBEE will be integrated with the other LOFT electronics and finally complete modules will be tested with X-ray radiation in calibration facilities. The final production of the MBEE will be coordinated with industry partners by IAAT, too. The currently on-going assessment phase of LOFT will be completed by the end of 2013 after the delivery of the Yellow Book[3] to ESA in October. By the first quarter of 2014, ESA is expected to select one of the five mission candidates. If selected, LOFT will be launched between 2022 and 2024 and will be able to contribute to X-ray astronomy and beyond in a truly magnificent way.

---

[3]The so called Yellow Book is the assessment study report including the scientific objectives as well as a detailed payload description.

Acknowledgments

I would like to thank all members of the institute which contributed to making this last year a highlight of my studies. I really enjoyed the time with you guys, thank you so much! There are a few people who I owe special thanks to:

Dr. Chris Tenzer for his excellent mentoring throughout the last year. He rather works night shifts than not having time for his students. He encouraged me to pursue my interests in electronics and always offered his help, when needed. Thank you so much!

Prof. Dr. Santangelo for the assignment of this thesis, the friendly welcome to the group and of course for a great week in Castellomare del Golfo.

Thomas Schanz for his help with VHDL, FPGAs and electronics in general, for proofreading this thesis and for getting me to buy a bike again. 73!

Dr. Slawomir Suchy for supplying me with simulation data, for proofreading this thesis and his interest in my work.

Jörg Bayer for sharing his enormous knowledge about FPGAs and electronics, and especially for his help concerning the design of the PCB.

Henning Wende and Daniel Maier for their support with everyday problems, but most of all for a great year in the shared office. I enjoyed our vivid discussion about physics, astronomy and society very much!

Thank you!

Bibliography

Ables, J. G. (1968). "Fourier transform photography: a new method for X-ray astronomy". In: *Proceedings of the Astronomical Society of Australia* 1, p. 172.

Abramowicz, M. A. and W. Kluźniak (2001). "A precise determination of black hole spin in GRO J1655-40". In: *Astronomy and Astrophysics* 374, pp. L19–L20. DOI: 10.1051/0004-6361:20010791. eprint: arXiv:astro-ph/0105077.

Akmal, A., V. R. Pandharipande, and D. G. Ravenhall (1998). "Equation of state of nucleon matter and neutron star structure". In: *Physical Review C* 58, pp. 1804–1828. DOI: 10.1103/PhysRevC.58.1804. eprint: arXiv:hep-ph/9804388.

Asai, K. et al. (2000). "Iron K Emission Lines in the Energy Spectra of Low-Mass X-Ray Binaries Observed with ASCA". In: *Astrophysical Journal, Supplement* 131, pp. 571–591. DOI: 10.1086/317374.

Bambynek, W. et al. (1972). "X-Ray Fluorescence Yields, Auger, and Coster-Kronig Transition Probabilities". In: *Reviews of Modern Physics* 44, pp. 716–813. DOI: 10.1103/RevModPhys.44.716.

Basko, M. M. and R. A. Sunyaev (1975). "Radiative transfer in a strong magnetic field and accreting X-ray pulsars". In: *Astronomy and Astrophysics* 42, pp. 311–321.

Belloni, T. M. and E. Bozzo (2012). "LOFT: the Large Observatory For X-ray Timing". In: *ArXiv e-prints*. arXiv:1211.1905 [astro-ph.IM].

Berger, M.J. et al. (2011). *XCOM: Photon Cross Sections Database*. URL: http://www.nist.gov/pml/data/xcom/index.cfm.

Bhattacharyya, S. et al. (2005). "Constraints on Neutron Star Parameters from Burst Oscillation Light Curves of the Accreting Millisecond Pulsar XTE J1814-338". In: *Astrophysical Journal* 619, pp. 483–491. DOI: 10.1086/426383. eprint: arXiv:astro-ph/0402534.

Bibliography

Blumenthal, G. R. and R. J. Gould (1970). "Bremsstrahlung, Synchrotron Radiation, and Compton Scattering of High-Energy Electrons Traversing Dilute Gases". In: *Reviews of Modern Physics* 42, pp. 237–271. DOI: 10.1103/RevModPhys.42.237.

Boella, G. et al. (1997). "BeppoSAX, the wide band mission for X-ray astronomy". In: *Astronomy and Astrophysics, Supplement* 122, pp. 299–307. DOI: 10.1051/aas:1997136.

Bradt, H. V., R. E. Rothschild, and J. H. Swank (1993). "X-ray timing explorer mission". In: *Astronomy and Astrophysics, Supplement* 97, pp. 355–360.

Brandt, S. et al. (2012). "The LOFT wide field monitor". In: *Society of Photo-Optical Instrumentation Engineers (SPIE) Conference Series*. Vol. 8443. Society of Photo-Optical Instrumentation Engineers (SPIE) Conference Series. DOI: 10.1117/12.926060. arXiv:1209.1499 [astro-ph.IM].

Carroll, B.W. and D.A. Ostlie (2007). *An introduction to modern astrophysics*. Pearson Addison-Wesley. ISBN: 9780805304022.

Christmann, S. D. (2011). "Design and implementation of an FPGA-driven, hardware-based realtime data reduction system for pixelated photon detectors". Diplomarbeit. IAAT, Eberhard Karls Universität Tübingen.

Dicke, R. H. (1968). "Scatter-Hole Cameras for X-Rays and Gamma Rays". In: *Astrophysical Journal, Letters* 153, p. L101. DOI: 10.1086/180230.

Fabian, A. C. et al. (1989). "X-ray fluorescence from the inner disc in Cygnus X-1". In: *Monthly Notices of the RAS* 238, pp. 729–736.

Fabian, A. C. et al. (2000). "Broad Iron Lines in Active Galactic Nuclei". In: *The Publications of the Astronomical Society of the Pacific* 112, pp. 1145–1161. DOI: 10.1086/316610. eprint: arXiv:astro-ph/0004366.

Feroci, M. et al. (2012). "LOFT: the Large Observatory For X-ray Timing". In: *Society of Photo-Optical Instrumentation Engineers (SPIE) Conference Series*. Vol. 8443. Society of Photo-Optical Instrumentation Engineers (SPIE) Conference Series. DOI: 10.1117/12.926310. arXiv:1209.1497 [astro-ph.IM].

Frontera, F. et al. (2001). "Broadband Spectrum of Cygnus X-1 in Two Spectral States with BeppoSAX". In: *Astrophysical Journal* 546, pp. 1027–1037. DOI: 10.1086/318304. eprint: arXiv:astro-ph/0009160.

Gamow, G. and M. Schoenberg (1941). "Neutrino Theory of Stellar Collapse". In: *Physical Review* 59, pp. 539–547. DOI: 10.1103/PhysRev.59.539.

Gatti, E. and P. Rehak (1984). "Semiconductor drift chamber – An application of a novel charge transport scheme". In: *Nuclear Instruments and Methods in Physics Research* 225, pp. 608–614. DOI: 10.1016/0167-5087(84)90113-3.

Giacconi, R. et al. (1971). "An X-Ray Scan of the Galactic Plane from UHURU". In: *Astrophysical Journal, Letters* 165, p. L27. DOI: 10.1086/180711.

Glasser, C. A., C. E. Odell, and S. E. Seufert (1994). "The proportional counter array (PCA) instrument for the X-ray timing explorer satellite (XTE)". In: *IEEE Transactions on Nuclear Science* 41, pp. 1343–1348. DOI: 10.1109/23.322911.

Gnedin, O. Y., D. G. Yakovlev, and A. Y. Potekhin (2001). "Thermal relaxation in young neutron stars". In: *Monthly Notices of the RAS* 324, pp. 725–736. DOI: 10.1046/j.1365-8711.2001.04359.x. eprint: arXiv:astro-ph/0012306.

Gruber, D. E. et al. (1996). "The high energy X-ray timing experiment on XTE." In: *Astronomy and Astrophysics, Supplement* 120, p. C641.

Harrison, F. A. et al. (2010). "The Nuclear Spectroscopic Telescope Array (NuSTAR)". In: *Society of Photo-Optical Instrumentation Engineers (SPIE) Conference Series.* Vol. 7732. Society of Photo-Optical Instrumentation Engineers (SPIE) Conference Series. DOI: 10.1117/12.858065. arXiv:1008.1362 [astro-ph.IM].

Illarionov, A. F. and R. A. Siuniaev (1975). "Comptonization, characteristic radiation spectra, and thermal balance of low-density plasma". In: *Soviet Astronomy* 18, pp. 413–419.

Jahoda, K. et al. (2006). "Calibration of the Rossi X-Ray Timing Explorer Proportional Counter Array". In: *Astrophysical Journal, Supplement* 163, pp. 401–423. DOI: 10.1086/500659. eprint: arXiv:astro-ph/0511531.

Jansen, F. et al. (2001). "XMM-Newton observatory. I. The spacecraft and operations". In: *Astronomy and Astrophysics* 365, pp. L1–L6. DOI: 10.1051/0004-6361:20000036.

Bibliography

Karttunen, H. et al. (2007). *Fundamental Astronomy*. Springer. ISBN: 9783540341437.

Kelley, R. L. et al. (2007). "The Suzaku High Resolution X-Ray Spectrometer". In: *Publications of the ASJ* 59, pp. 77–112.

Koyama, K. et al. (2007). "X-Ray Imaging Spectrometer (XIS) on Board Suzaku". In: *Publications of the ASJ* 59, pp. 23–33.

LOFT Consortium (2012a). *LOFT Mission Requirements Document*. Version 3.4. European Space Agency.

— (2012b). *LOFT Payload Definition Document*. Version 2.3. European Space Agency.

— (2012c). *LOFT Proposal Draft*. Version 2.6. European Space Agency.

— (2012d). *LOFT Science Requirements Document*. Version 1.6. European Space Agency.

— (2013). URL: http://www.isdc.unige.ch/loft/.

Lechner, P. et al. (1996). "Silicon drift detectors for high resolution room temperature X-ray spectroscopy". In: *Nuclear Instruments and Methods in Physics Research A* 377, pp. 346–351. DOI: 10.1016/0168-9002(96)00210-0.

Lechner, P. et al. (2001). "Silicon drift detectors for high count rate X-ray spectroscopy at room temperature". In: *Nuclear Instruments and Methods in Physics Research A* 458, pp. 281–287. DOI: 10.1016/S0168-9002(00)00872-X.

Leighton, Frank Thomson (1991). *Introduction to Parallel Algorithms and Architectures: Arrays, Trees, Hypercubes*. 1st ed. Morgan Kaufmann Pub. ISBN: 9781558601178.

Levine, A. M. et al. (1996). "First Results from the All-Sky Monitor on the Rossi X-Ray Timing Explorer". In: *Astrophysical Journal, Letters* 469, p. L33. DOI: 10.1086/310260. eprint: arXiv:astro-ph/9608109.

Liu, Q. Z., J. van Paradijs, and E. P. J. van den Heuvel (2001). "A catalogue of low-mass X-ray binaries". In: *Astronomy and Astrophysics* 368, pp. 1021–1054. DOI: 10.1051/0004-6361:20010075.

Longair, Malcolm S., ed. (2004). *Particles, photons and their detection*. 2. ed., repr. with corr. Cambridge: Cambridge Univ. Press, XVII, 418 S. ISBN: 0-521-38773-6.

Manzo, G. et al. (1997). "The high pressure gas scintillation proportional counter on-board the BeppoSAX X-ray astronomy satellite". In: *Astronomy and Astrophysics, Supplement* 122, pp. 341–356. DOI: 10.1051/aas:1997139.

Markoff, S. et al. (2003). "Exploring the role of jets in the radio/X-ray correlations of GX 339-4". In: *Astronomy and Astrophysics* 397, pp. 645–658. DOI: 10.1051/0004-6361:20021497. eprint: arXiv:astro-ph/0210439.

Matt, G. et al. (1997). "Hard X-ray detection of NGC 1068 with BeppoSAX." In: *Astronomy and Astrophysics* 325, pp. L13–L16. eprint: arXiv:astro-ph/9707065.

Matteson, J. L. et al. (1985). "Advanced techniques for high resolution spectroscopic observations of cosmic gamma-ray sources". In: *International Cosmic Ray Conference.* Ed. by F. C. Jones. Vol. 3. International Cosmic Ray Conference, pp. 326–329.

Meszaros, P. (1984). "Radiation from accreting magnetized neutron stars". In: *Space Science Reviews* 38, pp. 325–351. DOI: 10.1007/BF00176833.

Microsemi (2011). *RTAX-S/SL and RTAX-DSP Radiation-Tolerant FPGAs.* Data sheet. Version 14.

Miniutti, G., A. C. Fabian, and J. M. Miller (2004). "The relativistic Fe emission line in XTE J1650-500 with BeppoSAX: evidence for black hole spin and light-bending effects?" In: *Monthly Notices of the RAS* 351, pp. 466–472. DOI: 10.1111/j.1365-2966.2004.07794.x. eprint: arXiv:astro-ph/0311037.

Mirabel, I. F. (2007). "Black holes: from stars to galaxies". In: *IAU Symposium.* Ed. by V. Karas and G. Matt. Vol. 238. IAU Symposium, pp. 309–314. DOI: 10.1017/S1743921307005224. eprint: arXiv:astro-ph/0612188.

Mitsuda, K. et al. (2007). "The X-Ray Observatory Suzaku". In: *Publications of the ASJ* 59, pp. 1–7.

Morrison, D., S.C. Wolff, and A. Fraknoi (1995). *Abell's Exploration of the Universe.* Saunders Golden Sunburst Series. Saunders College Pub. ISBN: 9780030010347.

Nandra, K. et al. (2007). "An XMM-Newton survey of broad iron lines in Seyfert galaxies". In: *Monthly Notices of the RAS* 382, pp. 194–228. DOI: 10.1111/j.1365-2966.2007.12331.x. arXiv:0708.1305.

Bibliography

Neddermeyer, H. (1979). "H. K. U. Lotsch (Ed.): Topics in Applied Physics. Vol. 26: L. Ley, M. Cardona (Eds.): Photoemission in Solids I. General Principles. Springer-Verlag, Berlin, Heidelberg, New York 1978." In: *Berichte der Bunsengesellschaft für physikalische Chemie* 83.9, pp. 962–963. ISSN: 0005-9021. DOI: 10.1002/bbpc.19790830919.

Orosz, Jerome A. et al. (2002). "Dynamical Evidence for a Black Hole in the Microquasar XTE J1550-564". In: *The Astrophysical Journal* 568.2, p. 845. URL: http://stacks.iop.org/0004-637X/568/i=2/a=845.

Policarpo, A. J. P. L. et al. (1972). "Improved resolution for low energies with gas proportional scintillation chambers". In: *Nuclear Instruments and Methods* 102, p. 337. DOI: 10.1016/0029-554X(72)90733-1.

Poutanen, J. and M. Gierliński (2003). "On the nature of the X-ray emission from the accreting millisecond pulsar SAX J1808.4-3658". In: *Monthly Notices of the RAS* 343, pp. 1301–1311. DOI: 10.1046/j.1365-8711.2003.06773.x. eprint: arXiv:astro-ph/0303084.

Rashevsky, A. et al. (2002). "Large area silicon drift detector for the ALICE experiment". In: *Nuclear Instruments and Methods in Physics Research A* 485, pp. 54–60. DOI: 10.1016/S0168-9002(02)00531-4.

Rehak, P. et al. (1985). "Semiconductor drift chambers for position and energy measurements". In: *Nuclear Instruments and Methods in Physics Research A* 235, pp. 224–234. DOI: 10.1016/0168-9002(85)90557-1.

Remillard, R. A. and J. E. McClintock (2006). "X-Ray Properties of Black-Hole Binaries". In: *Annual Review of Astron and Astrophys* 44, pp. 49–92. DOI: 10.1146/annurev.astro.44.051905.092532. eprint: arXiv:astro-ph/0606352.

Sauli, Fabio (1977). "Principles of operation of multiwire proportional and drift chambers". In: CERN, Geneva, 1975 - 1976. CERN. Geneva: CERN, 92 p.

Seward, F. D. and Z.-R. Wang (1988). "Pulsars, X-ray synchrotron nebulae, and guest stars". In: *Astrophysical Journal* 332, pp. 199–205. DOI: 10.1086/166646.

Seward, Frederick (2010). *Exploring the X-ray universe.* Cambridge, UK New York: Cambridge University Press. ISBN: 9780521884839.

Shakura, N. I. and R. A. Sunyaev (1973). "Black holes in binary systems. Observational appearance." In: *Astronomy and Astrophysics* 24, pp. 337–355.

Shapiro, S.L. and S.A. Teukolsky (2008). *Black Holes, White Dwarfs and Neutron Stars*. Wiley. ISBN: 9783527617678. URL: http://books.google.de/books?id=d1CRQIcP1zoC.

Skinner, G. K. (1995). "Coding (and Decoding) Coded Mask Telescopes". In: *Experimental Astronomy* 6, pp. 1–7. DOI: 10.1007/BF00419252.

Smithonian Astrophysical Observatory, Chandra X-ray Observatory (2011). *Details of Chandra Specifications*. URL: http://chandra.harvard.edu/graphics/resources/handouts/lithos/chandra_specs_litho.pdf (visited on 01/03/2013).

Spieler, H. (2005). *Semiconductor Detector Systems*. Series on Semiconductor Science and Technology. OUP Oxford. ISBN: 9780198527848.

Stella, L., M. Vietri, and S. M. Morsink (1999). "Correlations in the Quasi-periodic Oscillation Frequencies of Low-Mass X-Ray Binaries and the Relativistic Precession Model". In: *Astrophysical Journal, Letters* 524, pp. L63–L66. DOI: 10.1086/312291. eprint: arXiv:astro-ph/9907346.

Strohmayer, T. E. (2004). "Future Probes of the Neutron Star Equation of State Using X-ray Bursts". In: *X-ray Timing 2003: Rossi and Beyond*. Ed. by P. Kaaret, F. K. Lamb, and J. H. Swank. Vol. 714. American Institute of Physics Conference Series, pp. 245–252. DOI: 10.1063/1.1781035. eprint: arXiv:astro-ph/0401465.

Strohmayer, T. E. et al. (1996). "Millisecond X-Ray Variability from an Accreting Neutron Star System". In: *Astrophysical Journal, Letters* 469, p. L9. DOI: 10.1086/310261.

Strohmayer, T. and L. Bildsten (2003). "New Views of Thermonuclear Bursts". In: *ArXiv Astrophysics e-prints*. eprint: arXiv:astro-ph/0301544.

Strüder, L. et al. (2001). "The European Photon Imaging Camera on XMM-Newton: The pn-CCD camera". In: *Astronomy and Astrophysics* 365, pp. L18–L26. DOI: 10.1051/0004-6361:20000066.

Suchy, S. et al. (2012). "The on-board data handling concept for the LOFT large area detector". In: *Society of Photo-Optical Instrumentation Engineers (SPIE) Conference Series*. Vol. 8443. Society of Photo-Optical Instrumentation Engi-

neers (SPIE) Conference Series. DOI: `10.1117/12.925663`. arXiv:`1209.1844` `[astro-ph.IM]`.

Suzuki, K. et al. (1984). "Detection of iron K-emission lines from two low-mass binary X-ray sources - Scorpius X-1 and 4U 1608-52". In: *Publications of the ASJ* 36, pp. 761–767.

Swank, J. H. (2006). "The Rossi X-ray timing explorer: Capabilities, achievements and aims". In: *Advances in Space Research* 38, pp. 2959–2963. DOI: `10.1016/j.asr.2006.07.009`.

Takahashi, T. et al. (2007). "Hard X-Ray Detector (HXD) on Board Suzaku". In: *Publications of the ASJ* 59, pp. 35–51. eprint: `arXiv:astro-ph/0611232`.

Terada, Y. et al. (2008). "In-Orbit Timing Calibration of the Hard X-Ray Detector on Board Suzaku". In: *Publications of the ASJ* 60, p. 25. arXiv:`0711.2715`.

Thorsett, S. E. and D. Chakrabarty (1999). "Neutron Star Mass Measurements. I. Radio Pulsars". In: *Astrophysical Journal* 512, pp. 288–299. DOI: `10.1086/306742`. eprint: `arXiv:astro-ph/9803260`.

Titarchuk, L. (1994). "Generalized Comptonization models and application to the recent high-energy observations". In: *Astrophysical Journal* 434, pp. 570–586. DOI: `10.1086/174760`.

Toor, A. and F. D. Seward (1974). "The Crab Nebula as a calibration source for X-ray astronomy". In: *Astronomical Journal* 79, pp. 995–999. DOI: `10.1086/111643`.

Trümper, J.E. and G. Hasinger (2007). *The Universe in X-Rays*. Astronomy and Astrophysics Library. Springer London, Limited. ISBN: 9783540344124.

Turner, M. J. L. et al. (2001). "The European Photon Imaging Camera on XMM-Newton: The MOS cameras : The MOS cameras". In: *Astronomy and Astrophysics* 365, pp. L27–L35. DOI: `10.1051/0004-6361:20000087`. eprint: `arXiv:astro-ph/0011498`.

Vacchi, A. et al. (1991). "Performance of the UA6 large-area silicon drift chamber prototype". In: *Nuclear Instruments and Methods in Physics Research A* 306, pp. 187–193. DOI: `10.1016/0168-9002(91)90318-K`.

Weisskopf, M. C. et al. (2002). "An Overview of the Performance and Scientific Results from the Chandra X-Ray Observatory". In: *Publications of the ASP* 114, pp. 1–24. DOI: 10.1086/338108. eprint: arXiv:astro-ph/0110308.

Winter, M. (2013). *WebElements*. URL: http://www.webelements.com/silicon/orbital_properties.html (visited on 01/03/2013).

Wolter, H. (1952). "Spiegelsysteme streifenden Einfalls als abbildende Optiken für Röntgenstrahlen". In: *Annalen der Physik* 445, pp. 94–114. DOI: 10.1002/andp.19524450108.

Zampa, G., A. Rashevsky, and A. Vacchi (2009). "The X-Ray Spectroscopic Performance of a Very Large Area Silicon Drift Detector". In: *IEEE Transactions on Nuclear Science* 56, pp. 832–835. DOI: 10.1109/TNS.2008.2007955.

Zane, S. et al. (2012). "A large area detector proposed for the Large Observatory for X-ray Timing (LOFT)". In: *Society of Photo-Optical Instrumentation Engineers (SPIE) Conference Series*. Vol. 8443. Society of Photo-Optical Instrumentation Engineers (SPIE) Conference Series. DOI: 10.1117/12.925156. arXiv:1209.1498 [astro-ph.IM].

in't Zand, J. J. M. and N. N. Weinberg (2010). "Evidence of heavy-element ashes in thermonuclear X-ray bursts with photospheric superexpansion". In: *Astronomy and Astrophysics* 520, A81, A81. DOI: 10.1051/0004-6361/200913952. arXiv:1001.0900 [astro-ph.HE].

van der Klis, M. (2000). "Millisecond Oscillations in X-ray Binaries". In: *Annual Review of Astron and Astrophys* 38, pp. 717–760. DOI: 10.1146/annurev.astro.38.1.717. eprint: arXiv:astro-ph/0001167.

van der Klis, M. et al. (1985). "Intensity-dependent quasi-periodic oscillations in the X-ray flux of GX5 - 1". In: *Nature* 316, pp. 225–230. DOI: 10.1038/316225a0.

van der Klis, M. et al. (1996). "Discovery of Submillisecond Quasi-periodic Oscillations in the X-Ray Flux of Scorpius X-1". In: *Astrophysical Journal, Letters* 469, p. L1. DOI: 10.1086/310251. eprint: arXiv:astro-ph/9607047.

List of Figures

List of Figures

List of Tables

Erklärung

Hiermit erkläre ich, Pascal Uter, geboren am 07.11.1986 in Filderstadt, dass ich meine Diplomarbeit mit dem Titel **"Development of the Module Back End Electronics for the Large Observatory For X-ray Timing"** selbständig verfasst und nur die in diesem Dokument angegebenen Quellen und Hilfsmittel verwendet habe.

Pascal Uter